



Norwegian University of  
Science and Technology

# Perforation of Steel Plates at Various Temperatures

**Daniel Gulbrandsen**

Master of Science in Mechanical Engineering

Submission date: June 2017

Supervisor: Tore Børvik, KT

Norwegian University of Science and Technology  
Department of Structural Engineering








## MASTER'S THESIS 2017

SUBJECT AREA: Computational Mechanics	DATE: 11 June 2017	NO. OF PAGES: 129 20+98+11
--	-----------------------	-------------------------------

TITLE: <b>Perforation of Steel Plates at Various Temperatures</b>	
BY:  Daniel Gulbrandsen	

SUMMARY: <p>The primary objective of this thesis was to investigate how the temperature affects the perforation resistance of the high-strength steel ArmoX 500T and the low-strength steel NVE 36. This was investigated both experimentally and numerically.</p> <p>Tensile tests were conducted at room temperature to obtain the material properties for both materials. The ArmoX 500T was shown to have a yield stress of about four times the yield stress of the NVE 36 steel, while for the ductility the opposite was true. The Modified Johnson-Cook constitutive relation and the Cockcroft-Latham fracture criterion were calibrated using the material data obtained from the tensile tests. By inverse modeling, the model constants were tuned until wanted material behaviour was obtained.</p> <p>Ballistic impact experiments were conducted at room temperature and at -40 °C. The target plates were subjected to impacts using 7.62 mm APM2 bullets. The objective was to determine the ballistic limit curve by curve fitting the Recht-Ipson model to the experimental data. Only a minor positive effect on the ballistic limit velocity was observed for the lowest temperature. The failure modes were shown to be more sensitive to different initial velocities than temperature inside the tested range.</p> <p>Numerical analyses were conducted using IMPETUS Afea Solver with the model constants obtained from the inverse modeling. The simulations gave good results for the ballistic limit velocity and they were able to capture the trends seen in the experiments with regards to failure modes. Ductile hole growth was shown to be the main failure mode for both materials at various temperatures. A sensitivity study was performed to see how sensitive the base models were to changes in different parameters.</p>
--


RESPONSIBLE TEACHER:	Professor Tore Børvik
SUPERVISOR(S):	Professor Tore Børvik and Post PhD Jens Kristian Holmen
CARRIED OUT AT:	SIMLab, The Department of Structural Engineering, NTNU





## MASTEROPPGAVE 2017

FAGOMRÅDE: Beregningsmekanikk	DATO: 11. juni 2017	ANTALL SIDER: 129 20+98+11
----------------------------------	------------------------	-------------------------------

TITTEL: <b>Perforering av stålplater ved forskjellige temperaturer</b>	
UTFØRT AV:  Daniel Gulbrandsen	

SAMMENDRAG: <p>Hovedmålet med denne oppgaven var å undersøke hvordan temperaturen påvirker perforeringsmotstanden til det høyfaste stålet ArmoX 500T og det lavfaste stålet NVE 36. Dette ble gjort både eksperimentelt og numerisk.</p> <p>Strekktester ble utført ved romtemperatur for å karakterisere materialoppførselen til begge materialene i romtemperatur. ArmoX 500T visste seg å ha en flytspenning på rundt fire ganger så mye sammenlignet med NVE 36, det motsatte var tilfelle for duktiliteten. Den modifisert Johnson-Cook materialmodellen og Cockcroft-Latham bruddmodellen ble kalibrert basert på materialdataene funnet fra strekktestene. Ved hjelp av inversmodellering ble modellkonstantene tunet til ønsket materialoppførselen var oppnådd.</p> <p>Ballistiske eksperimenter ble gjennomført ved romtemperatur og ved <math>-40\text{ }^{\circ}\text{C}</math>. Platene ble utsatt for skudd med 7.62 mm APM2 kuler ved ulike initialhastigheter. Målet var å finne den ballistiske kurven ved å linjetilpasse Recht-Ipson modellen til de eksperimentelle dataene. En liten positiv forskjell ble observert for den ballistiske grensen ved <math>-40\text{ }^{\circ}\text{C}</math> sammenlignet med romtemperatur. Bruddmodene visste seg å være mer sensitive for en endring i initialhastighet enn for endringer i temperaturer innenfor det testede område.</p> <p>Numeriske analyser ble utført i IMPETUS Afea Solver med modellkonstantene funnet fra invers modelleringen. Simuleringene ga gode resultater for den ballistiske grensen og de var i stand til å gjenskape trendene i bruddmoder som ble observert under eksperimentene. Duktilt brudd visste seg å være hoved bruddmoden for begge materialene ved begge testtemperaturer. Et sensitivitetsstudie ble utført for å se hvor sensitiv de numeriske modellene var for en endring i forskjellige parametere.</p>
---

FAGLÆRER:	Professor Tore Børvik
VEILEDER(E):	Professor Tore Børvik og post ph. d. kandidat Jens Kristian Holmen
UTFØRT VED:	SIMLab, Institutt for konstruksjonsteknikk, NTNU



## **MASTER'S THESIS 2017**

for

Daniel Gulbrandsen

### **Perforation of Steel Plates at Various Temperatures**

#### **1. INTRODUCTION**

Steel is a widely used structural material, but its mechanical properties can change considerably over a small temperature range. This is called the ductile-to-brittle transition: At low temperatures steel may be brittle and fails by cleavage, while at higher temperatures steel is ductile and fails by micro-void coalescence. Other factors that may affect the transition are the stress state and the strain rate. This transition from ductile to brittle behavior is important to be aware of in practical applications, for example in arctic environments. In this research project the behavior of low- and high-strength steel plates will be investigated at temperatures above and below the ductile-to-brittle transition temperature. In addition to this, impact tests will be conducted in the ballistic laboratory where the steel plates are inserted in a newly developed temperature chamber and cooled with the help of liquid nitrogen.

#### **2. OBJECTIVES**

The primary objective of the research project is to investigate (both experimentally and numerically) the impact behavior of the low-strength steel NVE 36 and the high-strength steel ArmoX 500 T at various temperatures.

#### **3. A SHORT DESCRIPTION OF THE RESEARCH PROJECT**

The main topics in the research project will be as follows:

1. The candidate will conduct a study of relevant literature concerning the impact behavior of steel plates at various temperatures, constitutive modeling of metallic materials, and failure modeling.
2. Tension specimens with varying geometries are tested to characterize the materials at room temperature. Alternatively, material data for the steels should be found from the literature.
3. Ballistic penetration tests are conducted at selected temperatures in a temperature chamber. Here, the main idea is to check if the perforation resistance changes with temperature.
4. The candidate shall calibrate a modified Johnson-Cook (MJC) constitutive relation and a ductile failure criterion based on the room temperature test program, and validate this calibration with numerical simulations of all the tension and impact tests (at elevated temperatures).
5. Numerical simulations of the tests conducted at low temperature are done with one or more of the fracture criteria reported in the literature review.

*Supervisors:* Tore Børvik and Jens Kristian Holmen

The thesis must be written according to current requirements and submitted to Department of Structural Engineering, NTNU, no later than June 11<sup>th</sup>, 2017.

NTNU, January 15<sup>th</sup>, 2017

Tore Børvik  
Professor



# Preface

This thesis was a requirement for the degree of Master in Science in Civil and Environmental Engineering. The thesis was written at the Norwegian University of Science and Technology (NTNU) for the Structural Impact Laboratory (SIMLab) in the spring of 2017.

Trondheim, 11.06.2017

*Daniel Gulbrandsen*

---

Daniel Gulbrandsen





# Acknowledgements

First, I want to thank Engineer Tore Andre Kristensen from SINTEF for conducting the tensile tests. I would also like to thank Senior Engineer Trond Auestad for helping me with the ballistic impact experiments.

I would like to thank Dr. Lars Olovsson for giving me an introduction to IMPETUS Afea Solver. Additionally, thanks to Simulation Engineer Eric Lee at IMPETUS Afea Solver for answering my questions about issues in IMPETUS throughout the semester.

Thanks to Egil Fagerholt for helping me with the DIC pattern when conducting the tensile tests and for answering my questions about DIC measuring.

A big thanks to my supervisor, Post PhD Candidate Jens Kristian Holmen, for helping me with IMPETUS, answering my questions day and night, and for proofreading.

Lastly, a big thanks to my main supervisor, Professor Tore Børvik, for weekly meetings, guidance throughout the semester and for shearing your knowledge and experience.



# Abstract

The primary objective of this thesis was to investigate how the temperature affects the perforation resistance of the high-strength steel ArmoX 500T and the low-strength steel NVE 36. This was investigated both experimentally and numerically.

Tensile tests were conducted at room temperature to obtain the material properties for both materials. The ArmoX 500T was shown to have a yield stress of about four times the yield stress of the NVE 36 steel, while for the ductility the opposite was true. The Modified Johnson-Cook constitutive relation and the Cockcroft-Latham fracture criterion were calibrated using the material data obtained from the tensile tests. By inverse modeling, the model constants were tuned until wanted material behaviour was obtained.

Ballistic impact experiments were conducted at room temperature and at  $-40\text{ }^{\circ}\text{C}$ . The target plates were subjected to impacts using 7.62 mm APM2 bullets. The objective was to determine the ballistic limit curve by curve fitting the Recht-Ipson model to the experimental data. Only a minor positive effect on the ballistic limit velocity was observed for the lowest temperature. The failure modes were shown to be more sensitive to different initial velocities than temperature inside the tested range.

Numerical analyses were conducted using IMPETUS Afea Solver with the model constants obtained from the inverse modeling. The simulations gave good results for the ballistic limit velocity and they were able to capture the trends seen in the experiments with regards to failure modes. Ductile hole growth was shown to be the main failure mode for both materials at various temperatures. A sensitivity study was performed to see how sensitive the base models were to changes in different parameters.



# Contents

<b>Preface</b>	<b>i</b>
<b>Acknowledgements</b>	<b>iii</b>
<b>Abstract</b>	<b>v</b>
<b>Contents</b>	<b>vii</b>
<b>Nomenclature</b>	<b>xi</b>
<b>1 Introduction</b>	<b>1</b>
<b>2 Theory</b>	<b>3</b>
2.1 Impact Mechanics . . . . .	3
2.1.1 Terminology . . . . .	3
2.1.2 Ballistic Velocity . . . . .	7
2.1.3 The Recht-Ipson Model . . . . .	7
2.2 Material Mechanics . . . . .	8
2.2.1 Stress and Strain Measurement . . . . .	8
2.2.2 The Modified Johnson-Cook Material Model . . . . .	10
2.2.3 The Ductile Cockcroft-Latham Fracture Criterion . . . . .	11
2.2.4 Brittle Fracture Criterion . . . . .	11
2.3 Fracture Mechanics . . . . .	12
2.3.1 Ductile Fracture . . . . .	12
2.3.2 Brittle Fracture . . . . .	13
2.3.3 Ductile to Brittle Transition . . . . .	14
2.4 State of the Art . . . . .	16

<b>3</b>	<b>Target Materials</b>	<b>17</b>
3.1	Armox 500T Steel . . . . .	17
3.1.1	Material Description . . . . .	17
3.1.2	Experimental Work . . . . .	18
3.1.3	Experimental Results . . . . .	19
3.2	NVE 36 Steel . . . . .	22
3.2.1	Material Description . . . . .	22
3.2.2	Experimental Work . . . . .	22
3.2.3	Experimental Results . . . . .	23
<b>4</b>	<b>Ballistic Impact Experiments</b>	<b>27</b>
4.1	Experimental Setup . . . . .	27
4.1.1	Rig . . . . .	27
4.1.2	Bullet . . . . .	30
4.2	Experimental Results . . . . .	31
4.2.1	Armox 500T Steel . . . . .	31
4.2.2	NVE 36 Steel . . . . .	39
4.3	Summary and Discussion . . . . .	45
<b>5</b>	<b>Calibration of Material Models</b>	<b>47</b>
5.1	Armox 500T Steel . . . . .	48
5.1.1	Direct Calibration of Material Model . . . . .	48
5.1.2	Inverse Modelling . . . . .	50
5.2	NVE 36 Steel . . . . .	53
5.2.1	Direct Calibration of Material Model . . . . .	53
5.2.2	Direct Calibration of Fracture Criterion . . . . .	54
5.2.3	Inverse Modelling . . . . .	54
5.3	Summary of Material Data . . . . .	57
<b>6</b>	<b>Numerical Analysis of the Component Tests</b>	<b>59</b>
6.1	Armox 500T Steel . . . . .	60
6.1.1	Base Model . . . . .	60
6.1.2	Sensitivity Study . . . . .	68
6.1.3	Effect of Temperature . . . . .	73
6.2	NVE 36 Steel . . . . .	76
6.2.1	Base Model . . . . .	76

6.2.2	Sensitivity Study . . . . .	82
6.2.3	Effect of Temperature . . . . .	86
6.3	Summary and Discussion . . . . .	89
<b>7</b>	<b>Concluding Remarks</b>	<b>91</b>
<b>8</b>	<b>Further Work</b>	<b>93</b>
	<b>Bibliography</b>	<b>95</b>
<b>A</b>	<b>Armox 500T Steel</b>	<b>99</b>
A.1	Bullet Holes, RT . . . . .	100
A.2	Bullet Holes, -40 °C . . . . .	101
A.3	Front and Backside, RT . . . . .	102
A.4	Front and Backside, -40 °C . . . . .	103
<b>B</b>	<b>NVE 36 Steel</b>	<b>105</b>
B.1	Bullet Holes, RT . . . . .	106
B.2	Bullet Holes, -40 °C . . . . .	107
B.3	Front and Backside, RT . . . . .	108
B.4	Front and Backside, -40 °C . . . . .	109





# Nomenclature

$\alpha$	Pitch in the vertical plane
$\beta$	Pitch in the horizontal plane
$\chi$	Taylor-Quinney coefficient
$\Delta T$	Change in temperature
$\dot{p}$	Plastic strain rate
$\dot{p}^*$	Dimensionless plastic strain rate
$\dot{p}_0$	Reference plastic strain rate
$\gamma$	Yaw angle
$\omega$	Damage parameter
$\rho$	Material density
$\sigma^*$	Stress triaxiality
$\sigma_{0.2}$	0.2% offset yield stress
$\sigma_0$	Initial yield stress
$\sigma_1$	Major principal stress
$\sigma_1, \sigma_2, \sigma_3$	Principal stress
$\sigma_{eq}$	Equivalent von Mises stress
$\sigma_f$	True stress at failure
$\sigma_H$	Hydrostatic stress

$\sigma_t$	True stress
$\sigma_u$	True stress at necking
$\sigma_{VM}$	Von Mises stress
$\theta$	Impact angle
$\theta_L$	Lode angle
$\varepsilon^e, \varepsilon^p$	Elastic and plastic strain
$\varepsilon_A$	Almansi strain
$\varepsilon_f$	Logarithmic strain at failure
$\varepsilon_G$	Green strain
$\varepsilon_l$	Logarithmic strain
$\varepsilon_u$	Logarithmic strain at necking
$\varepsilon_v$	Volumetric strain
$\varphi$	Oblique angle
$A$	Current cross section area
$A$	Material constant Power law
$a$	Half crack length
$a$	Parameter in Recht-Ipson
$a/R$	Brigdman constant
$A_0$	Initial cross section area
$B$	Material constant Power law
$C$	Material constant MJC
$C_p$	Specific heat
$C_{Ri}$	Material constant Voce law

$C_V$	Absorbed energy
$D_{x,0}$	Initial diameter $x$ -direction
$D_x$	Current diameter $x$ -direction
$D_{y,0}$	Initial diameter $y$ -direction
$D_y$	Current diameter $y$ -direction
$E$	Youngs's modulus
$F$	Force
$G_1$	Strain energy release rate
$K$	Bulk modulus
$K$	Stress intensity factor
$L$	Current length
$L_0$	Initial length
$m$	Material constant MJC
$m_{pl}$	Mass of plug
$m_p$	Mass of projectile
$n$	Material constant Power law
$p$	Equivalent plastic strain
$p$	Hydrostatic pressure
$p$	Parameter in Recht-Ipson
$Q_{Ri}$	Material constant Voce law
$T$	Current temperature
$T^*$	Homologous temperature
$T_m$	Melting temperature

$T_r$	Reference temperature
$v_{bl}$	Ballistic velocity
$v_i$	Initial velocity
$v_r$	Residual velocity
$W_C$	Cockcroft-Latham parameter
Afea	Advanced Finite Element Analysis
CL	Cockcroft-Latham
DIC	Digital Image Correlation
fps	Frames per second
JC	Johnson-Cook
MJC	Modified Johnson-Cook
NTNU	Norwegian University of Science and Technology
RT	Room temperature (20 °C)
SIMLab	Structural Impact Laboratory
SINTEF	The Foundation for Scientific and Industrial Research

# Introduction

Protection against small-arms bullets has been an area of research worldwide for a long time. Different materials and alloys have been tested, but steel is still often the preferred material in design of protective structures, both for military and non-military use. The main reason for this is that steel has good ballistic properties due to its high material strength and ductility compared to other protective alloys [9]. Additionally, steel is known to have good formability and has a low cost.

Small-arms impact at high velocities is known to be a complex problem, due to rapid loading. Dynamic effects like material rate-dependency, stress wave propagation and inertia forces have to be considered. In addition, the effects of contact, temperature, stress triaxiality and material failure affect the results. In this thesis the purpose was to investigate how the temperature affects the ballistic behaviour of two steels with different material strength. Steel is usually ductile at room temperature (RT), but under a certain temperature called the ductile to brittle transition temperature (DBTT) it might become brittle. For structures that are built in an arctic environment where the temperature could be down to and even below -40 °C, this ductile-brittle temperature is important to be aware of.

The steels investigated, both experimentally and numerically, were the high strength steel Armox 500T and the low strength structural steel NVE 36.

A summary of each chapter is given below to give the reader an overview over the thesis:

**Chapter 2, Theory:** A short introduction to impact mechanics, material mechanics, fracture mechanics and previous studies relevant to this thesis are presented.

**Chapter 3, Target Materials:** Short presentations of each material tested are given. Then experimental methods and results from the tensile tests are presented.

**Chapter 4, Ballistic Impact Experiments:** A brief description of the ballistic impact experiment setup is given. Then the test results for both materials at different temperatures are presented and at last the results are discussed.

**Chapter 5, Calibration of Material Models:** Based on the results from the tensile tests, the material models for the two materials are calibrated. Two approaches are presented, direct calibration and inverse modelling.

**Chapter 6, Numerical Analysis of the Component Tests:** In this chapter the numerical analysis of the two base models using IMPETUS Afea Solver are presented. The results from a sensitivity study are discussed.

**Chapter 7, Concluding Remarks:** Here a short summary of results and conclusions are given. This includes both experimental and numerical work.

**Chapter 8, Further Work:** Suggestions for further work are given.

# Theory

Chapter 2 presents relevant theoretical background for this thesis. First, a brief introduction to impact mechanics and necessary ballistic terminology is given. Then, a short description of material mechanics and fracture mechanics is presented. Lastly, some earlier works on the same topic are summarised.

## 2.1 Impact Mechanics

*Impact* is defined as the collision between two or more solids, where the interaction between the bodies can be elastic, plastic or fluid, or any combination of these [5]. Additionally, Børvik et al. [5] defines *ballistics* as the art of accelerating bodies by use of some kind of an engine. Modern science ballistics is often related to projectiles accelerated from firearms [5].

### 2.1.1 Terminology

Ballistics is divided into three main research areas: interior, exterior and terminal ballistics. Interior and exterior include the motion and forces acting on the projectile in the launcher and during free flight. In this thesis the focus is on the terminal ballistics area which describes the interaction between the target and the projectile. Terminal ballistics is the area of most interest with respect to fortification, which may be defined as structures used for additional strengthening, especially in military defences [5].

A *projectile* is defined by Zukas [39] as any item that can be launched. Depending on the material, projectiles are often categorized as soft, semi-hard or hard. Further, they can be characterized by the material density, flight orientation, initial geometry and final condition.

In this thesis the projectile that is studied is a bullet. For a bullet the nose shape is an important parameter in impact mechanics since it has a significant effect on the penetration properties. Figure 2.1 illustrates some typical nose shapes, among them is the ogival nose which is used in the experimental and numerical work.

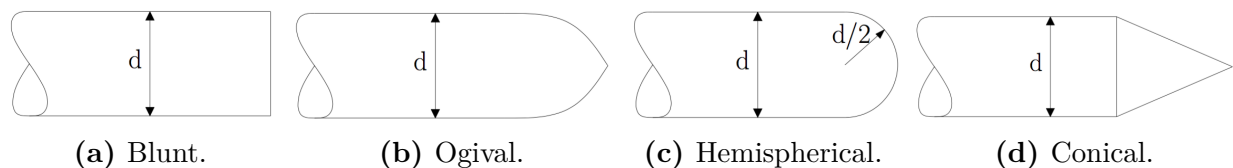


**Figure 2.1:** Examples of different nose shapes. Adapted from Børvik et al. [5].

According to Backman and Goldsmith [2] the initial velocity is an important parameter in impact mechanics. They divided the impact velocities into the following ranges; low velocity regime (0-50 m/s), sub-ordnance velocity regime (50-500 m/s), ordnance velocity regime (500-1300 m/s), ultra-ordnance velocity regime (1300-3000 m/s) and hypervelocity regime ( $\geq 3000$  m/s). This thesis deals with velocities in the sub-ordnance and ordnance ranges. For ordnance velocity impacts hardly no global deformation of the target is seen. Almost all of the kinetic energy is converted into local plastic work.

A *target* is defined as any moving or stationary object struck by the projectile [5]. Backman and Goldsmith classified the target by thickness and used the following categories [2]:

1. *Thin* is when the stress and deformation gradients are so small over the thickness that they can be neglected.
2. *Intermediate* is when the rear surface has a large effect on the deformation process during perforation.
3. *Thick* is when the rear surface only affects the penetration process after deep penetration.
4. *Infinite* is when the penetration process is not affected by the distal boundary.

*Penetration* is defined as the entry of a projectile into any region of a target [2]. The process can be divided into three categories:

1. *Perforation* is when the projectile passes through the target.
2. *Embedment* is when the target stops the projectile from passing through.



3. *Ricochet* is when the target deflects the projectile.

During impact the target material may deform or fail in different ways. It depends on variables such as impact velocity, target material, projectile shape and trajectory and the relative dimensions between the target and the projectile. Target response is often divided into non-perforating deformation modes and perforating failure modes. Non-perforating deformation modes typically consist of bulging, dishing and cratering. In this thesis the perforating failure modes are most relevant.

A combination of several failure modes are usually observed, but often one failure mode is dominating the failure process. The most common failure modes can be seen in Figure 2.2 and are described in short below.

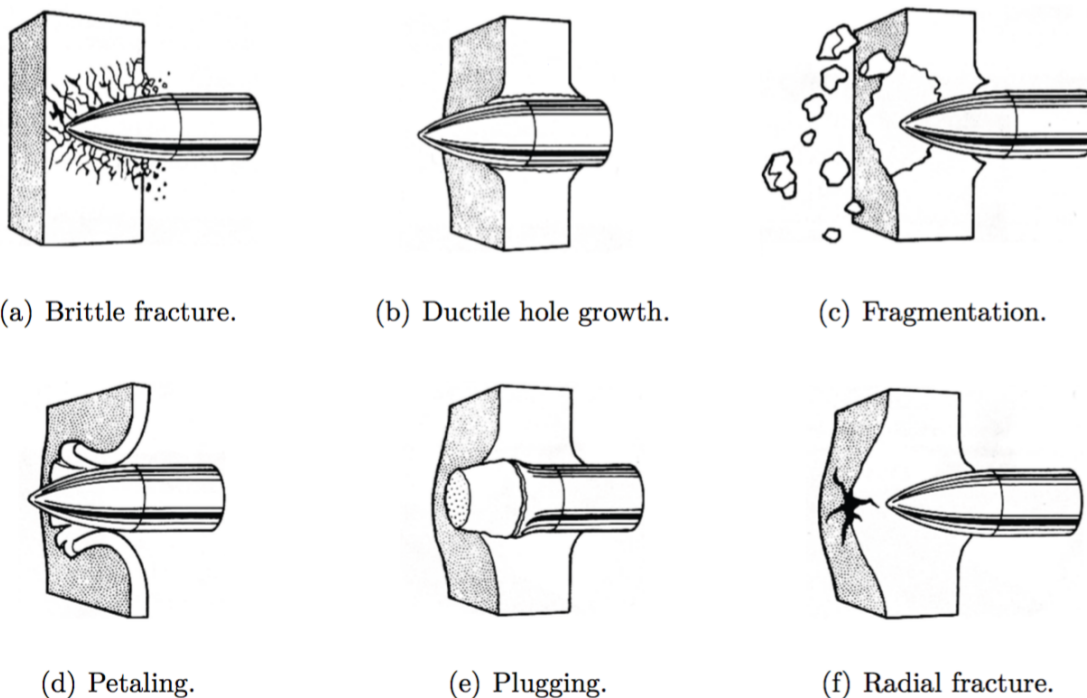


**Figure 2.2:** Different failure modes for thin and intermediate plates [5].

- Brittle fracture: This failure mode occurs when tensile stresses are reflected from compressive stress waves at the rear surface under perforation. Occurs typically for materials that are weak in tension.
- Ductile hole growth: This failure mode occurs when pointed nosed projectiles impact ductile materials. Under perforation the bullet moves the material because of the high radial pressure resulting in a thicker area near the hole.

- Fragmentation: High local stresses over a short time span obtained from high impact energies causes fragmentation. Mostly observed for brittle materials, but may also occur in high-strength metals at low temperatures when the impact velocity, triaxiality and strain rates are high enough.
- Petaling: High radial and circumferential tensile stresses near the projectile tip caused by bending moments result in petals. Petaling often occurs when projectiles with low velocity and pointed nose shape impact thin metal plates.
- Plugging: Impacts where blunt nosed projectiles establishes a high shear gradient over the target thickness which pushes out a plug approximately equal to the diameter of the projectile.
- Radial fracture: Tensile stresses are built up due to compressive waves that propagates from the impact point. If the tensile stresses are larger than the material strength radial cracks may occur. Happens typically for glass, ceramics and concrete.

By one single parameter, yaw ( $\gamma$ ), the flight orientation of a projectile can be described [22]. Yaw is defines as

$$\gamma = \arctan(\tan^2 \alpha + \tan^2 \beta)^{\frac{1}{2}} \quad (2.1)$$

where  $\alpha$  is the pitch in the vertical plane and  $\beta$  is the pitch in the horizontal plane. In this thesis only the vertical plane is considered,  $\beta$  is therefore assumed zero. So Equation 2.1 becomes,  $\gamma = \alpha$ . In Figure 2.3 the different angles to describe how a bullet hits a target plate are defined.  $\theta$  is the impact angle and is the angle between the target normal and the axis of symmetry.  $\varphi$  is the oblique angle and is the angle between the velocity vector and the target normal. A normal impact is defined as  $\gamma = \varphi = \theta = 0$

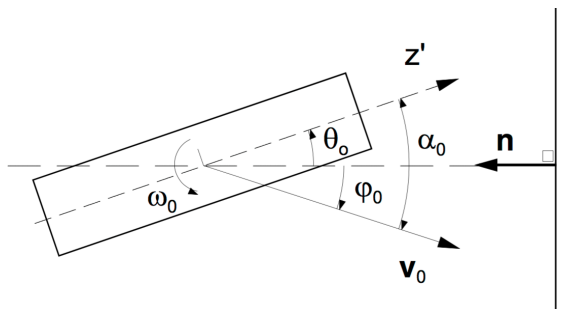


**Figure 2.3:** Definition of pitch ( $\alpha$ ), impact ( $\theta$ ) and oblique angle ( $\varphi$ ). Adapted from Børvik et al. [5].

### 2.1.2 Ballistic Velocity

In design of protective structures the ballistic limit velocity,  $v_{bl}$ , is an important parameter. It is defined as the average of the highest velocity that does not lead to perforation and the lowest velocity that does lead to perforation [5]. The relation between the residual ( $v_r$ ) and initial velocity ( $v_i$ ) gives the ballistic limit curve, as shown as the continuous line in Figure 2.4. The red dotted line illustrates the ballistic limit line. This line is a special case of the ballistic limit curve for a target of zero thickness.

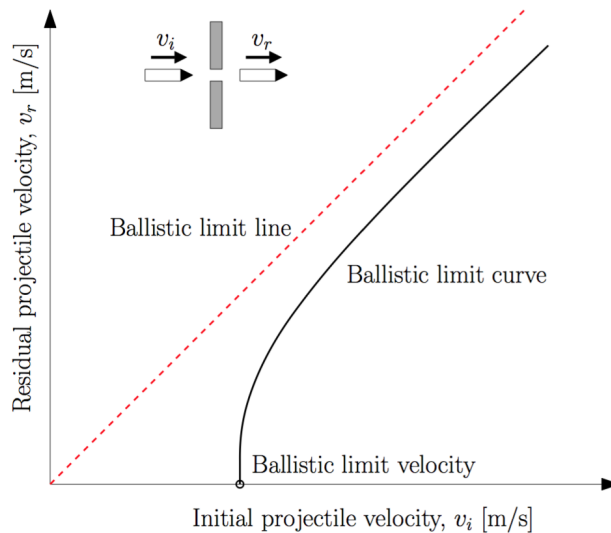


**Figure 2.4:** Ballistic limit line, limit curve and limit velocity [33].

### 2.1.3 The Recht-Ipson Model

Recht and Ipson [34] derived in 1963 an analytical model for the ballistic limit curve, based on the conservation laws of momentum and energy. Note that Recht and Ipson assumed ideal conditions and therefore the model only gives an approximation of the residual velocity. The model gives the residual velocity as

$$v_r = \left[ \frac{m_p}{m_p + m_{pl}} \right] (v_i^2 - v_{bl}^2)^{\frac{1}{2}} \quad (2.2)$$

where  $v_i$  is the initial velocity,  $v_{bl}$  is the ballistic velocity,  $m_{pl}$  is the mass of the plug and  $m_p$  is the mass of the projectile. For a full derivation see Børvik et al. [5]. For a perforation without plugging ( $m_{pl} = 0$ ) the first term in Equation 2.2 becomes unity.

Lambert and Jonas [39] made a more general version of the Recht-Ipson model in 1982, where the residual velocity is given by

$$v_r = a(v_i^p - v_{bl}^p)^{\frac{1}{p}} \quad (2.3)$$

where  $a$ ,  $p$  and  $v_{bl}$  are empirical constants found from experimental test data.

## 2.2 Material Mechanics

### 2.2.1 Stress and Strain Measurement

The Cauchy stress, better known as the true stress, may be introduced instead of the engineering stress where geometrical non-linearities take place. The engineering and the true stress are defined as

$$\sigma_e = \frac{F}{A_0}, \quad \sigma_t = \frac{F}{A} \quad (2.4)$$

where  $F$  is the measured force,  $A_0$  is the initial cross section area and  $A$  is the lowest current cross section area. For a circular specimen the initial and current cross section areas are calculated by

$$A_0 = \frac{\pi}{4} D_{x,0} D_{y,0}, \quad A = \frac{\pi}{4} D_x D_y \quad (2.5)$$

where  $D_x$  and  $D_y$  are the cross sectional diameters in  $x$  and  $y$  direction respectively.

For impact problems where large deformations take place a strain measure that fulfills the constraints of finite strain measures is needed [31]:

- For rigid body motions, like rotations and translations, the strain measure must be zero.
- For full compression the strains should converge to  $-\infty$  and for infinite stretching the strains should converge to  $\infty$ .
- For small deformations the strain should converge to the engineering strain.

In nonlinear structural problems the Almansi strain, the Green strain and the logarithmic strain are frequently used, but it is only the logarithmic strain that fulfills all the constraints for large strains. In this thesis the logarithmic strain will therefore be adopted. The Almansi

strain, the Green strain and the logarithmic strain are given by

$$\varepsilon_A = \frac{L^2 - L_0^2}{2L^2}, \quad \varepsilon_G = \frac{L^2 - L_0^2}{2L_0^2}, \quad \varepsilon_l = \ln \frac{L}{L_0} = \ln \frac{A_0}{A} \quad (2.6)$$

respectively. Where  $L_0$  is the initial length and  $L$  is the final length.

For a tensile specimen under tension loading the deformation localizes when the force reaches its maximum value,  $dF = 0$ , and for increasing elongation the cross-sectional area decreases rapidly. This phenomenon is called diffuse necking and occurs when

$$\frac{d\sigma_t}{d\varepsilon_l} = \sigma_t. \quad (2.7)$$

Then a notch takes place in the gauge area, as illustrated in Figure 2.5. This leads to a complex triaxial stress state in the neck, and the true stress differs from the equivalent stress. For a flat specimen diffuse necking marks the end of valid data. For circular specimens Bridgman [4] introduced a correction

$$\sigma_{eq} = \frac{\sigma_t}{(1 + 2R/a)[\ln(1 + (a/2R))]} \quad (2.8)$$

which compensates for the increasing longitudinal stresses produced in the notch. This gives an approximation of the uniaxial stress without introducing the triaxial stress state in the notch [19]. In Equation 2.8  $a$  is the diameter of the current cross section and  $R$  is the radius of the curvature. The equation

$$a/R = 1.1(\varepsilon_l^p - \varepsilon_{lu}^p), \quad \varepsilon_l^p > \varepsilon_{lu}^p \quad (2.9)$$

is an empirical expression for the relationship between  $a$  and  $R$  [30]. Where  $\varepsilon_u^p$  is the plastic strain at necking. The plastic strain can be found by subtracting the elastic strains from the logarithmic strain,

$$p = \varepsilon_l^p = \varepsilon_l - \frac{\sigma_t}{E}. \quad (2.10)$$

$E$  is Young's Modulus.

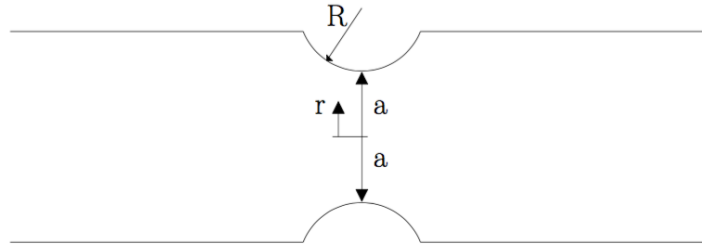


**Figure 2.5:** Notch introduced by diffuse necking [33].

## 2.2.2 The Modified Johnson-Cook Material Model

Johnson and Cook developed in 1983 a thermo-viscoplastic constitutive relation for metals subjected to large strains, high strain rates and high temperatures [29].

$$\sigma_{eq} = (A + Bp^n)(1 + C \ln \dot{p}^*)(1 - T^{*m}) \quad (2.11)$$

where  $A$ ,  $B$ ,  $n$ ,  $C$  and  $m$  are model constants.  $p$  is the equivalent plastic strain and  $\dot{p}^* = \dot{p}/\dot{p}_0$  is the dimensionless plastic strain rate, where  $\dot{p}$  is the plastic strain rate and  $\dot{p}_0$  is the reference plastic strain rate.  $T^* = (T - T_r)/(T_m - T_r)$  is the homologous temperature where  $T$  is the current temperature,  $T_r$  is the reference temperature and  $T_m$  is the melting temperature. The first term in Equation 2.11 describes the initial yield stress and the strain hardening, the second term describes the strain rate hardening and the third term captures the effect of temperature softening. To avoid numerical instabilities, which occur when  $\dot{p}^* < 1$ , a modified version of Johnson-Cook was proposed by Camacho and Ortiz in 1997 [13]. The logarithmic part in Equation 2.11 was replaced with  $(1 + \dot{p}^*)^C$ , and the modified Johnson-Cook is then given by

$$\sigma_{eq} = (A + Bp^n)(1 + \dot{p}^*)^C(1 - T^{*m}). \quad (2.12)$$

In this thesis two material hardening laws have been used; the Power hardening law and Voce hardening law. In Equation 2.11 and 2.12 the Power hardening law is used. By replacing the Power hardening law with the Voce hardening law, the modified Johnson-Cook is given by

$$\sigma_{eq} = \left( \sigma_0 + \sum_{i=1}^2 Q_{Ri}(1 - \exp(-C_{Ri}p)) \right) (1 + \dot{p}^*)^C(1 - T^{*m}) \quad (2.13)$$

where  $Q_{R1}$ ,  $C_{R1}$ ,  $Q_{R2}$ ,  $C_{R2}$  and  $m$  are model constants.

For fast transient problems the plastic dissipation leads to adiabatic heating [7]. The change in temperature is estimated as

$$\Delta T = \int_0^p \chi \frac{\sigma_{eq}}{\rho C_p} dp \quad (2.14)$$

where  $\rho$  is the material density,  $C_p$  the specific heat and  $\chi$  is the Taylor-Quinney coefficient. The Taylor-Quinney coefficient represents the amount of plastic work dissipated as heat. For metals  $\chi$  is typically 0.9 [7].

### 2.2.3 The Ductile Cockcroft-Latham Fracture Criterion

In 1968 Cockcroft and Latham [14] presented a one-parameter fracture criterion that depends on the stress state in addition to the plastic strains. The Cockcroft-Latham criterion (CL) only needs one single tensile test to be calibrated. It was shown by Dey et al. [15] that the CL criterion gives equally good or even better results than the Johnson-Cook fracture criterion. The CL criterion is given by

$$\omega = \frac{1}{W_C} \int_0^p \langle \sigma_1 \rangle dp = \frac{1}{W_C} \int_0^p \langle (\sigma^* + \frac{2}{3} \cos \theta_L) \sigma_{VM} \rangle dp \geq 1 \quad \Rightarrow \quad \text{ductile fracture} \quad (2.15)$$

where  $W_C$  is the fracture parameter,  $\sigma_{VM}$  is the von Mises stress and  $\theta_L$  is the Lode angle. In addition  $\sigma^* = \sigma_H / \sigma_{VM}$  is the stress triaxility, where  $\sigma_H$  is the hydrostatic stress.  $\langle \sigma_1 \rangle$  is the major principal stress and is defined as  $\max(\sigma_1, 0)$  which means that failure only can take place under tension dominated loading states. It should be noted that ductile fracture is highly sensitive to the stress triaxiality [12].

### 2.2.4 Brittle Fracture Criterion

Figure 2.6 illustrates three independent loading modes which can lead to fracture. The stress intensity at the crack tip is found by the stress intensity factor,  $K$ . For Mode 1 the stress intensity factor is defined as

$$K_1 = \sigma \sqrt{\pi a} \quad (2.16)$$

where  $a$  is the half crack length and  $\sigma$  is the remote tensile stress. Brittle fracture occurs when

$$\sigma_1 \geq \sigma_C \quad (2.17)$$

where  $\sigma_C$  is the critical stress. A rule of thumb says that the critical stress is about five times the yield stress [12]. To simulate brittle failure in IMPETUS Afea Solver two different criterions could be used. First, the strain energy release rate,  $G$ , could be defined in the ductile fracture criterion.  $G_1$  is related to  $K_1$  in the following way

$$G_1 = \frac{K_1^2}{E}. \quad (2.18)$$

The other possible method is the brittle fracture criterion given as

$$D = \frac{1}{t_s} \int_0^t H(\sigma_1 - \sigma_s) \left(\frac{\sigma_1}{\sigma_s}\right)^{\alpha_s} dp \geq 1 \quad (2.19)$$

where  $t_s$  is the time it takes for the fracture to initiate at the maximum principal stress,  $\sigma_s$  is the threshold stress to initiate fracture and  $\alpha_s$  is an exponent controlling the time to initiate fracture.

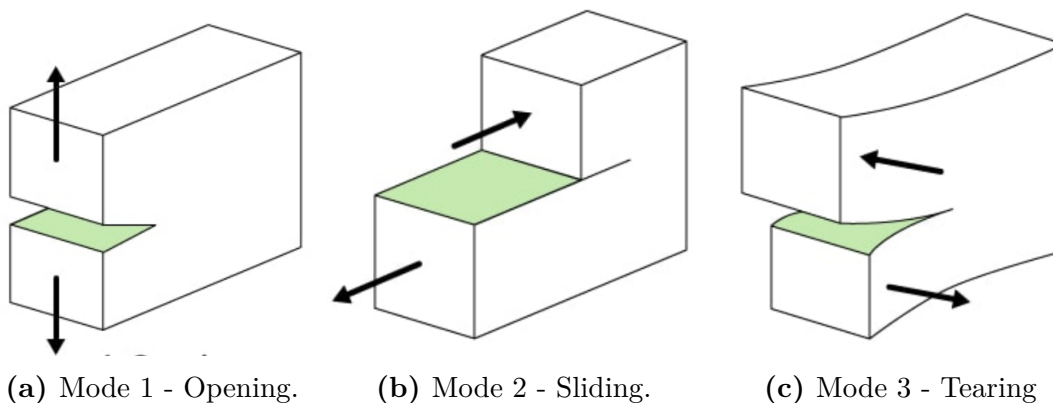


**Figure 2.6:** Three different fracture modes.

## 2.3 Fracture Mechanics

### 2.3.1 Ductile Fracture

Ductile fracture in metals is characterized by plastic deformation. The process consists of three main steps; void nucleation, growth and coalescence, as illustrated in Figure 2.7 [1]. The microscopic void is formed around a second-phase particle or inclusion when the applied stress is large enough to break the bonds between the matrix and the particle. In materials where the particles are well-bonded to the matrix, the fracture occurs soon after the voids are formed. If the bonds are weak, the fracture is controlled by growth and coalescence. Due



to hydrostatic stress and plastic strain the voids grow around the particles. When it reaches a critical value, a local plastic instability develops between the voids, which results in failure.

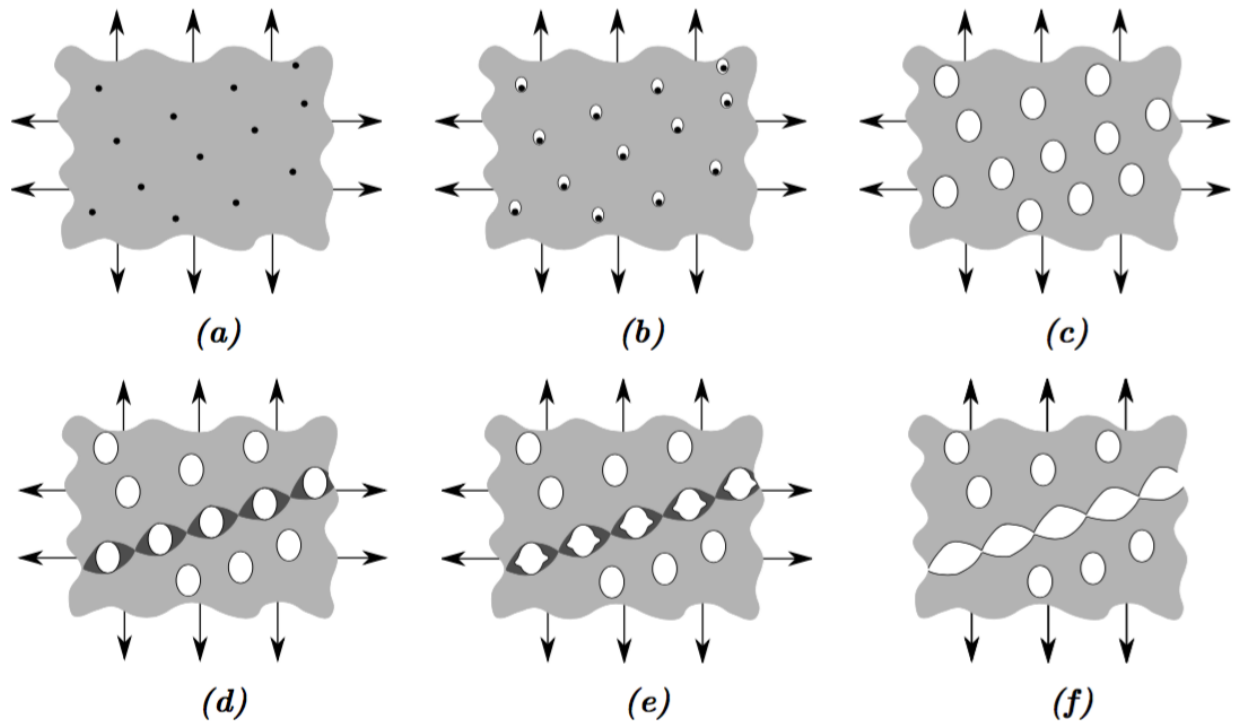


**Figure 2.7:** Void nucleation, growth and coalescence in ductile metals: (a) inclusions in a ductile material, (b) void nucleation, (c) void growth, (d) strain localization between voids, (e) necking between voids, and (f) void coalescence and fracture. Adapted from Anderson [1].

### 2.3.2 Brittle Fracture

Cleavage fracture is defined by Anderson [1] as the rapid propagation of a crack along a particular crystallographic plane. Hardly no plastic deformation is seen, and it may occur without any prior signs. Typical pure brittle materials are glass, ceramics, concrete and rock. Additionally, under the right conditions metals can also behave in a brittle manner. Factors that increase the probability for a brittle fracture of metals are low temperature, high strain rate and especially high triaxiality [19]. The preferred cleavage planes are the ones with the lowest packing density since the distance between the planes is greater and fewer bonds need to be broken. The crack grows perpendicular to the maximum principal stress direction. A face-centered cubic (FCC) metal, like aluminium, has many ductile slip systems at all temperatures and is therefore not susceptible to cleavage fracture. On the other hand, a body-centered cubic (BCC) metal, like steel, is susceptible to cleavage fracture when the

temperature is below the ductile-brittle transition temperature (DBTT). The reason for this is the few slip system in a BCC metal.

### 2.3.3 Ductile to Brittle Transition

For a small change in temperature the amount of absorbed energy ( $C_V$ ) that is required to get fracture can change drastically for a BCC metal. At low temperatures steel might be brittle and therefore fail by cleavage fracture. At high temperatures however, it fails by microvoid coalescence due to ductile material properties. The region where the metal transitions from ductile to brittle is called the ductile-to-brittle transition. In this temperature region a combination of brittle and ductile fracture micro-mechanisms take place. Figure 2.8 presents five different definitions of the ductile to brittle transition temperature [19]. The curve is obtained from Charpy tests conducted at different temperatures. The Charpy test is a widely used method to describe the relation between temperature and absorbed energy. For more information about Charpy impact tests see Holmen [27]. The list below describes the different definitions of the transition temperature in Figure 2.8.

- The transition temperature  $T1$  is defined as the temperature where the fracture is assumed to be purely ductile. No brittle micro-mechanisms are assumed to take place. This is the most conservative definition.
- $T2$  defines the temperature where the material fractures with 50% cleavage and 50% shear mechanisms.
- $T3$  is the average temperature between  $T1$  and  $T5$ .
- $T4$  is based on a random low value of  $C_V$ .
- $T5$  is defined as the temperature where the fracture becomes purely brittle. The probability for plastic deformation is negligible.

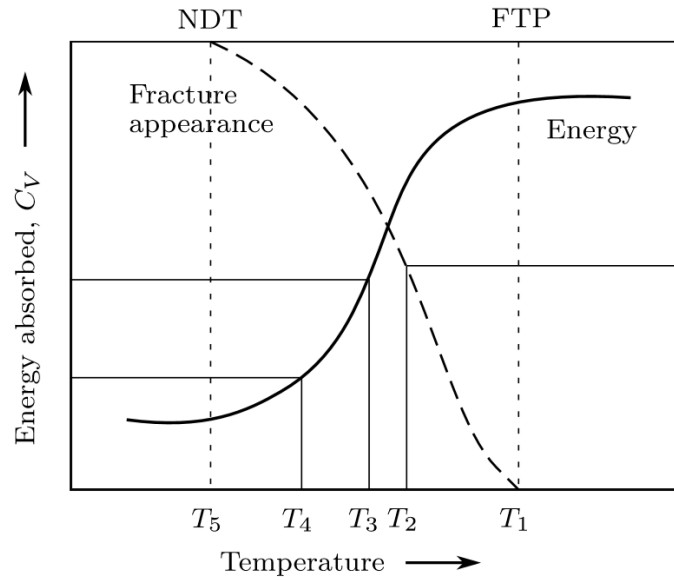


**Figure 2.8:** Ductile to brittle transition [19].

It is important to be aware of that the DBTT in steels is highly sensitive to chemical composition and microstructure. Earlier studies show that the amount of carbon and manganese has the largest effect on the DBTT [19]. The DBTT for mild steels are found when the  $C_V$  is 20 J. An increase of 0.1 weight % carbon raises the transition temperature with approximately 14 °C. On the other hand the same increase in weight % of manganese decreases the DBTT with about 5 °C. To preserve the material toughness the ratio between manganese and carbon should be higher than 3:1. In addition, the grain diameter has an influence on the transition temperature. By decreasing the grain size the transition temperature is decreased [19].

## 2.4 State of the Art

Terminal ballistics has been a heavily researched area world wide for a long time. This section presents relevant works for this thesis.

Small-arms impact at high velocities is known to be a complex problem due to non-linearities. Many factors are shown to affect the perforation process. Baker et al. [3] identified around 30 parameters, where plate thickness, material strength, impact velocity, projectile size and nose shape were shown to be important parameters.

In Børvik et al. [9] was five different high-strength steels; Weldox 500E, Weldox 700E, Hardox 400, Domex Protect 500 and ArmoX 560T, subjected to two different small-arms bullets, 7.62 mm Ball bullet and 7.62 mm APM2 bullet. They showed that there was a linear relation between the material strength and the ballistic resistance for impact velocities in the ordnance regime. Dey et al. [18] showed that a layered configuration (2 x 6 mm) of a Weldox 700E steel had better ballistic properties than a monolithic configuration (12 mm) subjected to ogival projectiles in the ordnance regime. Projectiles with a blunt nose-shape were shown to have the opposite effect. Goldsmith [22] performed a study on non-ideal projectile impacts. The results showed the projectiles penetration capacity were highly reduced for angles above 5°.

The studies mentioned above were performed at room temperature. The FV535 steel was investigated by Erice et al. [20] at elevated temperatures. Ballistic tests were conducted at RT, 400 °C and 700 °C. For the tests performed at 700 °C a significant reduction of the ballistic limit velocity was observed. Thomesen [36] investigated how the temperature affected the ballistic resistance of the high strength steel Strenx-960-Plus at low temperatures. The material was subjected to impacts with 7.62 mm APM2 bullets at temperatures between RT and -60 °C. A slight increase of the ballistic limit velocity was shown at low temperatures.

In this thesis the armour steel ArmoX 500T and the low strength steel NVE 36 will be investigated. The main objective is to provide better understanding of how temperatures at RT and -40 °C affects the ballistic resistance for a armour steel and for a low strength steel.

## Target Materials

Two different target materials were investigated in this thesis. These are the armour steel Armox 500T and structural steel NVE 36. This chapter contains a presentation of each material, a short description of test methods and results from the material experiments. In Table 3.1 an overview over quasi-static tensile tests conducted in this thesis is given.

**Table 3.1:** Overview over quasi-static tensile tests.

Material	Test orientation	Specimen type	Test name		
Armox 500T	0°	Dog Bone	Test 1, 0°	Test 2, 0°	Test 3, 0°
Armox 500T	90°	Dog Bone	Test 1, 90°	Test 2, 90°	Test 3, 90°
NVE 36	0°	Smooth	Test 1, 0°	Test 2, 0°	Test 3, 0°
NVE 36	90°	Smooth	Test 1, 90°	Test 2, 90°	Test 3, 90°

### 3.1 Armox 500T Steel

#### 3.1.1 Material Description

Armox 500T is a high-strength armour steel delivered from SSAB in Sweden. According to the manufacturer it is the toughest protection plate in the world and the material you want between you and the risk [35]. Typical applications are in military vehicles and buildings, but in the later years also in non-military structures. "500T" indicates a nominal HBW hardness of 500 and the material has a minimum yield stress of 1250 MPa. It is about four times the yield stress of the NVE 36 steel.

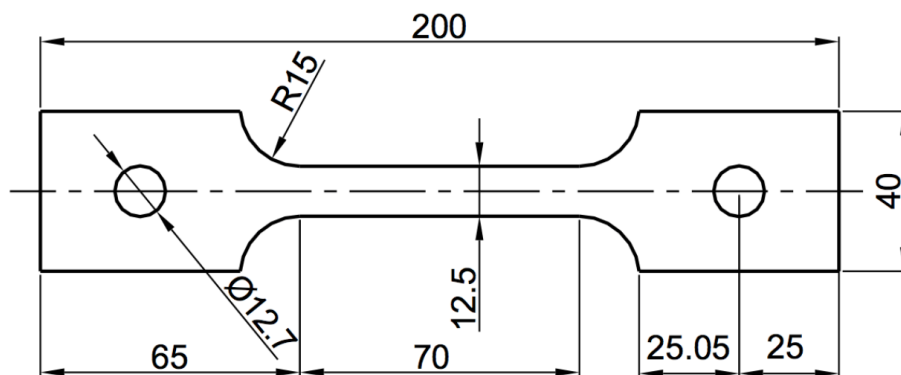
In Table 3.2 the chemical composition of Armox 500T is given. Note that concentrations less than 0.01 weight % are neglected.

**Table 3.2:** Chemical composition in weight % of Armox 500T.

	C	Si	Mn	P	Cr	Ni	Mo
Certificate	0.32	0.4	1.2	0.010	1.0	1.8	0.7

### 3.1.2 Experimental Work

The quasi-static tensile tests were carried out by Tore Andre Kristensen from SINTEF (The Foundation for Scientific and Industrial Research). Figure 3.1 illustrates the dog bone specimens used in the material experiments. They were extracted from rolled plates with a thickness of 3.5 mm. Note, the specimens were spark eroded from different plates than were used in the component tests in Chapter 4. The specimens were mounted in an Instron hydraulic test machine with a 100 kN load cell, as seen in Figure 3.2a. A displacement rate of 2.1 mm/min, corresponding to an initial strain rate of  $5 \cdot 10^{-4} \text{ s}^{-1}$ , was given the specimens.

**Figure 3.1:** Geometry of the dog bone specimen given in mm.

Digital imaging correlation, better known as DIC, was used to get an exact measurement of the displacements. DIC is a method that can track displacements by comparing an image at a deformed stage to an image from the initial configuration [21]. This requires that the surface has features which make every area unique. Each specimen was therefore painted with a random DIC pattern, as shown in Figure 3.2b. Pictures were continuously taken during the experiments with a frequency of 2 Hz. Furthermore, a vector, marked with the green line in Figure 3.2c, was added on the initial configuration like a virtual extensometer. By tracing the end nodes the displacement was found for each specimen. The force applied to the specimens was logged by the experiment computer and saved in a text document. In addition, strain and stress fields were obtained from inside the area marked with the red mesh, as seen in

Figure 3.2c. These fields were used as a validation for the numerical simulations.

To check the degree of in-plane anisotropy, the specimens were extracted from two different directions,  $0^\circ$  and  $90^\circ$ , with respect to the rolling direction of the plate. All tests were conducted at room temperature,  $T = 293$  K.

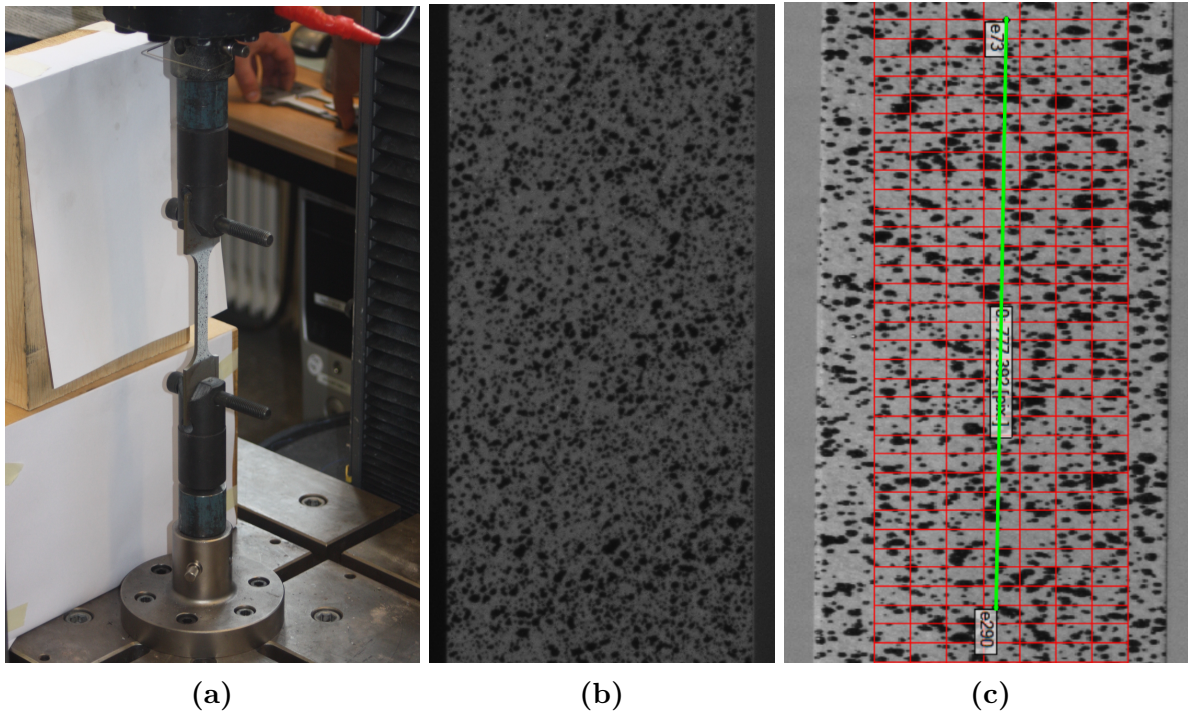


**Figure 3.2:** (a) Setup for the quasi-static tensile tests, (b) gauge area painted with a DIC pattern and (c) DIC pattern with virtual mesh and extensometer.

### 3.1.3 Experimental Results

A MATLAB script was used to process and plot the material data. In Figure 3.3a the force - displacement curves are plotted with displacements from DIC and load from the experiment computer. The tensile specimens seemed to behave almost identically up to necking,  $dF = 0$ , and then differ some. Small variations in fracture displacement were observed for the two directions. Using Equation 2.4 and 2.6, the true stress - logarithmic strain curve was found. Furthermore, a correction of the Young's modulus was performed since the measured value differed from the typical value for steels which is  $E = 210000$  MPa. The correction was calculated using

$$\varepsilon_c = \varepsilon_m + \Delta\varepsilon = \varepsilon_m + \frac{E_m - E_c}{E_m E_c} \quad (3.1)$$

where subscript  $m$  means the measured value from the experiments and  $c$  means the corrected value ( $E_c = 210000$  MPa). The zero-point for the strains was also adjust using  $\Delta\varepsilon$  and the relations in Figure 3.3b were obtained. It can be observed that the strain hardening, yield stress and necking strain for the two directions almost coincide. The tests show that the ArmoX 500T steel has a high yield stress of about 1300 MPa and a necking strain of 0.037. See Table 3.3 for more detailed data from each tensile test where  $\sigma_{0.2}$  is the yield stress,  $\sigma_u$  is the true stress at necking and  $\varepsilon_u$  is the logarithmic strain at necking. Note that the curves only contain data up to necking since only a virtual extensometer over the whole gauge area was used to measure the displacements.

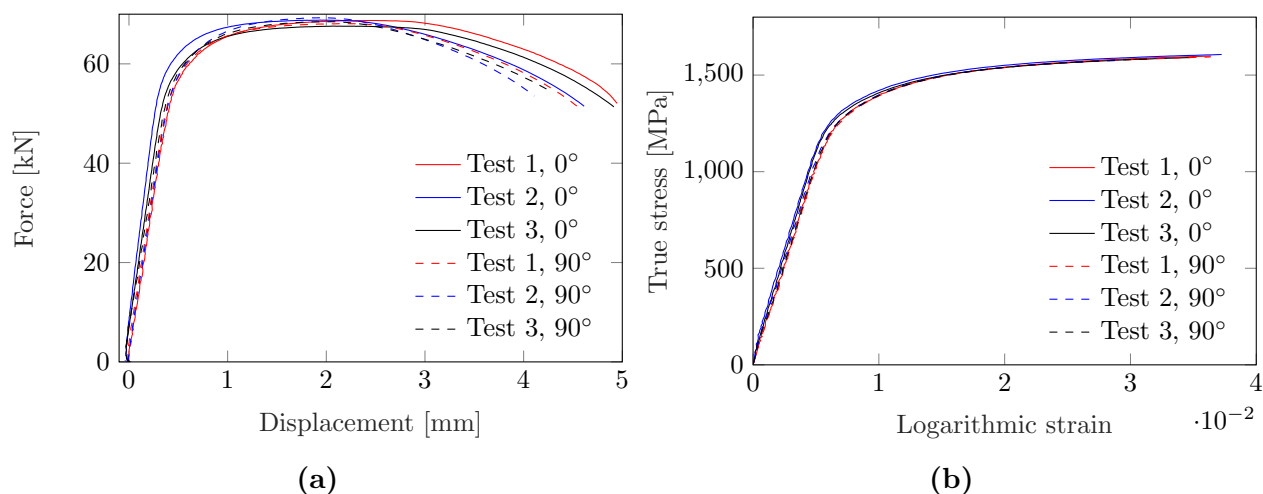


**Figure 3.3:** (a) Force - displacement relation and (b) true stress - logarithmic strain relation up to necking.

**Table 3.3:** Material data for each tensile test.

	$\sigma_{0.2}$ [MPa]	$\sigma_u$ [MPa]	$\varepsilon_u$
Test 1, 0°	1337	1599	0.036
Test 2, 0°	1364	1607	0.037
Test 3, 0°	1350	1592	0.035
Test 1, 90°	1326	1594	0.036
Test 2, 90°	1331	1575	0.029
Test 3, 90°	1334	1584	0.032

Figure 3.4 shows the specimens post fracture. Inclined shear seems to be the dominating fracture mode. Almost every specimen failed in a 45° direction with respect to the length direction. Some diffuse necking and a ductile behaviour were seen. Here, necking and fracture occurred at different places in the gauge area due to imperfections and small difference in the cross-section area for each specimen.



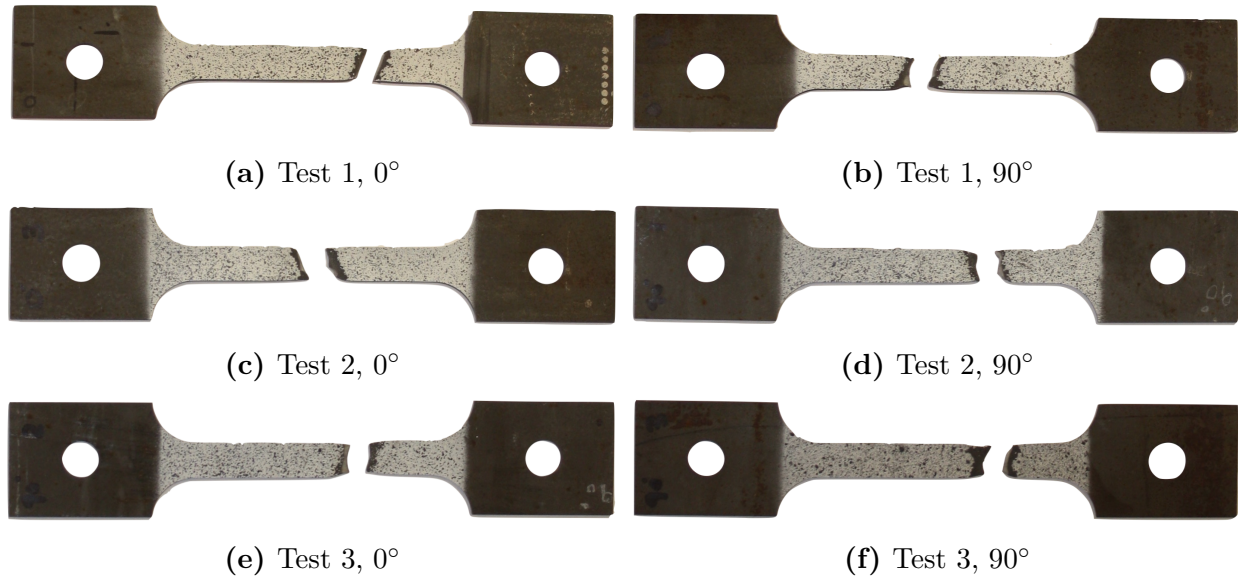


**Figure 3.4:** Armox 500T specimens after fracture.

## 3.2 NVE 36 Steel

### 3.2.1 Material Description

NVE 36 is a structural marine steel with a nominal yield stress of 355 MPa. Typical applications of these steel plates are in maritime structural components. As mentioned in Section 3.1.1, ArmoX 500T has about four times the yield stress of NVE 36, while for the ductility the opposite is true.

The chemical composition in weight % is given in Table 3.4. Note, also here concentrations less than 0.01 weight % are neglected.

**Table 3.4:** Chemical composition in weight % of NVE 36.

	C	Si	Mn	P	Al	Nb	Cr	Ni	Cu	Ti
Certificate	0.15	0.26	1.48	0.018	0.036	0.023	0.03	0.01	0.04	0.015

### 3.2.2 Experimental Work

The NVE 36 tensile tests were carried out earlier at NTNU by Orthe and Thorsen in their master thesis [33]. The raw data from the earlier tests, which contained force, diameter in  $x$  and  $y$  direction and time, were analysed and compared to the results from [33].

A Zwick/Roell Z030 hydraulic test machine with a 30 kN load cell was used for the quasi-static tensile tests. Note, also here the specimens were extracted from different directions ( $0^\circ$  and  $90^\circ$ ) and from different plates than those used in the ballistic experiments in Chapter 4. The smooth tensile specimens, shown in Figure 3.5, were mounted in the test machine (Figure 3.6a) and given a displacement rate of 1.2 mm/min. This corresponded to an initial strain rate of  $5 \cdot 10^{-4} \text{ s}^{-1}$ . During the tensile tests an AEROEL XLS 13XY Laser Micrometer measured continuously the smallest diameter in two principal directions, see Figure 3.6b. To ensure that the minimum cross-section area was measured, the laser was able to move in the vertical direction and every specimen was given a slightly smaller cross-section area in the centre of the gauge area. All the tests were conducted at room temperature,  $T = 293 \text{ K}$ .

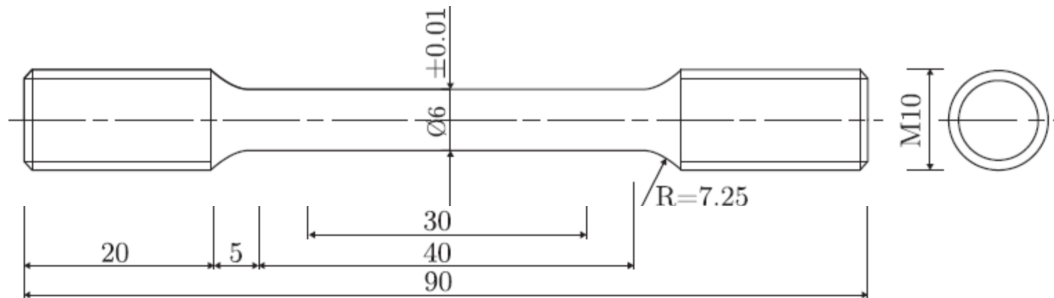


**Figure 3.5:** Geometry of the smooth test specimens given in mm.

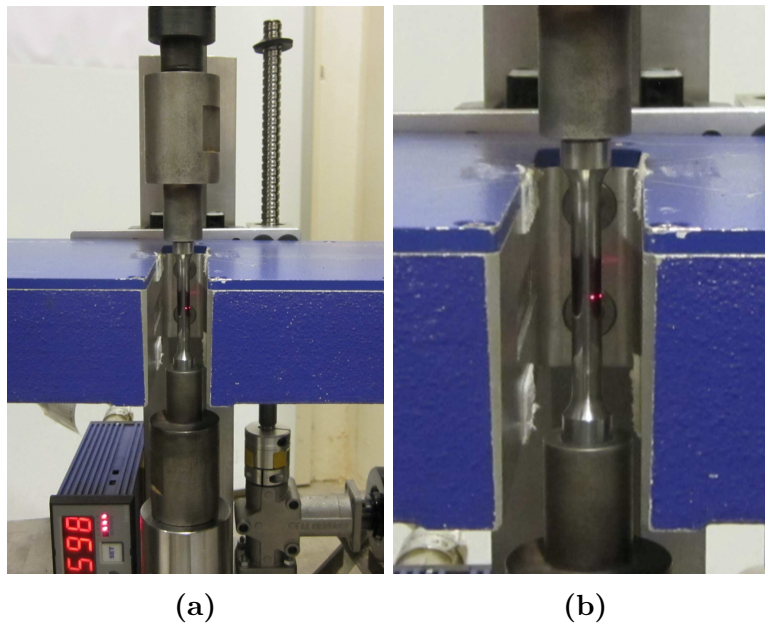


**Figure 3.6:** (a) Setup for the quasi-static tensile tests and (b) close up of AEROEL XLS 13XY Laser Micrometer.

### 3.2.3 Experimental Results

The six tensile tests performed on NVE 36 showed that the material hardening and yield stress almost coincided for each direction, this can clearly be seen in Figure 3.7a. The tests show that the material has a yield stress of about 400 MPa and a yield plateau shown in Figure 3.7b). This is a typical result for mild steels like NVE 36. Furthermore, it was observed that the 90° direction material behaves more ductile than the 0° direction material. A difference of about 30% in fracture strain was observed. Here, an anisotropic failure criterion could have been introduced, but it was not investigated in this thesis. In Chapter 6 a numerical sensitivity study was conducted and the sensitivity of the  $W_C$  parameter was checked. See

Table 3.5 for more detailed data for each tensile test where  $\sigma_{0.2}$  is the yield stress,  $\sigma_u$  is the true stress at necking,  $\varepsilon_u$  is the logarithmic strain at necking,  $\sigma_f$  is the true stress at failure and  $\varepsilon_f$  is the logarithmic strain at failure.

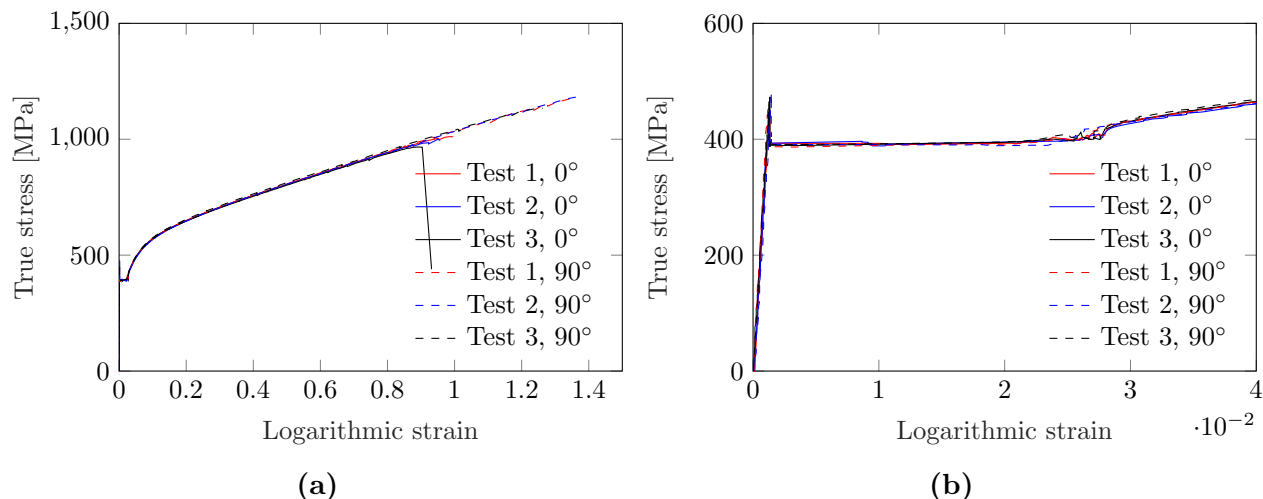


**Figure 3.7:** (a) True stress - logarithmic strain relation and (b) yield plateau.

**Table 3.5:** Material data for each tensile test.

	$\sigma_{0.2}$ [MPa]	$\sigma_u$ [MPa]	$\varepsilon_u$	$\sigma_f$ [MPa]	$\varepsilon_f$
Test 1, 0°	393	642	0.188	1011	0.996
Test 2, 0°	393	645	0.197	994.9	0.957
Test 3, 0°	390	631	0.174	965.5	0.904
Test 1, 90°	387	648	0.199	1171	1.360
Test 2, 90°	391	638	0.187	1183	1.367
Test 3, 90°	391	655	0.201	1134	1.263

To check if the material hardening was isotropic the  $r$ -value was obtained from the test data by using

$$r = \frac{d\varepsilon_x}{d\varepsilon_y} = \frac{\ln(D_y/D_0)}{\ln(D_x/D_0)} \quad (3.2)$$

As seen in Figure 3.8a and 3.8b the curves are close to unity. No variation is seen between the tests in the different directions and the  $r$ -value shows that the plastic flow is isotropic.

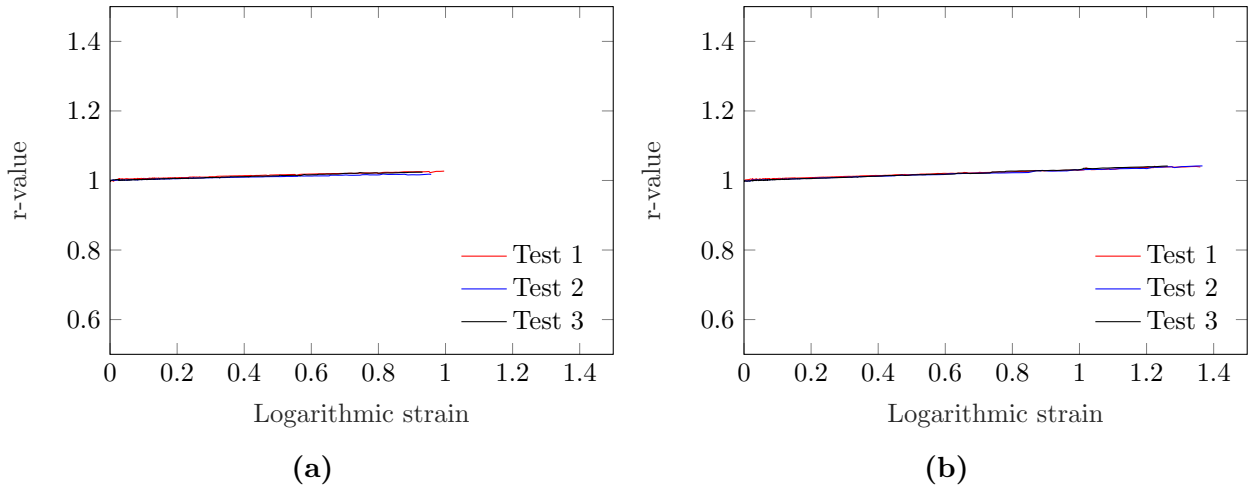


**Figure 3.8:**  $r$ -value versus logarithmic strain; (a)  $0^\circ$  direction and (b)  $90^\circ$  direction.

Pictures of the smooth specimens after fracture are shown in Figure 3.9. Here, necking and fracture occurred at the same place in each test due to a slightly smaller cross-section area at the middle of the gauge area. The material failed with a characteristic cup and cone fracture. This indicated a ductile material. Also, a large diffuse neck was observed for each specimen.



**Figure 3.9:** NVE 36 specimens post fracture.



## Ballistic Impact Experiments

This chapter presents the ballistic experiments conducted on the materials Armox 500T and NVE 36. For both materials the objective was to determine the ballistic velocity curve at different temperatures. Table 4.1 gives an overview of the experimental tests.

**Table 4.1:** An overview of ballistic impact experiments.

Material	Temperature	Number of tests
Armox 500T	RT (20 °C)	8
Armox 500T	-40 °C	5
NVE 36	RT (20 °C)	8
NVE 36	-40 °C	5
Total		26

### 4.1 Experimental Setup

#### 4.1.1 Rig

The ballistic impact experiments were conducted in a rig at the Department of Structural Engineering at NTNU by Trond Auestad. A 7.62 x 63 mm smooth-bored Mauser rifle with a barrel length of 1 m was used in the experiments. In order to ensure a well-defined impact point for each test the Mauser was mounted in a rigid rack. A remote trigger, as shown in Figure 4.2a, was used to safely fire the projectile inside a 16 m<sup>3</sup> chamber. Figure 4.1 illustrates the chamber.

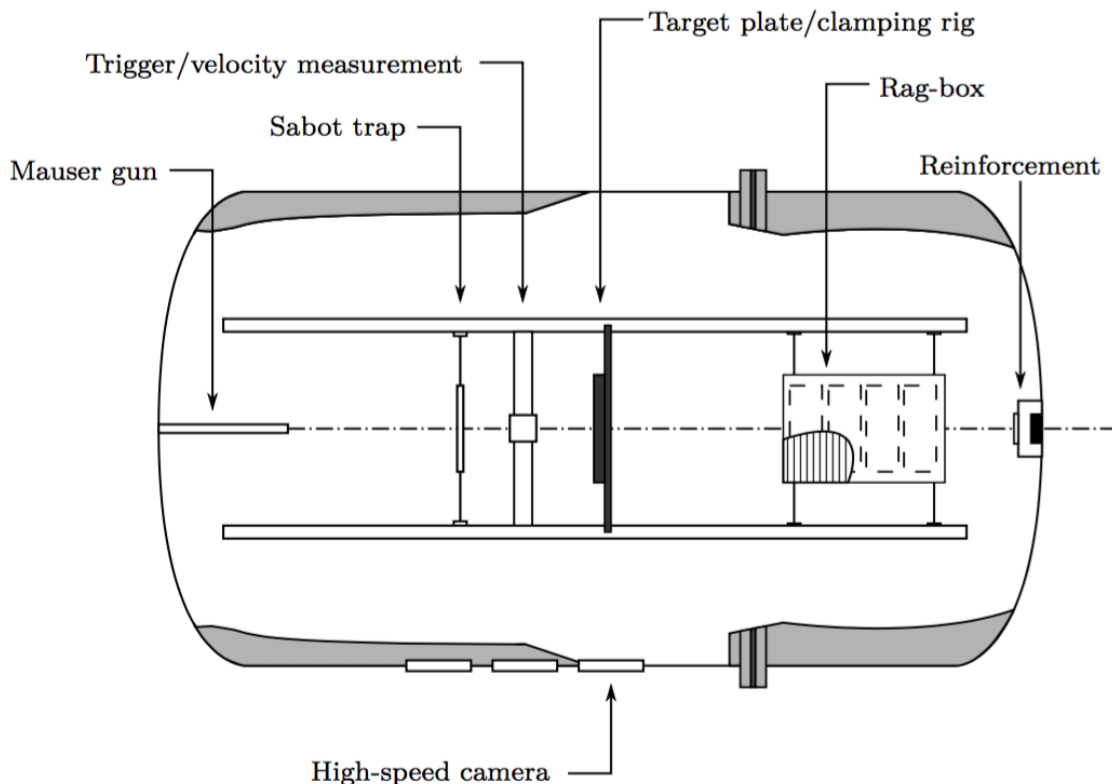


**Figure 4.1:** Sketch of the chamber. Adapted from Børvik et al. [8].

The target plates, with in-plane dimensions of  $300 \times 300 \text{ mm}^2$ , were clamped to a rigid frame inside the chamber, as seen in Figure 4.2b. Two transverse beams provided fixed boundary conditions for the horizontal sides of the plates. The vertical sides were free to move. As mentioned in Section 2.1.1 this thesis deals with velocities in the ordnance regime (500 m/s - 1000 m/s). For these impact velocities hardly no global deformation is seen and the boundary conditions are therefore of minor importance if the distance between the single shots are more than several projectile diameters [9]. Here, maximum four shots were fired per plate at RT and the distance between each shot was approximately 100 mm. For the experiments conducted at  $-40 \text{ }^\circ\text{C}$  only one plate was tested for each material to save time and nitrogen. Therefore, five shots were fired. Different plate thicknesses for the two materials were used in this study. For Armox 500T a laminated configuration with thickness  $2 \times 3.5 \text{ mm}$  was tested and for NVE 36 a monolithic configuration with thickness 6 mm was tested. The reason for this was the availability of the materials.

The Phantom V1610 high-speed camera with a frame rate of 75000 fps was used under each



test. The camera is shown in Figure 4.2c. The pictures were used to measure the initial and residual velocities. The camera was triggered when the projectile passed a metal sheet in front of the muzzle.

For the ballistic tests at  $-40\text{ }^{\circ}\text{C}$  a custom-built temperature chamber was installed inside the chamber. It was made of plexiglass and the dimensions were  $0.44\text{ m} \times 0.51\text{ m} \times 0.7\text{ m} = 0.157\text{ m}^3$ . In Figure 4.2d the temperature chamber is shown. Liquid nitrogen was injected from a tank to cool down the target plates. To ensure that the temperature was  $-40\text{ }^{\circ}\text{C}$  inside the chamber, sensors were placed on the plexiglass and directly onto the target plates. Furthermore, a 22 mm diameter hole was drilled in the front plate to make an opening for the projectile. In the back of the temperature chamber a polystyrene plate was mounted. The reasons for this was to make an exit path for fragments and for keeping the nitrogen inside the temperature chamber.

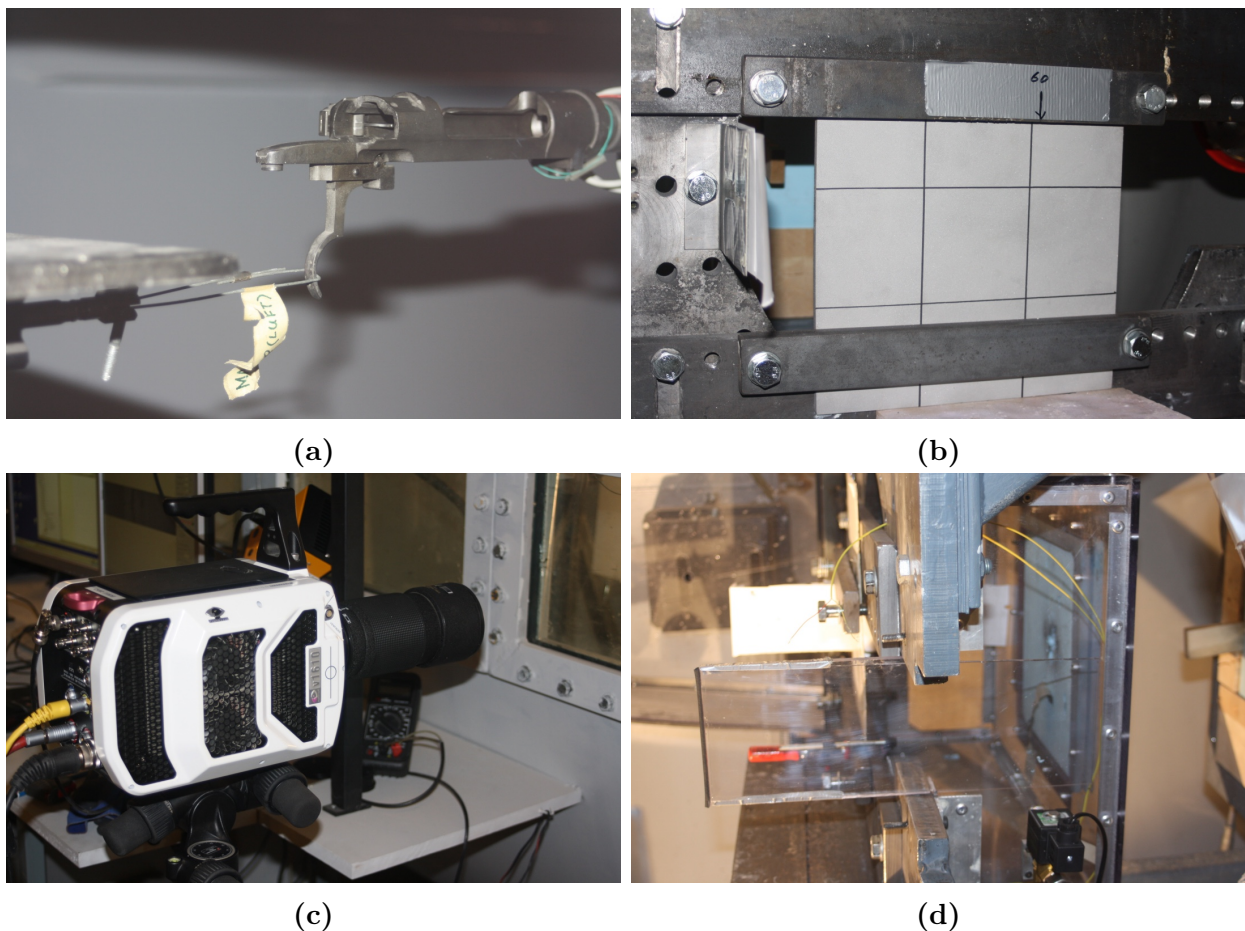


**Figure 4.2:** (a) Trigger mechanism, (b) rigid rig with two transverse beams, (c) Phantom V1610 high-speed camera and (d) temperature chamber.

### 4.1.2 Bullet

The projectile used was a 7.62 mm APM2 bullet with a total mass of about 10.5 g. The APM2 bullet consists of four parts; an ogival-nosed hardened steel core, a lead cap, an end cap and a brass jacket. Figure 4.3 illustrates the geometry of the projectile. In Table 4.2 the projectile material constants are presented. For more information about the APM2 bullet see Børvik et al. [9].

In order to determine the ballistic limit velocities different impact velocities were needed. For each shot the amount of gunpowder in the cartridge was adjusted to ensure that the projectile impacted the target with the desirable velocity.

**Table 4.2:** Material constants for each part of the APM2 bullet [9].

Material	$\rho$ [kg/m <sup>3</sup> ]	$E$ [MPa]	$\nu$
Hard steel core	7850	210000	0.33
Lead cap	10660	10000	0.42
Brass jacket	8520	115000	0.31

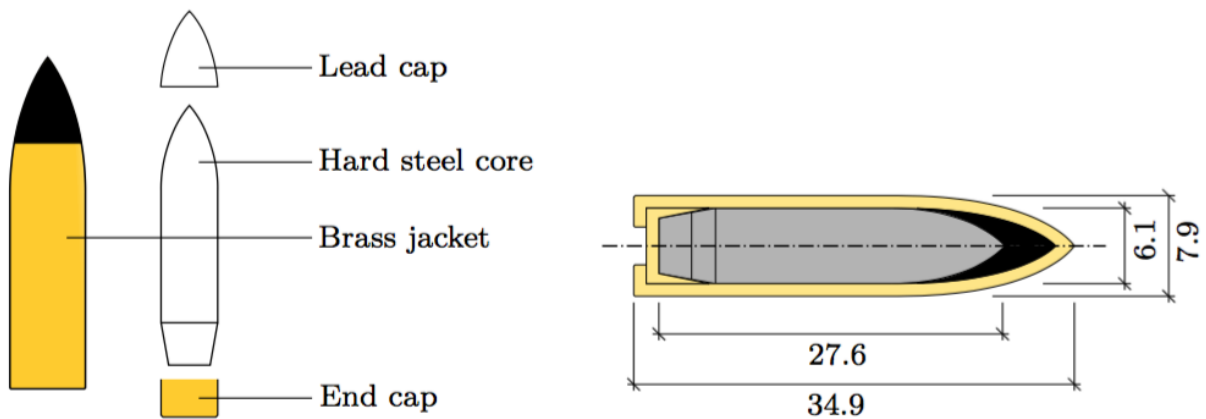


**Figure 4.3:** Schematic drawing and geometry of an APM2 bullet. Adapted from Børvik et al. [9].

## 4.2 Experimental Results

This section presents the results from the ballistic experiments. Both steels were tested with the same methods and at the same temperatures. The temperature effect will be examined and discussed.

With the least square method the ballistic limit curves were found by curve fitting the Recht-Ipson equation (Equation 2.3), described in Section 2.1.3, to the experimental data. Since the tests were performed with pointed nosed projectiles and mainly failed by ductile hole growth, the Recht-Ipson parameter,  $a$ , was set to unity. Note, some fragmentation was seen for impacts with an initial velocity around 900 m/s. The two other parameters in Recht-Ipson,  $p$  and  $v_{bl}$ , were curve fitted to the experimental data.

Time lapses were made for the highest impact velocity and for a velocity near the ballistic limit velocity for each material and temperature. The time lapses at -40 °C are a bit blurry because of condensation on the plexiglass inside the temperature chamber. In addition, front holes and back holes are presented to show differences in failure modes. Pictures of all front holes, back holes and target plates can be found in Appendix A and B.

### 4.2.1 Armox 500T Steel

Table 4.3 and 4.4 shows the results at RT and -40 °C respectively. All tests were successful, except of test number 7 at RT.

**Table 4.3:** Tabulated results - Armox 500T 2x3.5 mm plates at RT.

Test	Gunpowder [grain]	$v_i$ [m/s]	$v_r$ [m/s]	Comment
1	Full	879.5	735.1	OK
2	39.0	659.4	390.8	OK
3	33.0	569.7	232.7	OK
4	31.0	585.9	307.0	Projectile split in two
5	30.0	522.5	0	No exit
6	30.5	586.2	257.0	OK
7	30.0	-	-	No measurement, no exit
8	30.0	507.2	0.0	No exit

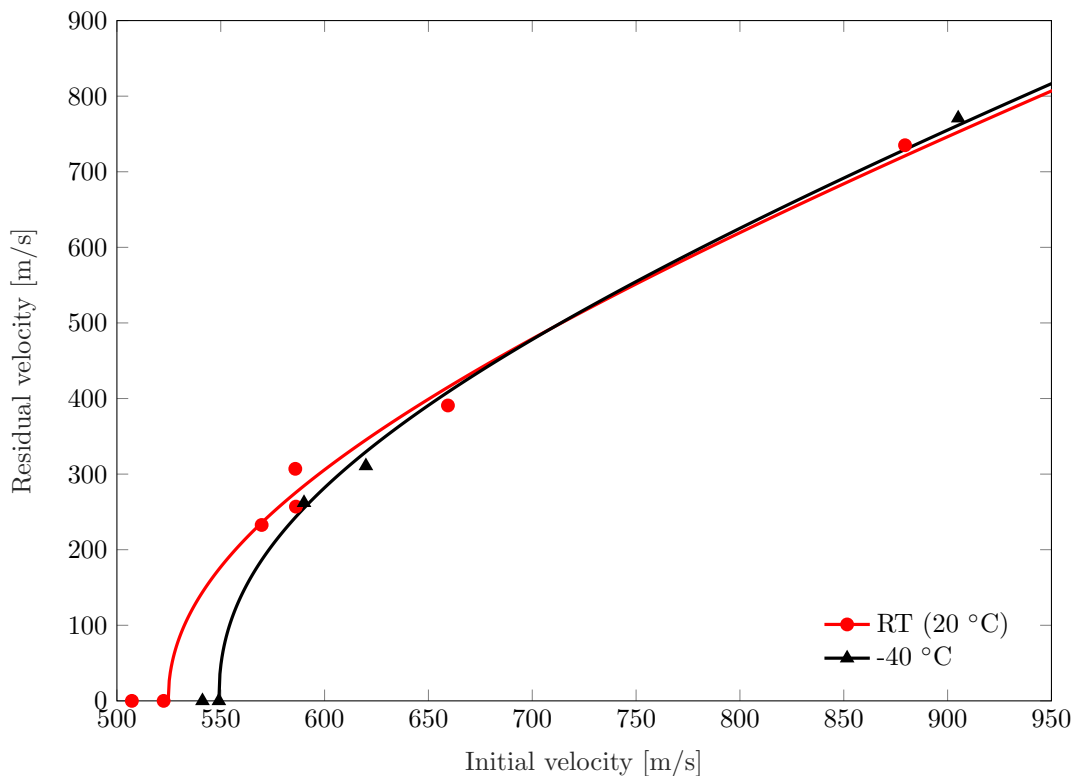
**Table 4.4:** Tabulated results - Armox 500T 2x3.5 mm plates at -40 °C .

Test	Gunpowder [grain]	$v_i$ [m/s]	$v_r$ [m/s]	Comment
1	Full	905.1	770.9	OK
2	31.0	541.2	0.0	No exit
3	32.0	549.1	0.0	No exit
4	34.0	619.9	310.8	Projectile split in two
5	33.0	590.1	262.1	Projectile split in two.

Table 4.5 presents the Recht-Ipson parameters obtained from the experiments at RT and -40 °C. In Figure 4.4 the fitted ballistic limit curves and the experimental data are illustrated.

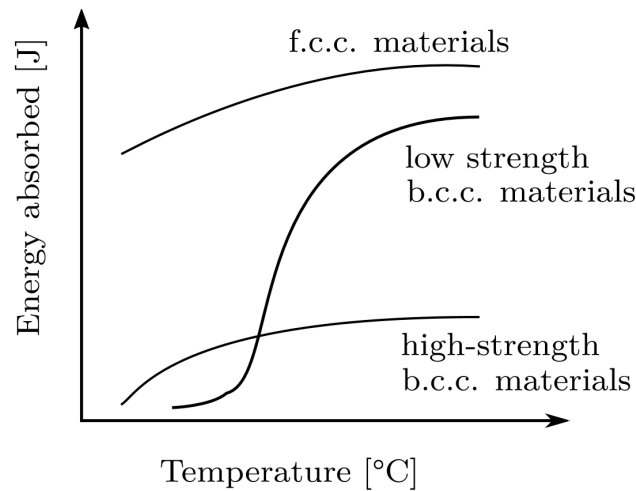
**Table 4.5:** Recht-Ipson parameters - Armox 500T 2x3.5 mm plates.

Parameters	Units	RT	-40 °C
$a$	[-]	1	1
$p$	[-]	2.09	2.26
$v_{bl}$	[m/s]	524.7	549.1



**Figure 4.4:** Ballistic velocity curves and experimental data for each temperature.

The ballistic curves shows that a decrease in temperature gives a slightly higher ballistic limit velocity. An increase of 4.65% was observed for the laminated configuration at  $-40\text{ }^{\circ}\text{C}$  compared to RT. This indicated that the ductile to brittle transition temperature was lower than  $-40\text{ }^{\circ}\text{C}$  for Armox 500T under these conditions. A brittle fracture would require less work, with other words it would absorb less energy, and the residual velocity would increase. Here, the opposite behaviour was detected. Note that a high-strength steel like Armox 500T has a wider temperature transition range than a low-strength steel [19], as shown in Figure 4.5. As mentioned in Section 2.3.2 the probability for brittle fracture increases with high triaxialities, high strain rates and low temperatures. Here, relatively low temperatures and high strain rates were present, but it should be noted that the triaxiality for the perforation process was around zero. The reason for the increase of the ballistic limit velocity is that the yield stress increase with a decreasing temperature [12].



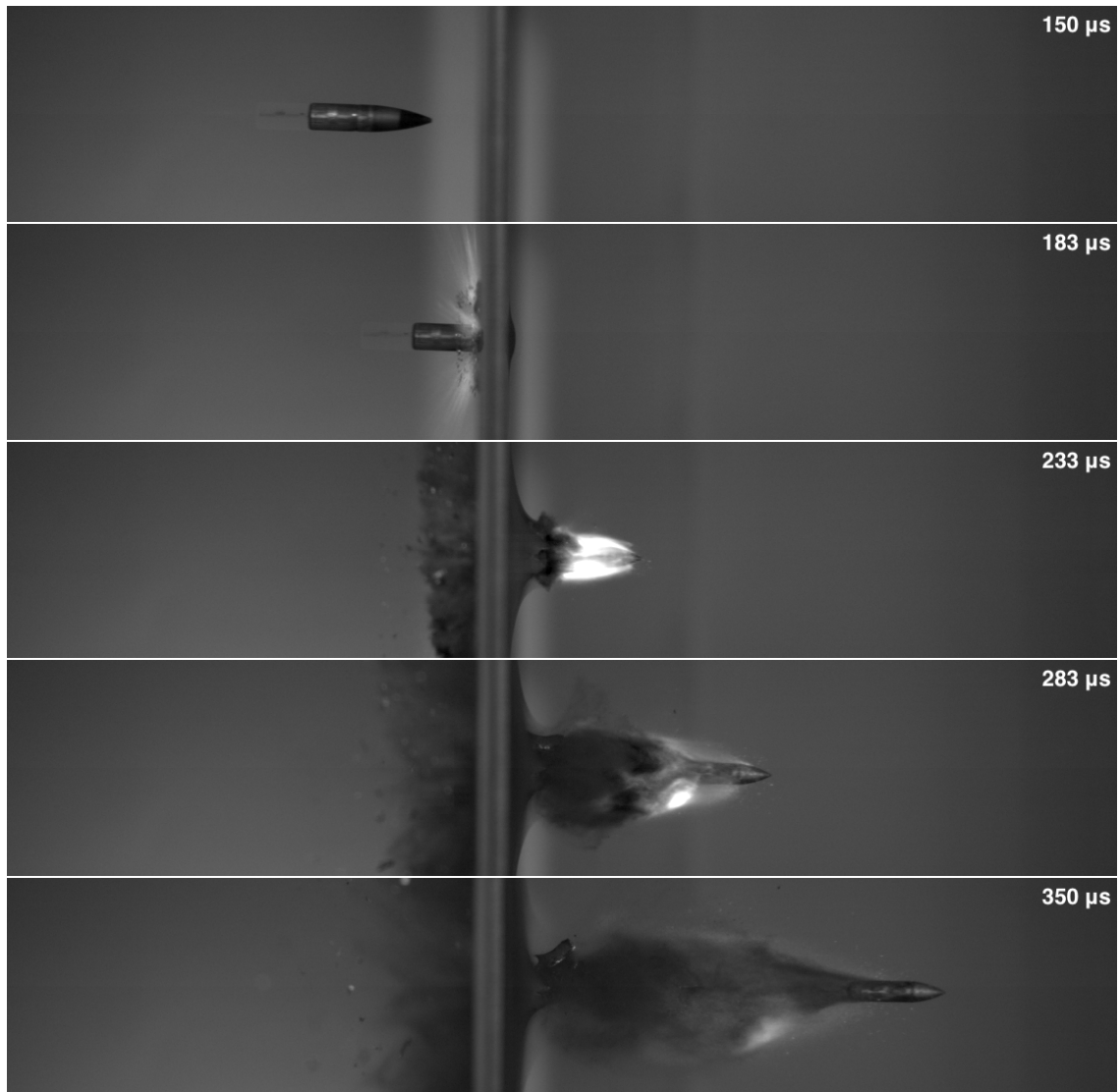
**Figure 4.5:** Theoretical curve for DBTT for different materials [19].

Figure 4.6-4.9 presents time-lapses and appertaining front and back holes for different initial velocities at various temperatures. A summary of observations for each perforation process is given below. Figure 4.6 presents the results for a test with  $v_i = 879.5\text{ m/s}$  at RT. The main failure mode seemed to be ductile hole growth. However, Figure 4.6b and 4.6c shows some fragmentation, this is due to the relatively high yield stress and low fracture strain of Armox 500T. For an impact with  $v_i = 905.1\text{ m/s}$  at  $-40\text{ }^{\circ}\text{C}$  almost exactly the same behaviour was seen as shown in Figure 4.7. Ductile hole growth was still the main fracture mode for impacts with velocities near the ballistic limit velocity, but Figure 4.8c and 4.9c shows that petals were formed around the exit holes. Less fragmentation was observed at both temperatures.

Note, in Figure 4.9 the projectile split in at least two pieces and that the back end remained in the plate.

The results indicated that a decrease in temperature has a small positive effect on the ballistic limit velocity, but it does not largely affect the failure modes. Also, the results showed that the failure modes were more sensitivity to different initial velocities than temperature inside the tested range. In Chapter 6 a numerical study was conducted at low temperatures to further investigate the effect.

Another observation from the time-lapses was that some of the projectiles seemed to impact the plate with an angle, as clearly seen in Figure 4.7. As mentioned in Section 2.1.1, the impact angle is defined as the angle between the target normal and the axis of symmetry of the projectile. Here, the target normal and the velocity vector was assumed to be parallel. It is shown by Goldsmith et al. [22] that the impact angle affects the residual velocity. In Chapter 6 a numerical study conducted to see if the residual velocity is sensitive for angles up to  $10^\circ$  is presented.



(a) Time-lapse.

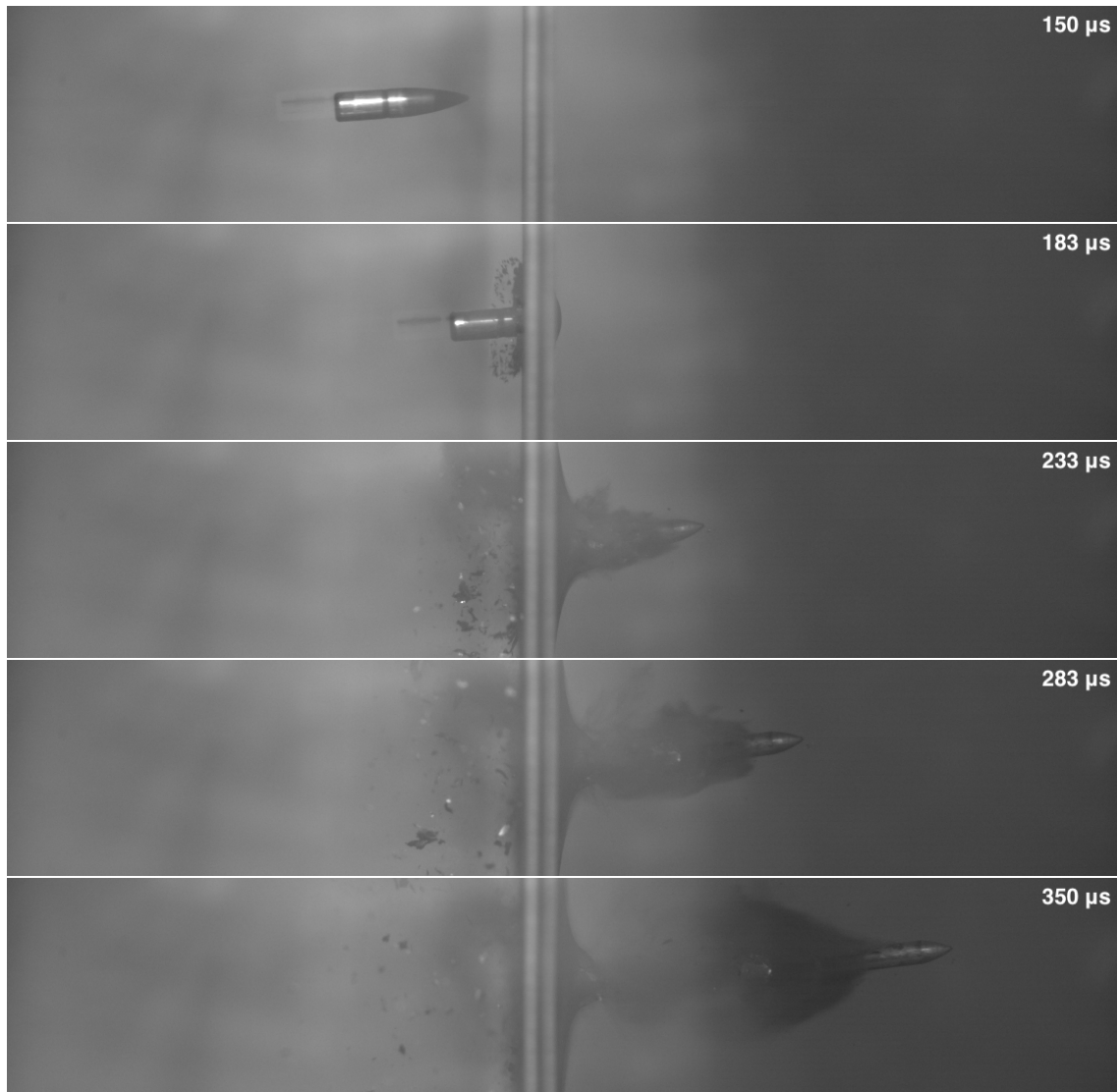


(b) Front hole.

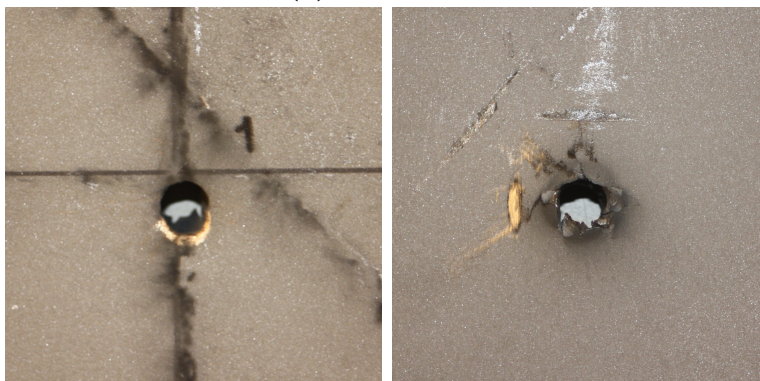
(c) Back hole.

**Figure 4.6:** Test 1 at RT.  $v_i = 879.5$  m/s and  $v_r = 735.1$  m/s.





(a) Time-lapse.

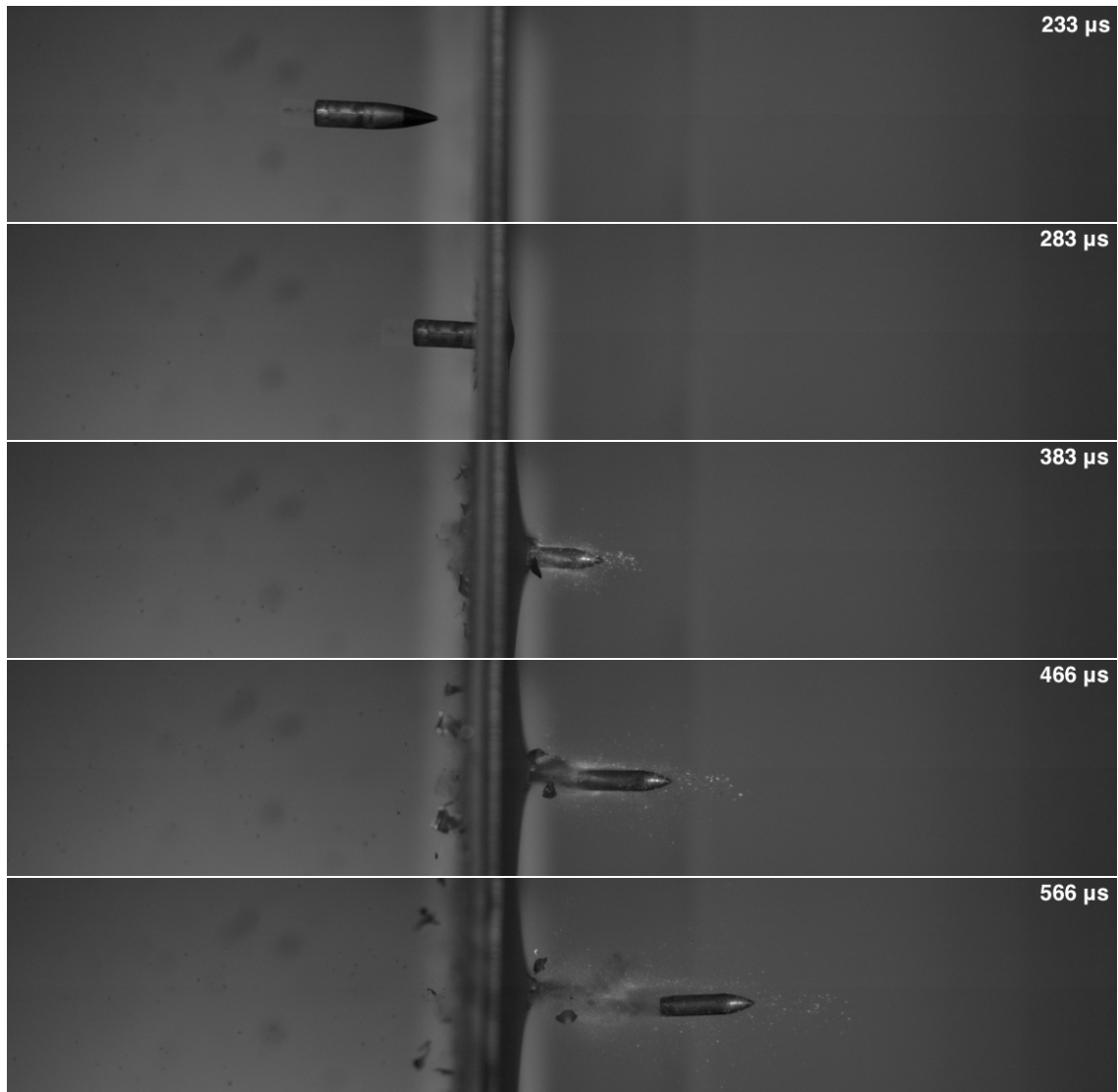


(b) Front hole.

(c) Back hole.

**Figure 4.7:** Test 1 at  $-40\text{ }^{\circ}\text{C}$ .  $v_i = 905.1\text{ m/s}$  and  $v_r = 770.9\text{ m/s}$ .





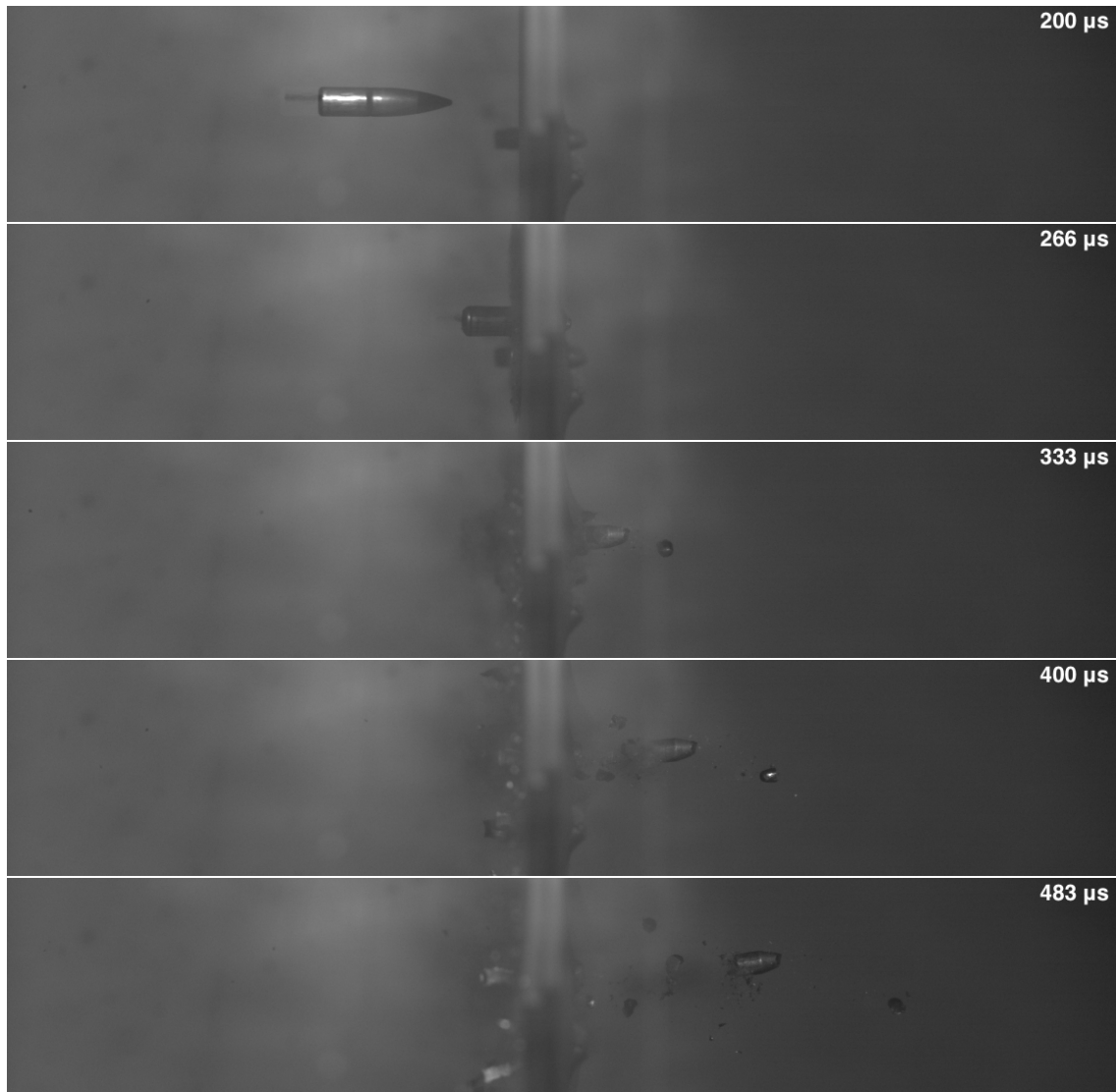
(a) Time-lapse.



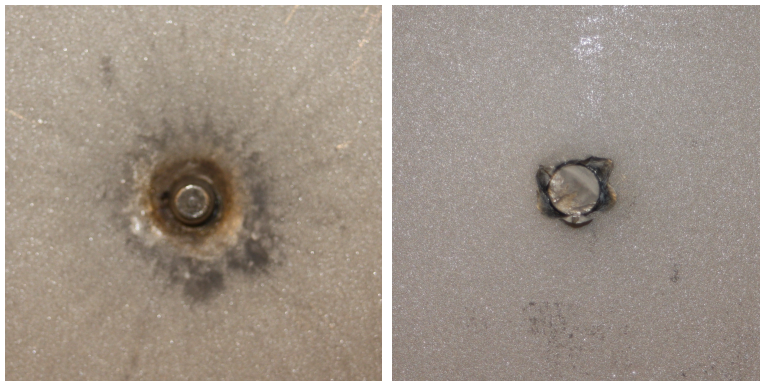
(b) Front hole.

(c) Back hole.

**Figure 4.8:** Test 3 at RT.  $v_i = 569.7$  m/s and  $v_r = 232.7$  m/s.



(a) Time-lapse.



(b) Front hole.

(c) Back hole.

**Figure 4.9:** Test 5 at  $-40\text{ }^{\circ}\text{C}$ .  $v_i = 590.1\text{ m/s}$  and  $v_r = 262.1\text{ m/s}$ .

### 4.2.2 NVE 36 Steel

Table 4.6 and 4.7 presents the results at RT and -40 °C. All tests were successful, except of test number 2 at -40 °C.

**Table 4.6:** Tabulated results - NVE 36 6 mm plates at RT.

Test	Gunpowder [grain]	$v_i$ [m/s]	$v_r$ [m/s]	Comment
1	Full	916.5	863.3	OK
2	39.0	698.2	608.3	OK
3	30.0	512.6	335.1	OK
4	28.0	493.6	311.2	OK
5	26.0	459.7	227.3	OK
6	24.0	409.8	105.3	OK
7	23.0	395.5	0.0	No exit
8	35.0	608.3	493.0	OK

**Table 4.7:** Tabulated results - NVE 36 6 mm plates at -40 °C.

Test	Gunpowder [grain]	$v_i$ [m/s]	$v_r$ [m/s]	Comment
1	Full	914.9	862.1	OK
2	30.0	-	-	No measurment
3	28.0	510.0	278.5	OK
4	25.0	416.5	0.0	No exit
5	26.0	439.8	149.6	OK

The Recht-Ipson parameters obtained from the experiments are listed in Table 4.8. Figure 4.10 presents the experimental data and the ballistic limit curves.

**Table 4.8:** Recht-Ipson parameters - NVE 36 6 mm plates.

Parameters	Units	RT	-40 °C
$a$	[-]	1	1
$p$	[-]	2.22	2.17
$v_{bl}$	[m/s]	401.9	419.4

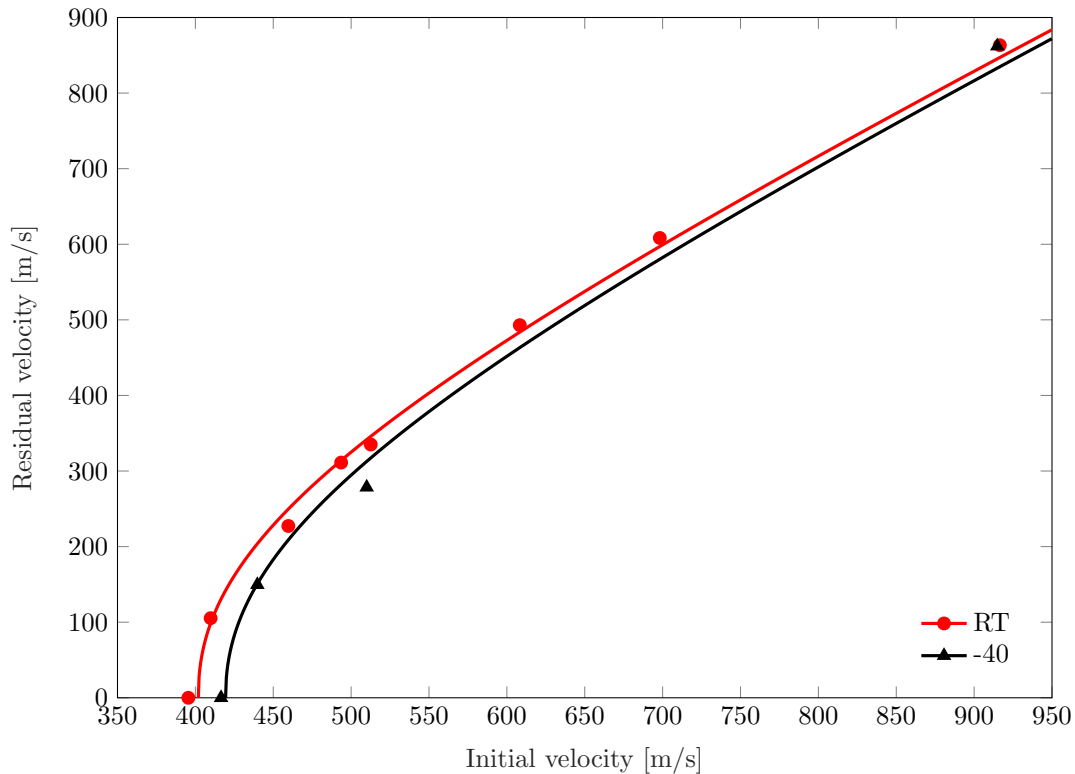
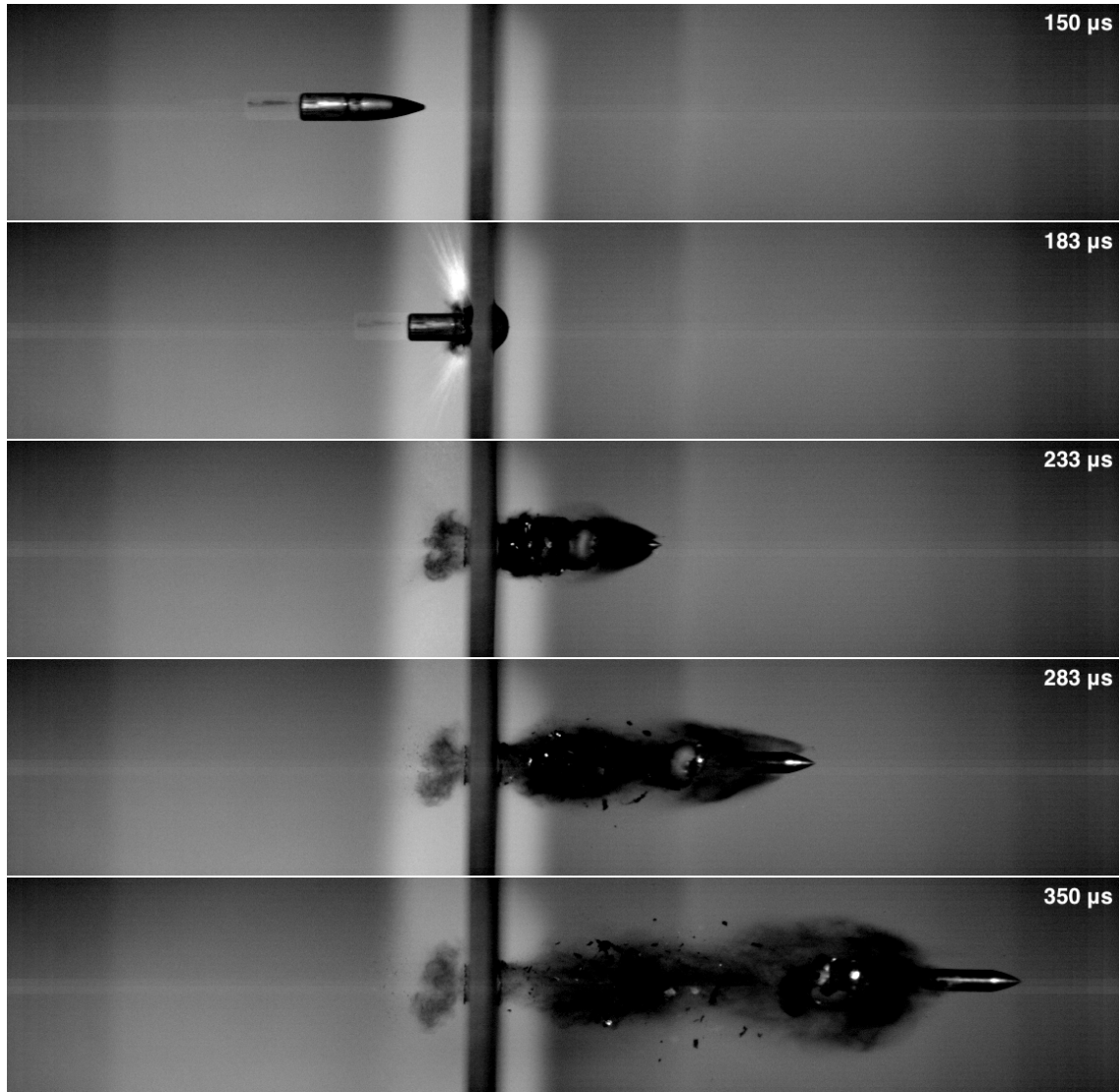


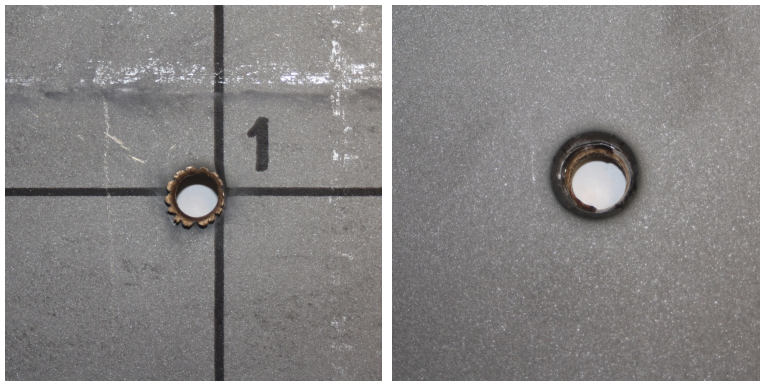
**Figure 4.10:** Ballistic velocity curves and experimental data for each temperature.

The same tendencies for the ballistic limit velocity and failure modes were seen for NVE 36 as for Armox 500T. Here, an increase of 4.35% was observed for the monolithic configuration at  $-40\text{ }^{\circ}\text{C}$  compared to RT. In Figure 4.11-4.14 time-lapses and appertaining front and back holes for different initial velocities at various temperatures are presented. The plate in Figure 4.11a failed with ductile hole growth. No fragmentation was seen. It was observed that the exit hole was slightly bigger than the projectile. Notice in Figure 4.11b that parts of the brass jacket stop during perforation. Figure 4.12a shows an impact with  $v_i = 914.9\text{ m/s}$  at  $-40\text{ }^{\circ}\text{C}$ . No differences in failure modes were seen between the two impacts. Figure 4.13 and 4.14 show perforations with impact velocities just above the ballistic limit velocity. Ductile hole growth was still the main fracture mode, but Figure 4.13c indicates radial cracks. Note, in Figure 4.14 the end cap stops in the target plate, while the bullet perforates the plate.





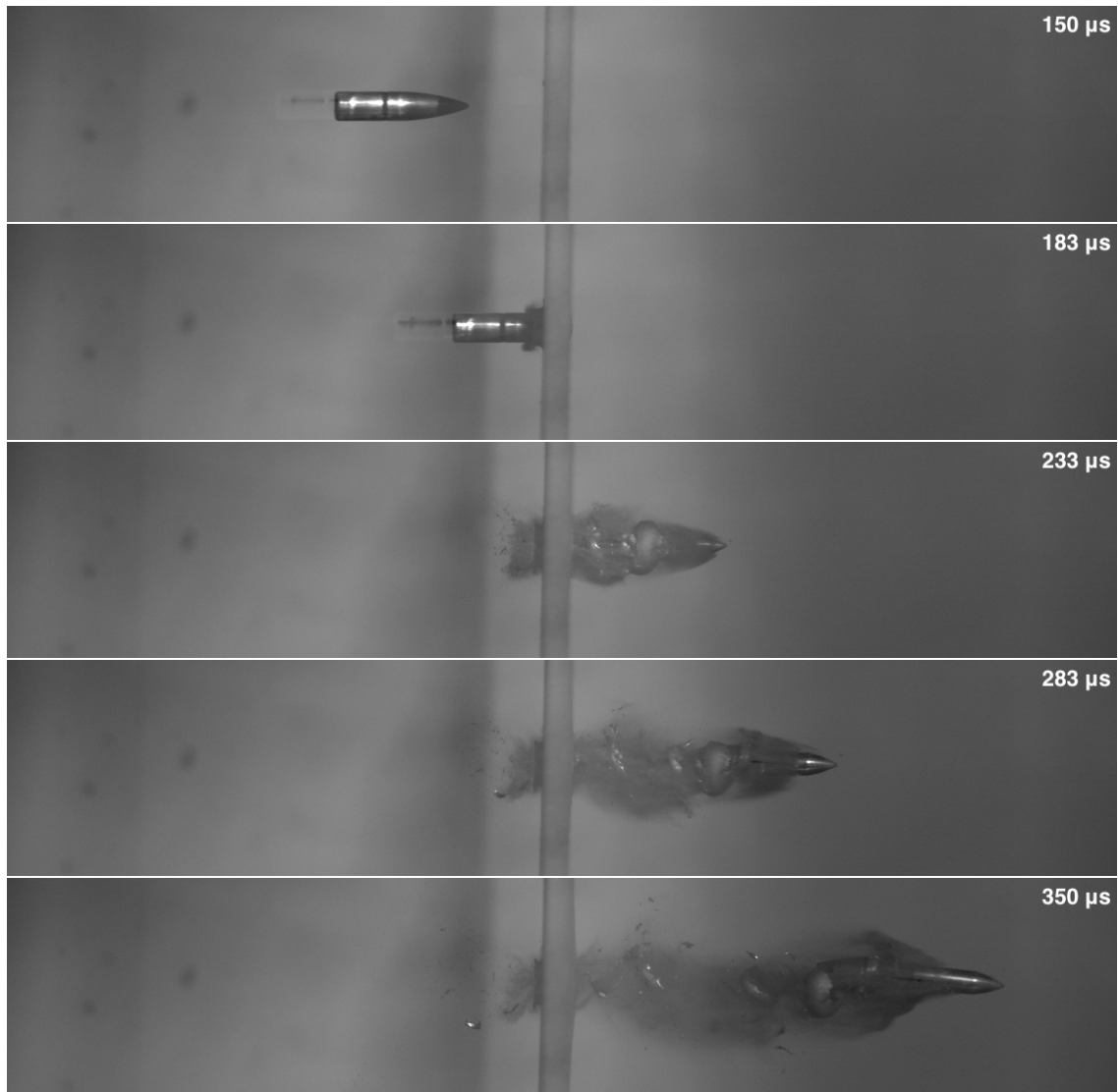
(a) Time-lapse.



(b) Front hole.

(c) Back hole.

**Figure 4.11:** Test 1 at RT.  $v_i = 916.5$  m/s and  $v_r = 863.3$  m/s.



(a) Time-lapse.

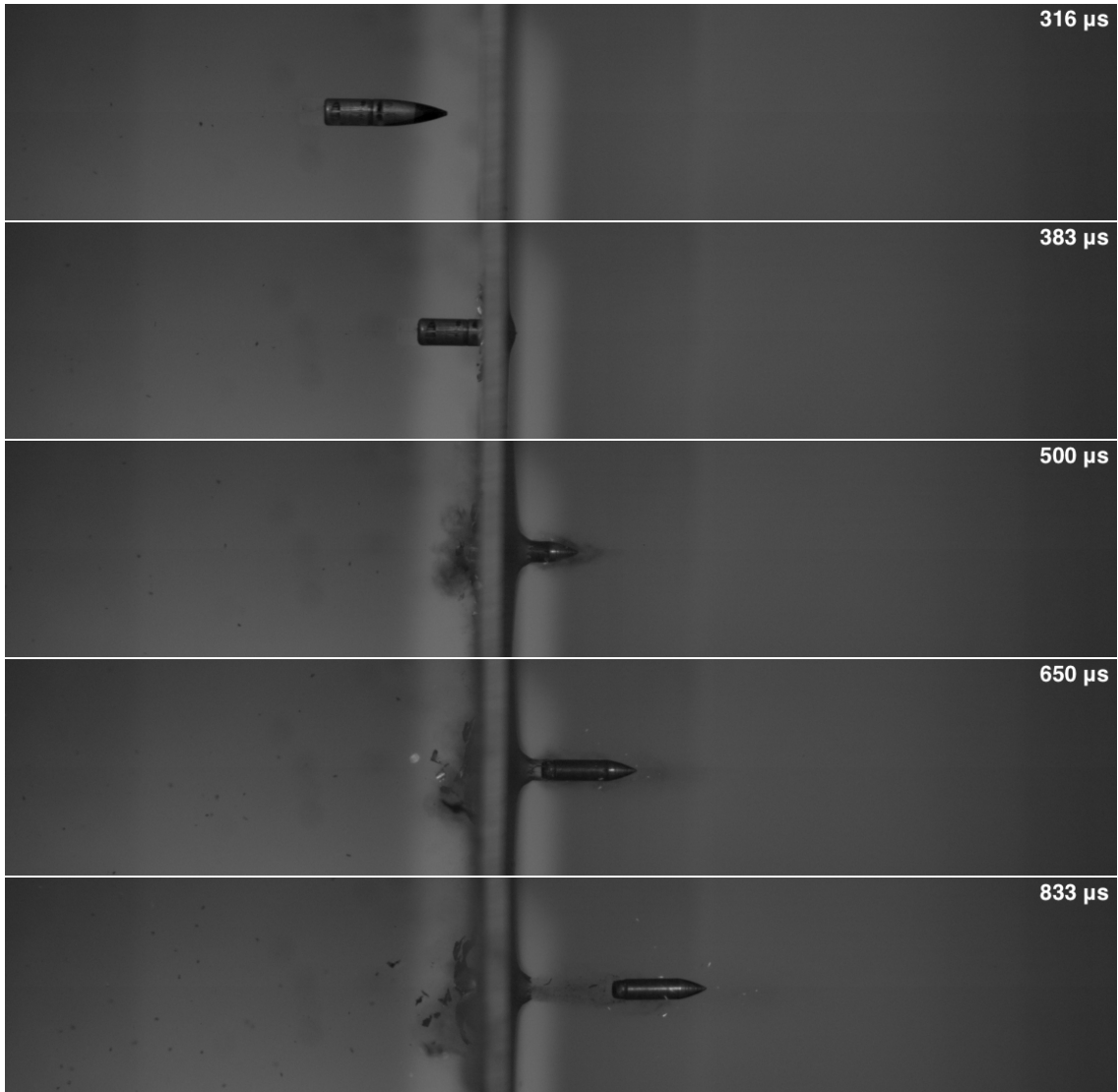


(b) Front hole.

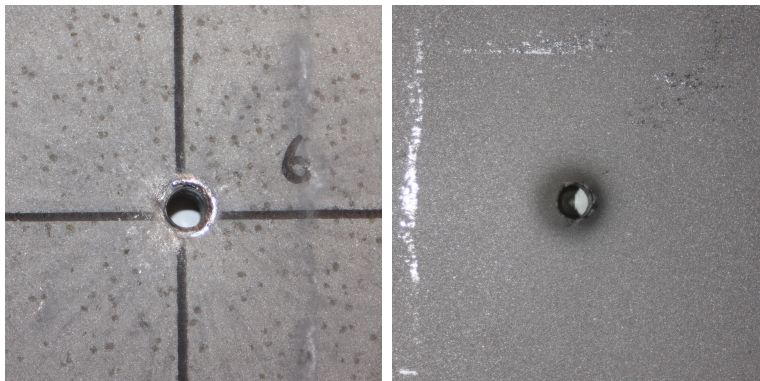


(c) Back hole.

**Figure 4.12:** Test 1 at  $-40\text{ }^{\circ}\text{C}$ .  $v_i = 914.9\text{ m/s}$  and  $v_r = 862.1\text{ m/s}$ .



(a) Time-lapse.



(b) Front hole.

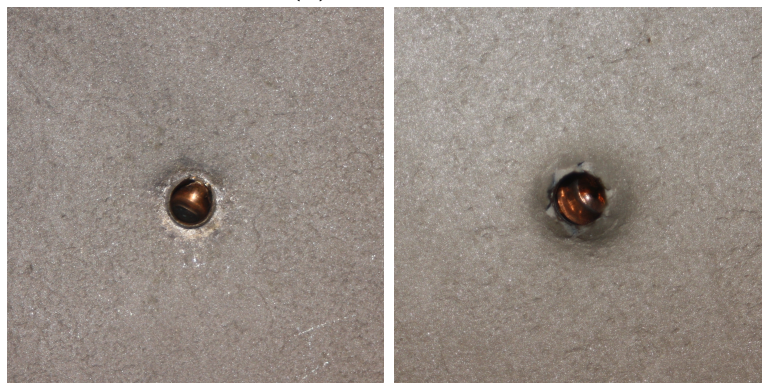
(c) Back hole.

**Figure 4.13:** Test 6 at RT.  $v_i = 409.8$  m/s and  $v_r = 105.3$  m/s.





(a) Time-lapse.



(b) Front hole.

(c) Back hole.

**Figure 4.14:** Test 5 at  $-40\text{ }^{\circ}\text{C}$ .  $v_i = 439.8\text{ m/s}$  and  $v_r = 149.6\text{ m/s}$ .



### 4.3 Summary and Discussion

Table 4.9 presents a summary of ballistic limit velocities and failure modes for both Armox 500T and NVE 36. Following notations are used; Ductile Hole Growth (DHG), Fragmentation (F), Petaling (P) and Radial Cracks (RC).

**Table 4.9:** Summary: Ballistic limit velocities and failure modes.

Material	Temperature	$v_{bl}$ [m/s]	Rel. diff.	Failure modes
Armox 500T	RT (20 °C)	524.7	-	DHG, F <sup>2</sup> , P <sup>1</sup>
Armox 500T	-40 °C	549.1	+4.65%	DHG, F <sup>2</sup> , P <sup>1</sup>
NVE 36	RT (20 °C)	401.9	-	DHG, RC <sup>1</sup>
NVE 36	-40 °C	419.4	+4.35%	DHG, RC <sup>1</sup>

<sup>1</sup> for low impact velocities.

<sup>2</sup> for high impact velocities.

- A decrease in temperature gives a decrease of the residual velocity for both materials, especially for velocities near the ballistic limit velocity. The increase of the ballistic limit velocity was shown to be around 4% for both materials. The ballistic limit curves converge to each other for high initial velocities.
- The DBTT seemed to be below -40 °C for both materials, due to approximately no change in failure modes for the different temperatures. The results indicated that the failure modes were more sensitive to initial velocities than to temperatures.

Note that these observations are based on 13 shots for each material.



## Calibration of Material Models

To describe the material behaviour in a numerical simulation a material model needs to be calibrated. In this chapter the calibration process will be described. Based on the true stress - logarithmic strain curves obtained in Chapter 3 the Modified Johnson-Cook material models will be calibrated using both Voce and Power hardening rules (Equation 2.13 and 2.12). In addition, calibration of the Cockcroft-Latham fracture parameter,  $W_C$ , will be presented. Two different approaches were used; (i) direct calibration and (ii) inverse modeling.

- (i) The material parameters for both Voce and Power hardening rules were curve fitted to the experimental data by using the least squares method. The two term Voce hardening rule, as defined in Equation 2.13, was used for both materials. It was not able to capture the yield plateau for NVE 36, seen in Figure 5.7b, but gives a good enough estimate [23][33].
- (ii) To verify the results from the direct calibration, two numerical models were established in IMPETUS Afea Solver [28]. Small differences were seen in the response between the experiments and the initial numerical simulations. The reasons for this will be discussed later in this chapter. By tuning the material parameters a good curve fit was obtained. Here, only Voce hardening rule was applied to save computational time.

Only small variations in material response for specimens of the same material was observed in Chapter 3. Therefore, only results from one material test was used to calibrate each material model. The tests with the highest fracture strain were chosen [23]. How this affected the results with regards to fracture for the component model is investigated and discussed in Chapter 6. For Armox 500T results from Test 2,  $90^\circ$  was used, and for NVE 36 results from Test 1,  $90^\circ$  was used.

Note, the strain rate hardening parameter,  $C$ , and temperature softening parameter,  $m$ , for both materials were found in the literature. Because only quasi-static tensile tests were conducted. A summary of the material data can be found in Section 5.3.

## 5.1 Armox 500T Steel

### 5.1.1 Direct Calibration of Material Model

#### The Modified Johnson-Cook Material Model

As mentioned in Section 3.1.3 the stress - strain relation is only valid up to diffuse necking. Therefore, the Voce and Power hardening rules were calibrated with data up to necking, as shown in Figure 5.1a and 5.2a. To ensure that necking occurs at the right amount of strain, the constraint

$$\frac{d\sigma_t}{d\varepsilon_t} = \sigma_t \quad (5.1)$$

was included in the curve fitting algorithm. The black x in Figure 5.1b and 5.2b marks when necking occurred for the test specimens. The Voce hardening rule seemed to predict necking satisfactory. The Power hardening rule was not able to recreate the curve and necking with only one polynomial term. This can be seen in Figure 5.2. Voce hardening rule was therefore preferred in the rest of this thesis. After necking the material behaviour was extrapolated as illustrated with the red dotted line in Figure 5.1b and 5.2b. Table 5.1 and 5.2 present the results from the direct calibration.

**Table 5.1:** Direct calibration with Power hardening rule.

$A$ [MPa]	$B$ [MPa]	$n$ [-]
972.8	1161.8	0.2

**Table 5.2:** Direct calibration with Voce hardening rule.

$\sigma_0$ [MPa]	$Q_{R1}$ [MPa]	$C_{R1}$ [-]	$Q_{R2}$ [MPa]	$C_{R2}$ [-]
1239.9	123	654.8	250.1	109.9

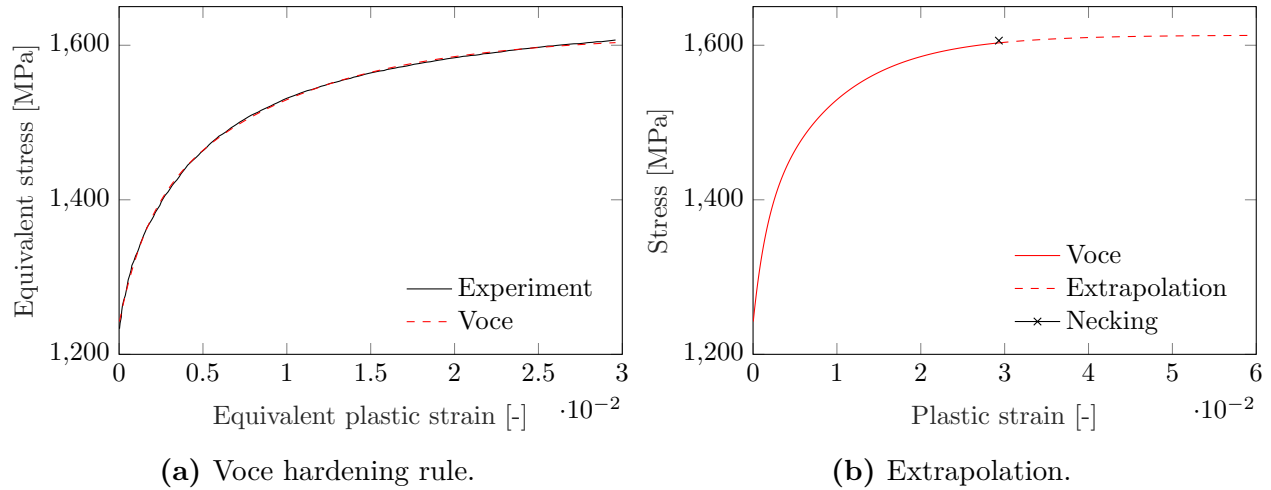


**Figure 5.1:** Stress - strain curves until necking for the Voce hardening rule.

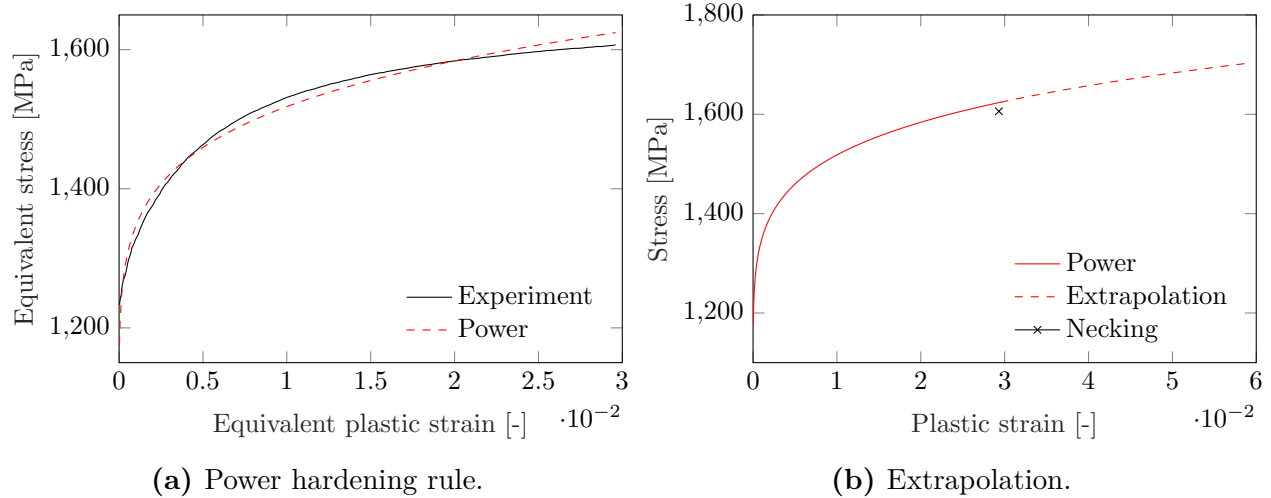


**Figure 5.2:** Stress - strain curves until necking for the Power hardening rule.

High-strength steels like Armox 500T are shown to be almost insensitive to strain rates and temperature [12]. The strain rate hardening,  $C$ , and the temperature softening,  $m$ , parameter was therefore assumed to be equal to the parameters of Armox 560T found from Børvik et al. [9].

**Table 5.3:** Strain rate hardening and temperature softening parameters.

$C$ [-]	$m$ [-]
0.0010	1

### 5.1.2 Inverse Modelling

To save computational time only a half of the dog bone specimen was built due to symmetry about the z-axis and it was established without the holes. In addition, different mesh sizes were given to different parts. Figure 5.3 illustrates the numerical model. The model consists of four parts; (i) fixed left part, (ii) gauge area, (iii) localization area and (iv) moving right part. A summary over elements and mesh sizes are given below.

- (i) Rigid material meshed with 64-node hexahedron cubic elements.
- (ii) 64-node hexahedron cubic elements with a mesh size of  $2 \times 2 \times 1.75 \text{ mm}^3$ .
- (iii) 64-node hexahedron cubic elements with a mesh size of  $0.5 \times 0.5 \times 0.5 \text{ mm}^3$ .
- (iv) Rigid material meshed with 64-node hexahedron cubic elements.

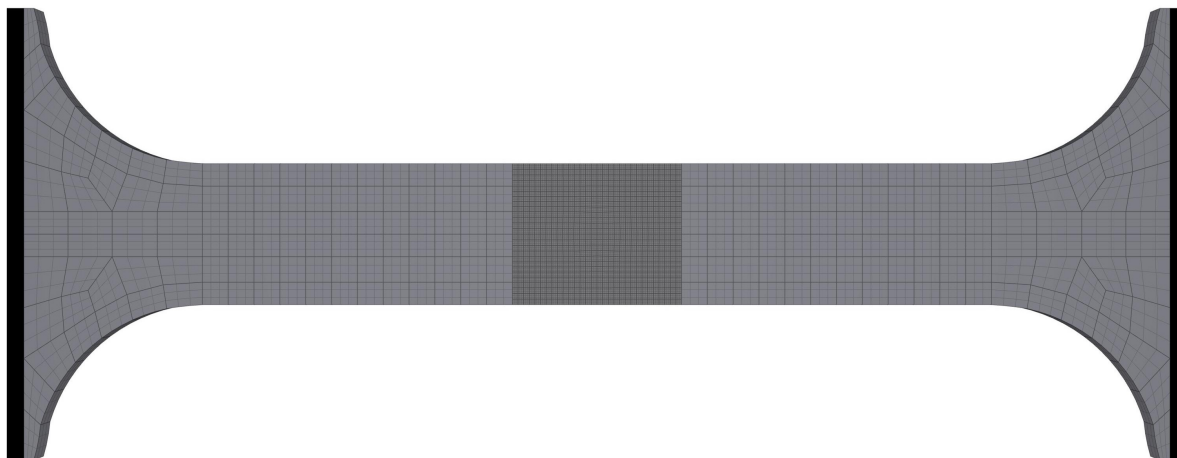


**Figure 5.3:** Meshed dog bone specimen.

As in the experimental tensile tests, the left side was fixed in the length direction. The right end was free to move and loading was applied with a given displacement of 10 mm. For an explicit numerical solver as IMPETUS small time steps are needed to avoid an unstable response [31]. The critical time step is given by

$$\Delta t_{cr} = \frac{L_e}{c_d}, \quad c_d = \sqrt{\frac{E}{\rho}} \quad (5.2)$$

where  $L_e$  is the element length,  $c_d$  is the speed of sound in the material,  $E$  is Young's modulus and  $\rho$  is the material density. Time scaling was applied, since the real time of the

experiments were too long for an explicit solver. The right end was given a displacement rate of 250 mm/s. Here, the energy balance was examined to be sure that undesirable inertia effects were avoided.

### The Modified Johnson-Cook Material Model

No fracture criteria was defined in this section, to verify the hardening parameters obtained from the direct calibration. Figure 5.4a presents the relation obtained from the first simulation with parameters obtained from the direct calibration. The curves diverges after a given displacement of 2 mm. This indicates that the extrapolation from Section 5.1.1 does not predict the correct material behaviour. By tuning the material constants the curve in Figure 5.4b was obtained. Table 5.4 presents the tuned constants.

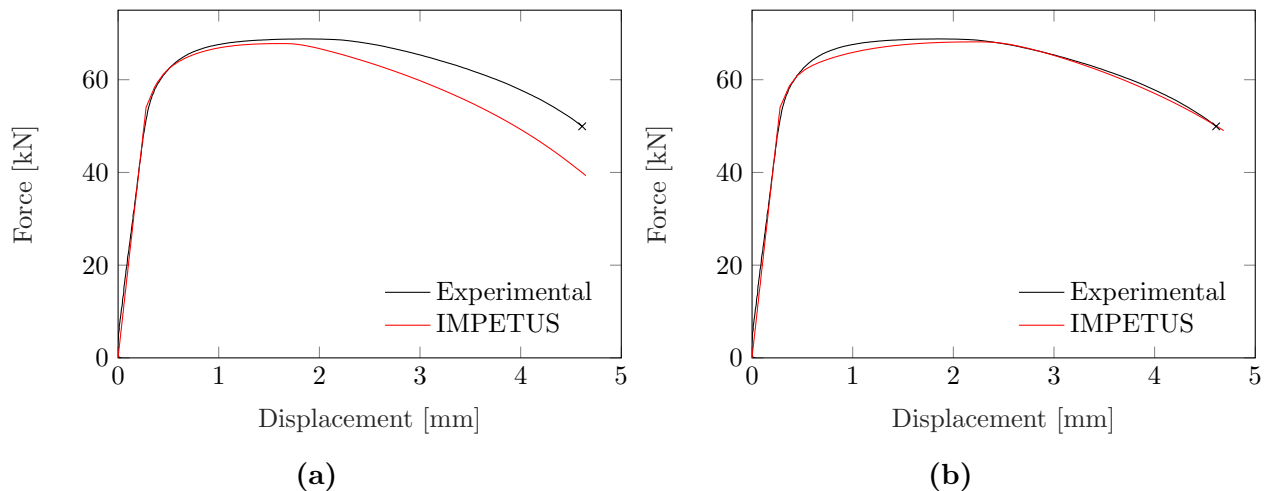


**Figure 5.4:** Force - displacement curve from the experiment compared to IMPETUS simulations with; (a) Material parameters from direct calibration and (b) tuned material parameters. The black x marks fracture for the experiment.

**Table 5.4:** Voce parameters from inverse modelling.

$\sigma_0$ [MPa]	$Q_{R1}$ [MPa]	$C_{R1}$ [-]	$Q_{R2}$ [MPa]	$C_{R2}$ [-]
1239.9	140	654.8	275.1	60

An alternative method to the trial and error method used in this section, is a numerical optimization tool named LS-OPT. It interacts with the finite element program LS-DYNA. Here, several simulations are run in a sequential order with different material parameters until the wanted response is obtained. The material parameters found from the direct calibration are used as initial values. This method requires a lot of computational time, but gives a

good curve fit. However, the trial and error method was preferred since it gave a good feeling about how the different material parameters influence the response and a satisfactory curve fit was obtained [23].

### The Cockcroft-Latham Fracture Criterion

A fracture criterion was then defined to predict fracture in the numerical simulations. In order to calibrate the fracture criterion, the equivalent plastic strain and the maximum principal stress were extracted from the most critical node in the neck. The node is marked with a blue dot in Figure 5.5. Compared with the global response the stress level of the critical node was clearly higher after diffuse necking. The fracture value found from the area under the stress distribution was found to be  $W_C = 2200$  MPa. Using this value the numerical simulation seemed to predict failure accurately (see Figure 5.6). Note, that the fracture parameter,  $W_C$ , is a mesh sensitive parameter. Therefore, the same mesh size was used for the localization area in the numerical tensile tests and for the impact area in the base model in Chapter 6.

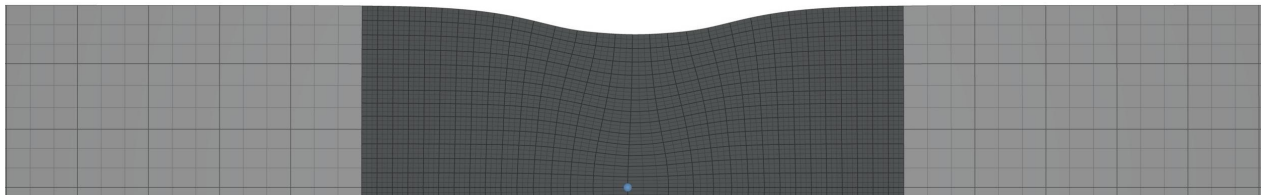


**Figure 5.5:** Critical node in the neck marked with a blue dot.

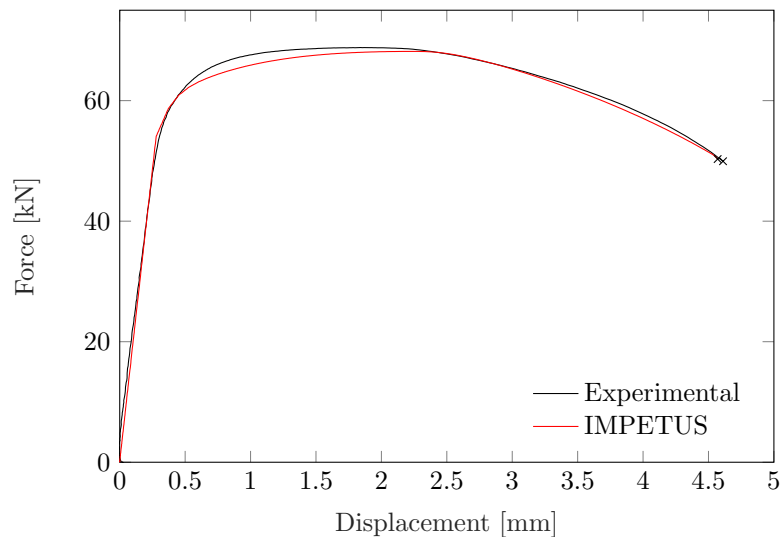


**Figure 5.6:** Force - displacement curve from the experiment compared to IMPETUS simulations with  $W_C$  from inverse modelling.



## 5.2 NVE 36 Steel

Almost the exact methods were used to calibrate the material model for NVE 36 as for Armox 500T described in the previous section. Some differences were seen and are described in the this section. These differences are caused by different initial geometry of the tensile specimens.

### 5.2.1 Direct Calibration of Material Model

#### The Modified Johnson-Cook Material Model

For the circular specimens no extrapolation of the stress - strain relation was needed, since local measurements of the necking area was performed. This gave valid data up to fracture. Figure 5.7a shows where necking occurred with the crossing point of the two curves. After necking the true stress differs from the equivalent stress due to a triaxial stress state in the neck. As mentioned in Section 2.2.1, the Bridgman correction gives an approximation of the equivalent stress after necking. Figure 5.7b presents the equivalent stress curve found by Bridgman correction and the curve fitted Voce hardening rule. Table 5.5 lists the MJC material constants.

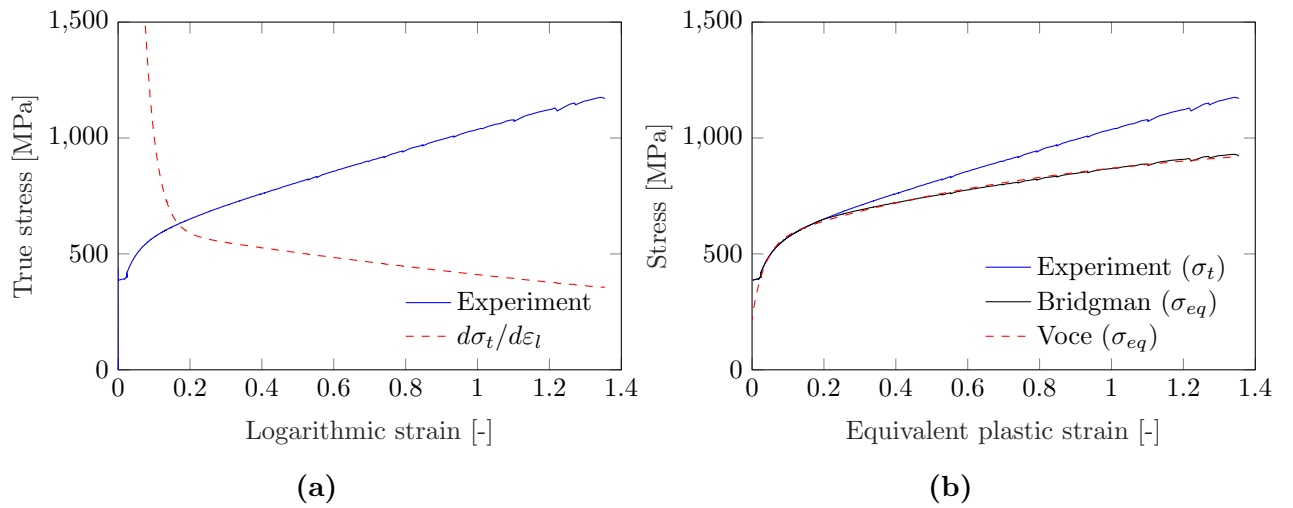


**Figure 5.7:** (a) The cross point defined necking and (b) shows the Bridgman correction.

**Table 5.5:** Direct calibration with Voce hardening rule.

$\sigma_0$ [MPa]	$Q_{R1}$ [MPa]	$C_{R1}$ [-]	$Q_{R2}$ [MPa]	$C_{R2}$ [-]
224.7	320.9	28.7	476.7	1.1368

The strain rate hardening,  $C$ , and the temperature softening,  $m$ , were assumed equal to the parameters used in Børvik et al. [10] for Weldox 460E. To validate this assumption a numerical study was conducted and is presented in Chapter 6.

**Table 5.6:** Strain rate hardening and temperature softening parameters.

$C$ [-]	$m$ [-]
0.0114	0.94

## 5.2.2 Direct Calibration of Fracture Criterion

### The Cockcroft-Latham Fracture Criterion

The critical fracture value was found to be 1182.5 MPa by numerical integration of the true stress curve in Figure 5.7b. This value was used in the inverse modeling of the fracture criterion.

## 5.2.3 Inverse Modelling

An exact copy of the smooth tensile specimen from Section 3.2.2 was established in IMPETUS Afea Solver. The specimen was built with two different mesh, a coarse mesh ( $1.0 \times 1.0 \times 1.0 \text{ mm}^3$ ) and a fine mesh ( $0.5 \times 0.5 \times 0.5 \text{ mm}^3$ ) to check how the mesh size affects the response and fracture. Figure 5.8 illustrates the coarse mesh. Both mesh consist of fully integrated high-order 64-node hexahedrom elements. These elements are shown to be excellent in plasticity [32]. The fixed left part and the moving right part, illustrated with the dark colour, were assumed rigid. The left part was fixed in the length direction and the right part was given a displacement of 16 mm. Time scaling was applied and the specimen was exposed to a displacement rate of 400 mm/s.

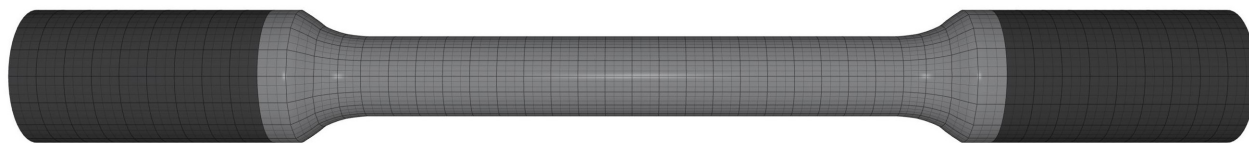


**Figure 5.8:** Meshed smooth specimen.

### The Modified Johnson-Cook Material Model

Several simulations were run without a fracture criterion to verify the direct calibration of the hardening parameters. Figure 5.9a shows the response obtained with values from the

direct calibration. The curves seems to almost coincide and with some small adjustment the responses in Figure 5.9b were obtained. Table 5.7 lists the tuned material parameters for both mesh.

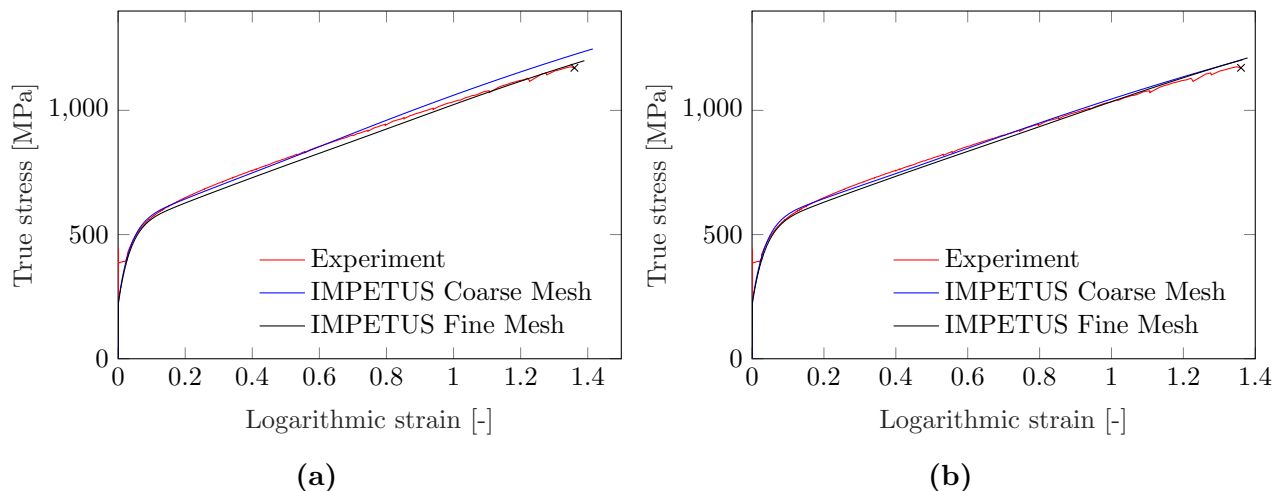


**Figure 5.9:** True stress - logarithmic strain from the experiment compared to IMPETUS simulations for two different mesh with; **(a)** Material parameters from direct calibration and **(b)** tuned material parameters. The black x marks fracture.

**Table 5.7:** Voce parameters from inverse modelling.

Mesh size	$\sigma_0$ [MPa]	$Q_{R1}$ [MPa]	$C_{R1}$ [-]	$Q_{R2}$ [MPa]	$C_{R2}$ [-]
Coarse mesh	224.7	330	28.72	435	1.1368
Fine mesh	224.7	320.9	28.72	495	1.1368

### The Cockcroft-Latham Fracture Criterion

A fracture criterion was then defined. Figure 5.10a shows the relations obtained from simulations with  $W_C = 1182.5$  MPa. The coarse mesh seems to almost predict the right failure strain. It only differs with 2.75%. For the fine mesh the fracture strain was underestimated by 20.9% as expected due to earlier localization and a general higher stress state. To inverse calibrate the  $W_C$  - value the maximum principal stress and the equivalent plastic strain were extracted from the most critical element (see Figure 5.11). Figure 5.10b illustrates the relations with the tuned  $W_C$  parameters. Table 5.8 presents the  $W_C$  - values from the direct and the inverse calibration. These values validates that  $W_C$  is a mesh dependent parameter.

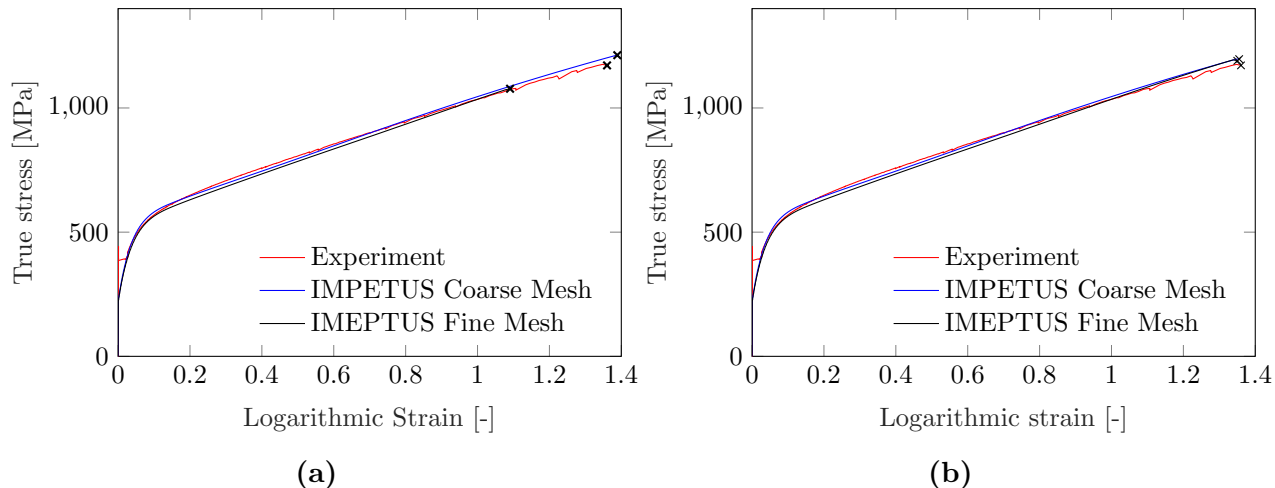


**Figure 5.10:** True stress - logarithmic strain from experiment and IMPETUS simulations with; (a)  $W_C$  from direct calibration and (b)  $W_C$  found by inverse modelling. The black x marks failure.

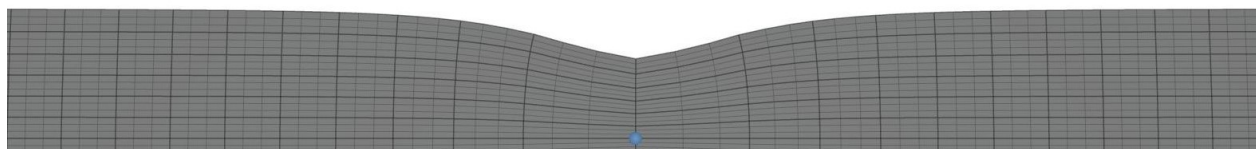


**Figure 5.11:** Critical node in the neck marked with a blue dot.

**Table 5.8:** Calibration of the Cockcroft-Latham Fracture Criterion.

Mesh Size	$W_C$ [MPa]			Percentage
	Experiment	IMPETUS	Deviation	
0.5 x 0.5 x 0.5 mm <sup>3</sup>	1182.5	1430	+247.5	+20.93%
1.0 x 1.0 x 1.0 mm <sup>3</sup>	1182.5	1150	-32.5	-2.75%

## 5.3 Summary of Material Data

A summary of all material parameters found in Chapter 5 are given in Table 5.9. These parameters were used in the numerical component models in Chapter 6.

**Table 5.9:** MJC and CL parameters that will be used in the base models.

	$\sigma_0$ [MPa]	$Q_{R1}$ [MPa]	$C_{R1}$ [-]	$Q_{R2}$ [MPa]	$C_{R2}$ [-]	$C$	$m$	$W_C$
Armox 500T	1239.9	140	654.8	275.1	60	0.0010	1	2200
NVE 36	224.7	320.9	28.7	495	1.14	0.0114	0.94	1430



## Numerical Analysis of the Component Tests

In this chapter two numerical base models will be established in a non-linear explicit solver called IMPETUS Afea Solver [28]. Then, a sensitivity study will be presented. One parameter was altered at a time in order to check the effect of that particular parameter. Lastly, an investigation on effects of temperature will be presented. All simulations were executed using an external computer with specifications listed in Table 6.1.

**Table 6.1:** IMPETUS computer [33].

Component	Description	Quantity
Memory(RAM)	SM Hynix 4 GB DDR3-1866MHz	4
CPU	Intel Xeon E5 quadcore, 3.70 GHz 10 MB cache	1
GPU	Nvidia GPU Tesla Kepler K20C, 5 GB GDDR5 w/2496 cores	2
Motherboard core	PNY Quadro NVS 300 512 MB DDR3	1

Numerical instabilities can occur when non-linear dynamic finite element method (FEM) problems are solved with explicit solvers [31]. Therefore, the total energy balance was checked for all simulations to ensure that no spurious energy was generated. It should not deviate more than 5% [12]. Note, only the energy balance for the base models were plotted.

## 6.1 Armox 500T Steel

### 6.1.1 Base Model

The base model consisted of two parts; the APM2 7.62 mm bullet and the laminated target plate (2 x 3.5 mm). Due to symmetry only half of the projectile and plate were modeled.

#### 7.62 mm APM2 Bullet

The projectile was modeled using the same initial geometry as the APM2 7.62 mm bullet used in the component tests (see Figure 4.3 for nominal values). Each material in the projectile was modeled with the MJC constitutive relation and the Cockcroft-Latham fracture criterion using constants taken from Børvik et al. [9]. Here, the Power hardening rule was used to describe the material strain hardening. Table 6.2 presents the material input. Note that the steel core was assumed to be rigid due to negligible visible deformation under the ballistic experiments. For physical material constants see Table 4.2. The mesh consisted of fully integrated 64-node cubic elements and is shown in Figure 6.1.

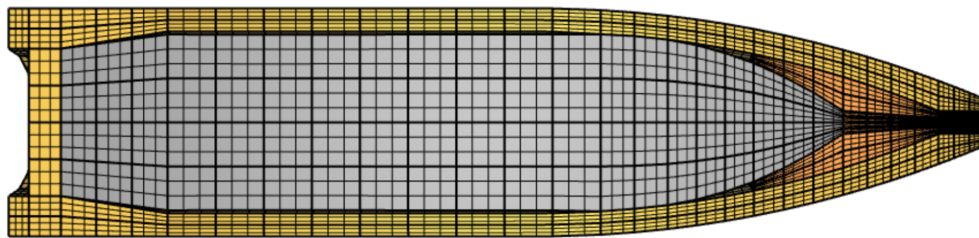


**Figure 6.1:** Meshed APM2 7.62 mm bullet. Provided by Holmen [23].

**Table 6.2:** MJC constitutive relation and CL fracture criterion constants for the APM2 7.62 mm bullet [9].

Material	$A$ [MPa]	$B$ [MPa]	$n$	$\dot{p}_0$ [ $s^{-1}$ ]	$C$	$T_r$ [K]	$T_m$ [K]	$m$	$W_C$ [MPa]
Steel core	1200	50000	1.0	$5 \times 10^{-4}$	0	293	1800	1.0	N/A
Lead cap	24	300	1.0	$5 \times 10^{-4}$	0.1	293	760	1.0	175
Brass jacket	206	505	0.42	$5 \times 10^{-4}$	0.01	293	1189	1.68	914



## Target Plate

For Armox 500T a laminated configuration (2 x 3.5 mm) was established and is shown in Figure 6.2. To save computational time only an 80 mm x 80 mm plate was modeled [25][26]. Holmen et al. [24] showed that the effects of a smaller plate were negligible due to highly local deformations. Between the two target plates a gap of 0.01 mm was modeled to ensure that no initial contact penetration occurred. The target plates were divided into three regions; (i) outside the impact area, (ii) the transition zone and (iii) inside the impact area. 8-noded linear elements with an element size of  $1 \times 1 \times 1.167 \text{ mm}^3$  were used outside a radius of 13 mm. The mesh in the transition zone was refined to  $0.5 \times 0.5 \times 0.58 \text{ mm}^3$ . Inside a radius of 10 mm the mesh consisted of fully integrated 64-node cubic elements with an element size of  $0.5 \times 0.5 \times 0.58 \text{ mm}^3$ .

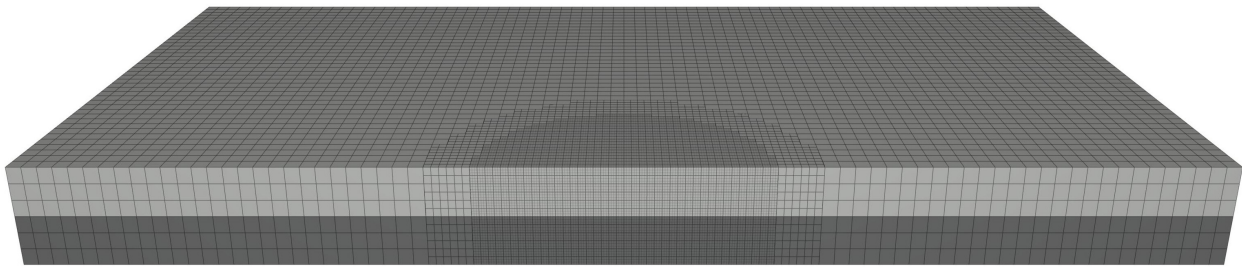


**Figure 6.2:** Meshed laminated Armox 500T configuration (2 x 3.5 mm).

Earlier studies by Holmen and Johnsen [25] and Børvik et al. [11] have shown that the boundary conditions have minor influence on the residual velocity of small-arms bullet impacts in the ordnance velocity regime. Here, one clamped edge was introduced at the back end. A small study was conducted to see if the boundary conditions affected the ballistic limit velocity for a high-strength steel like Armox 500T, and the results are presented later in this chapter. A general penalty contact algorithm in IMPETUS Afea Solver was applied between all the parts. The penalty number was set to  $1 \cdot 10^{15}$  [25]. In addition, the friction constant was set to zero, since conservative results are preferable from a design perspective.

As observed in the results in Chapter 4 the main failure mode under perforation was ductile hole growth. Therefore, the ductile Cockcroft-Latham fracture criterion presented in Section 2.2.3 was applied to the model. Note, node splitting was introduced since it gives a better physical approximation than element erosion [23]. Node splitting also gives the opportunity

to capture fragmentation in the numerical simulations. Furthermore, if a node reach the melting temperature of 1800 K, the element strength drops to zero. Additionally, a linear equation of state (EOS) was applied and is given by

$$p = -K\varepsilon_v + K\alpha_T(T + T_r) \quad (6.1)$$

where  $p$  is the hydrostatic pressure,  $K$  is the bulk modulus,  $\varepsilon_v$  is the volumetric strain,  $T$  the current temperature and  $T_r$  is the reference temperature. For impacts between two solids with an initial velocity between 500 - 2000 m/s, Zukas [37] showed that a non-linear equation of state is of secondary importance.

The material hardening was modeled with the MJC constitutive relation using the Voce hardening rule. In Table 5.9 a summary of the material parameters used in the base model is given. Table 6.3 lists the thermal constants used in the numerical model.

**Table 6.3:** Thermal properties adopted from Børvik et al. [9].

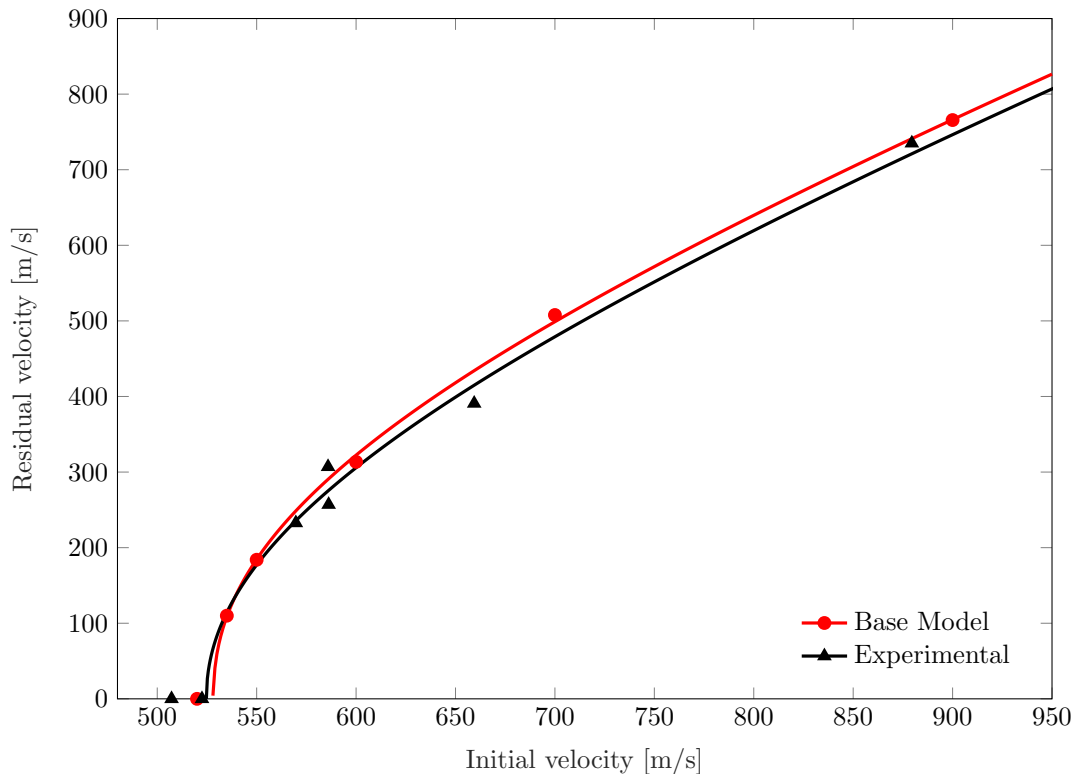
$C_p$ [J/KgK]	$\alpha_T$ [1/K]	$\chi$	$T_{Ref}$ [K]	$T_0$ [K]	$T_m$ [K]
452	1.2E-5	0.9	293	293	1800

## Results

To find the ballistic limit velocity several simulations with different initial velocities were run. Figure 6.3 shows the ballistic limit curves obtained from the base model and the experimental tests. The fitted Recht-Ipson parameters are presented in Table 6.4. Here, the ballistic limit velocity was overestimated with 0.69%. The base model gave a slightly non-conservative result compared to the experimental results.

**Table 6.4:** Recht-Ipson parameters - Armox 500T 2x3.5 mm plates.

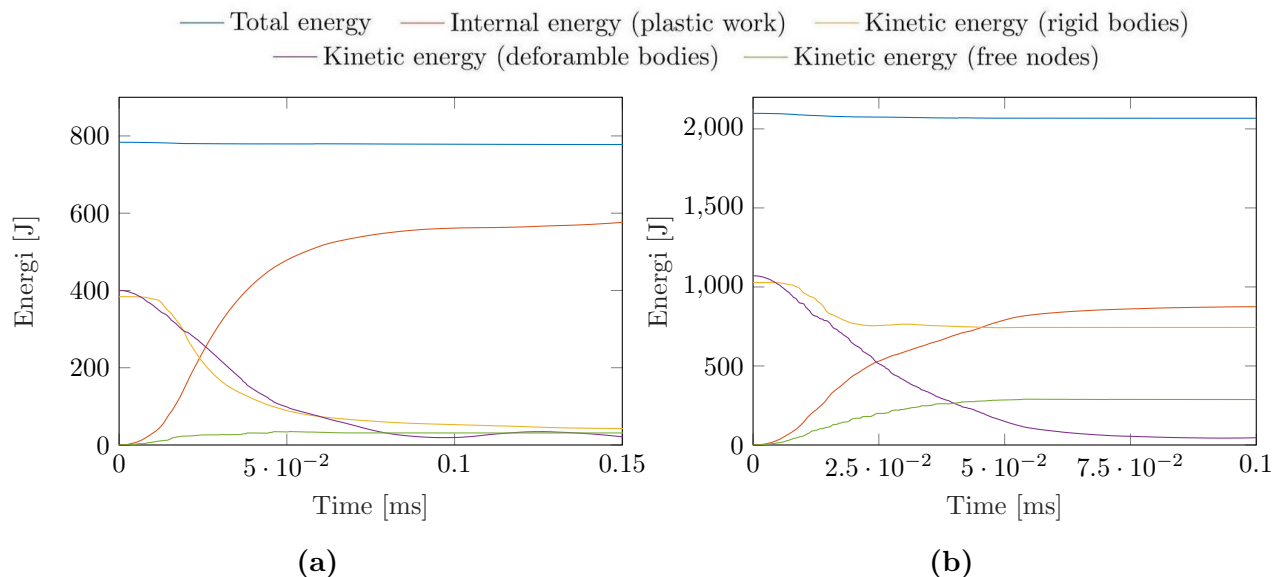
	$a$	$p$	$v_{bl}$ [MPa]	Deviation in $v_{bl}$
Experiment	1	2.09	524.7	-
Base model	1	2.24	528.3	+0.69%



**Figure 6.3:** Ballistic limit curves from experimental data and numerical simulations in IMPETUS.

To compare, two energy balance plots are presented in Figure 6.4. Only a deviation of 0.73% and 1.48% in total energy were observed for the two impact velocities. This is well within the 5% criterion, indicating that the residual velocities obtained by the numerical simulations can be trusted. The kinetic energy from the projectile and the internal plastic energy

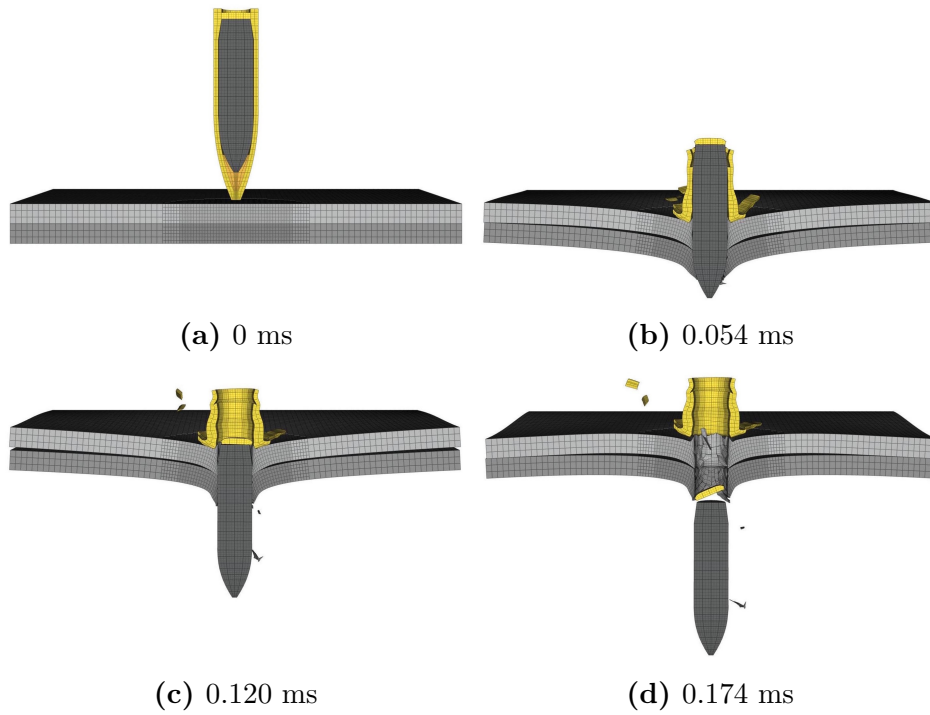
were observed to be the two main contributing energies during the perforation process. Almost all the kinetic energy goes over to local plastic work for  $v_i = 550$  m/s, while the rigid steel core with a initial velocity of 900 m/s only lost 27.7% of the kinetic energy under impact.



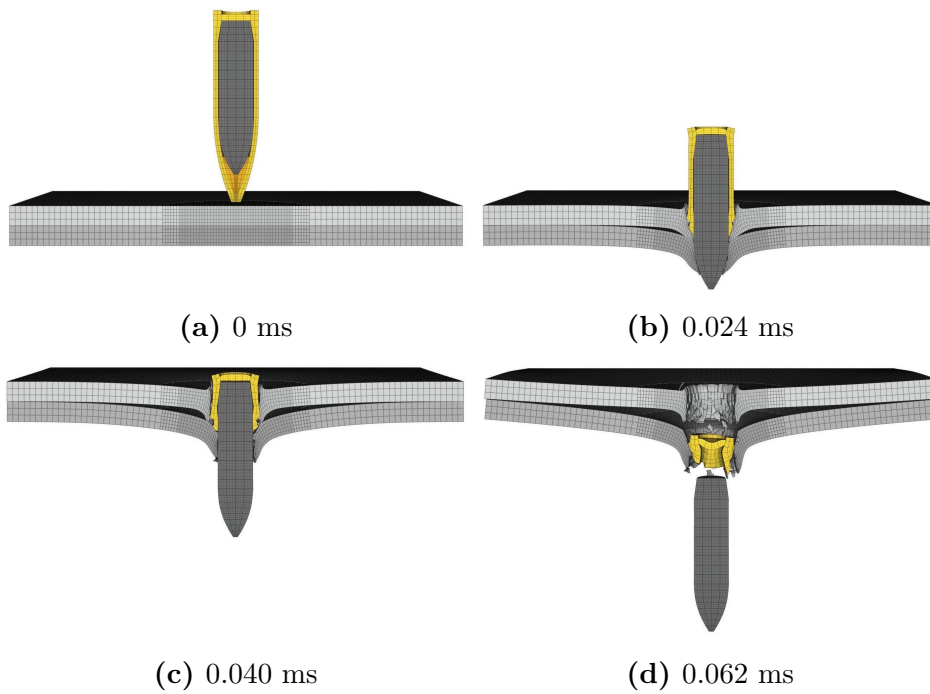
**Figure 6.4:** Energy balance plots from IMPETUS with initial velocity; **(a)**  $v_i = 550$  m/s and **(b)**  $v_i = 900$  m/s.

Figure 6.5 and 6.6 present time-lapses for the two different initial velocities. For simulations with the maximum velocity ( $v_i = 900$  m/s) it was seen that the brass jacket perforates the target plate. The same were seen in the ballistic experiments in Chapter 4. IMPETUS seemed to capture the peeling of the brass jacket under perforation very well. A closer look on the entry and exit holes in Figure 6.7 shows that ductile hole growth was the main failure mode for both impact velocities. However, some fragmentations were seen, especially for  $v_i = 900$  m/s. As expected, Figure 6.7d shows a slightly more global response for an impact where the initial velocity was close to the sub-ordnance velocity regime [2].

The amount of free nodes might give an interesting indication on how the failure modes are affected by different initial velocities and temperatures. For an increase from  $v_i = 550$  m/s to  $v_i = 900$  m/s an increase from 19331 to 43651 of free nodes were observed. A higher number of free nodes indicated more fragmentation. This substantiated what was observed on the target plates from the ballistic experiments conducted in Chapter 4.



**Figure 6.5:** Time-lapses ( $v_i = 550$  m/s and  $v_r = 184$  m/s).



**Figure 6.6:** Time-lapses ( $v_i = 900$  m/s and  $v_r = 765.7$  m/s)

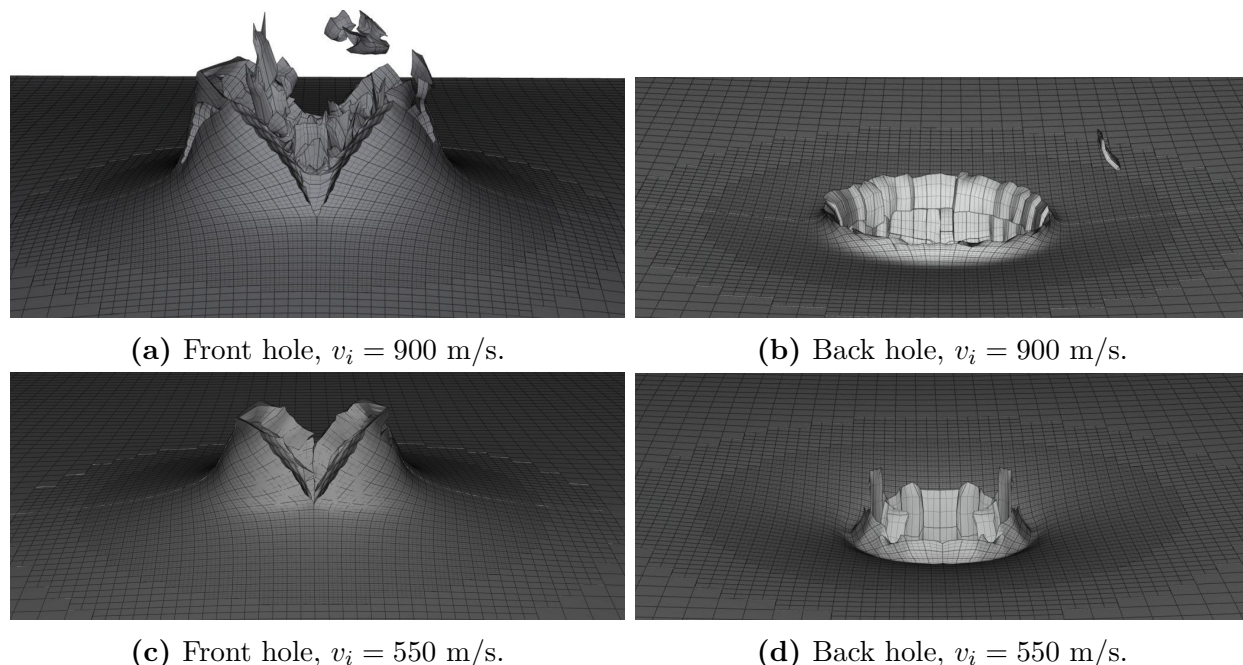


**Figure 6.7:** Close-ups of front and back holes.

To gain insight in the process near the bullet hole a closer investigation was conducted. Fifteen nodes from the impact point with a distance of 0.5 mm were picked out in the middle of the first plate. The nodes are marked with red dots in Figure 6.8. Values such as damage, temperature, plastic strain rate and maximum principal stress were extracted at 0.008 ms, 0.020 ms and 0.034 ms, for  $v_i = 900$  m/s. Note, near the impact zone some of the nodes gave a slightly non-physical results. Therefore, the overall trends in the plots were emphasized. A summary of observations from each plot in Figure 6.9 is given below.

Nodes within a distance of 2.5 mm from the impact point seemed to reach the critical CL-value (Equation 2.15) between 0.008 ms and 0.034 ms. No nodes seemed to reach the melting temperature, which is 1800 K for steels. The temperature increased to about 1500 K under perforation and decreased rapidly to RT with increasing radius. High plastic strain rates were observed near the impact area. As mentioned in Section 2.2.4 a major principal stress of about five times the yield stress indicates a brittle fracture [12]. Here, only values below five were observed, which indicated that brittle fracture did not occur. All the plots in Figure 6.9 substantiate the theory in Chapter 2 that high velocity perforation is a highly local process. Only material within a radius of about two times the projectile radius seemed to be affected.

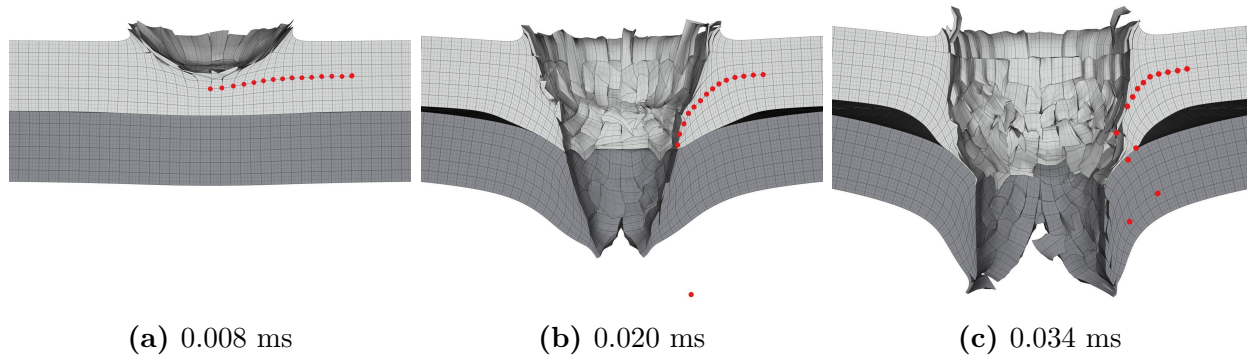


**Figure 6.8:** Sensor nodes,  $v_i = 900$  m/s and  $v_r = 765.7$  m/s.

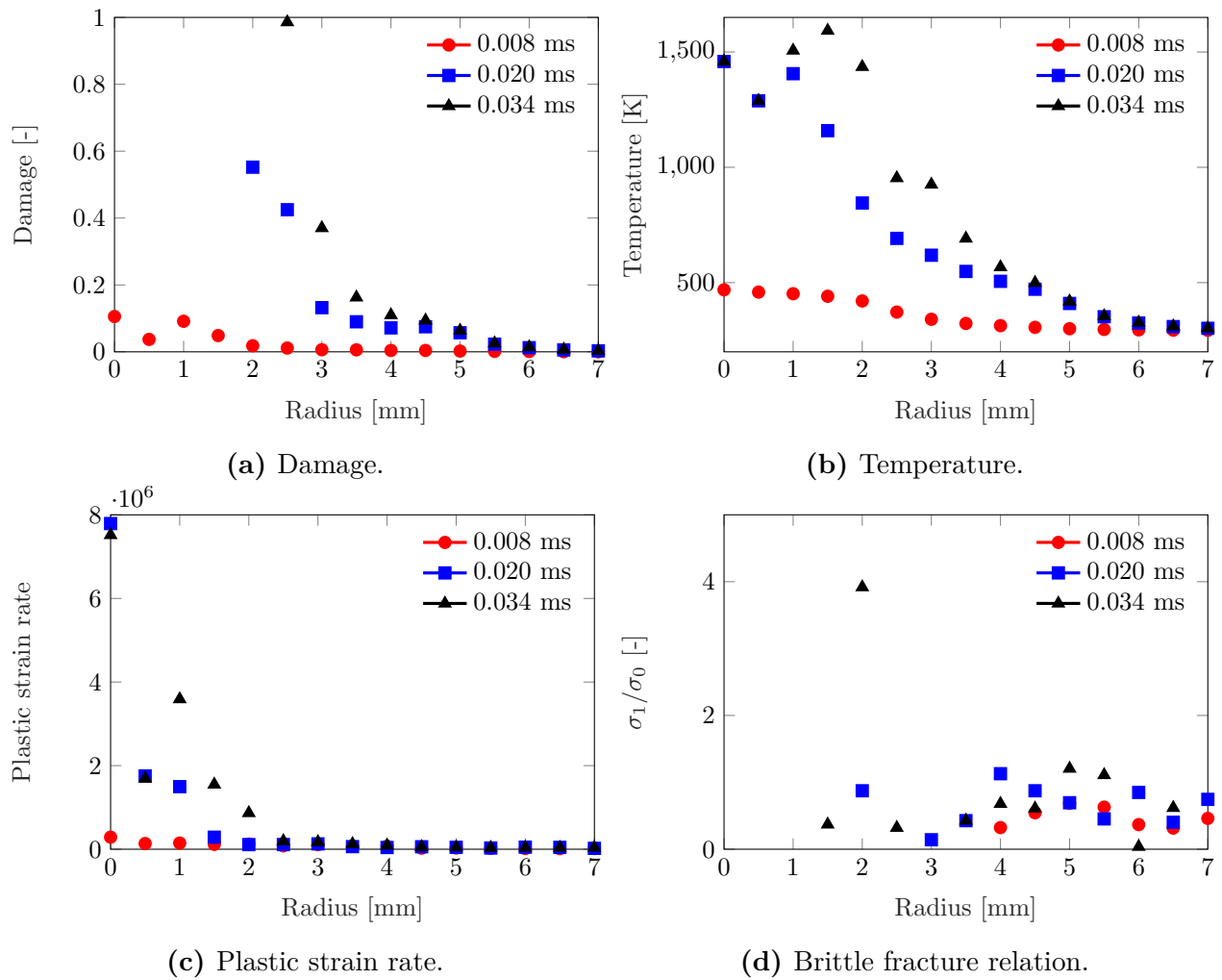


**Figure 6.9:** Outputs from nodes in Figure 6.8 during impact.

### 6.1.2 Sensitivity Study

Since these simulations are computationally expensive only simulations with initial velocities of 550 m/s and 900 m/s were performed. The effect of change in configurations, mesh, impact angle and boundary condition were investigated for Armox 500T.

#### Monolithic versus Laminated Configuration

Dey et al. [18] showed that for an ogival nose shape projectile the ballistic limit velocity decreases with a double-layered configuration for an impact in the ordnance velocity regime. The main reason for this is that no shear and tensile stresses can be transferred from one layer to another. For a blunt nosed projectile the opposite was shown. Figure 6.10 shows that the simulations for the Armox 500T steel gives results that coincide with Dey et al. [18]. Table 6.5 shows an increase of 11.3% for the ballistic limit velocity for the monolithic configuration.

**Table 6.5:** Sensitivity study: Configurations.

Configuration	$v_{bl}$ [m/s]	Deviation
Laminated	528.3	-
Monolithic	578.8	+11.3 %

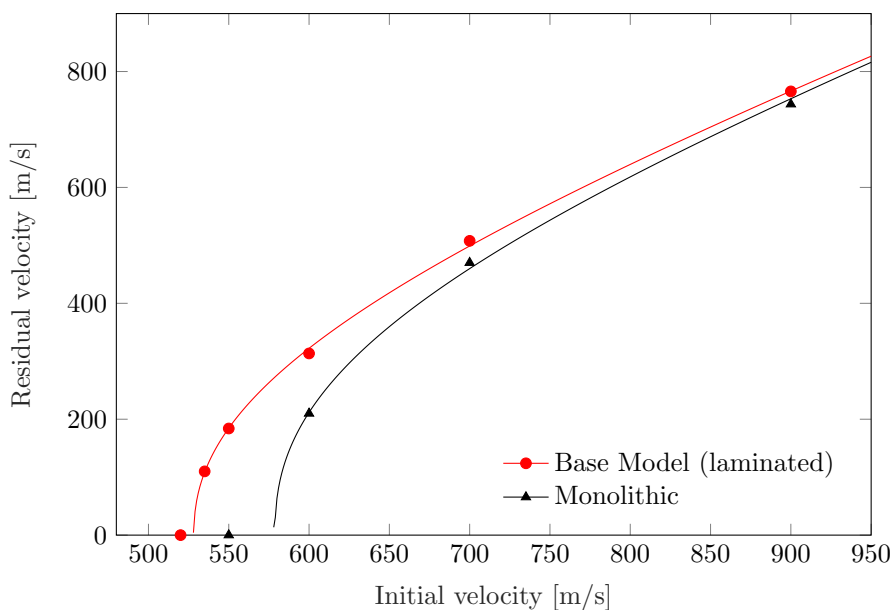


**Figure 6.10:** Ballistic limit curves for monolithic and laminated configurations.



## Mesh

In this mesh study three new mesh were established in addition to the base model mesh, which consisted of 12 elements over the thickness. Number of elements over the thickness were 6, 12, 18 and 24. Note, the number of elements over the thickness was in the impact region with the refined mesh. The impact area was reduced from a radius of 10 mm to a radius of 6.5 mm for the simulations with 24 elements over the thickness since it was not enough resources available to run the analysis. Otherwise, the models were identical to each other. The results of the study are presented in Table 6.6 and 6.7. For an initial velocity of 550 m/s an increase of the residual velocity was seen for both coarser and finer mesh. These results indicated that the residual velocity obtained from the simulations was not completely converged. A reason for this could be that the entire mesh was not scaled accordingly to the refined impact area due to low computer resources. According to Zukas and Scheffler [38] this could cause unwanted effects like unwanted reflection of stress waves. For  $v_i = 900$  m/s convergence was seen for finer mesh. The dotted line in Figure 6.11 is the residual velocity from the ballistic experiments. It should be noted that all mesh gives conservative results.

**Table 6.6:** Sensitivity study: Mesh ( $v_i = 550$  m/s).

Elm. over thickness	6	12 (base)	18	24
$v_r$ [m/s]	186.9	183.6	204.9	253.5

**Table 6.7:** Sensitivity study: Mesh ( $v_i = 900$  m/s).

Elm. over thickness	6	12 (base)	18	24
$v_r$ [m/s]	752.7	765.6	777.9	780.4

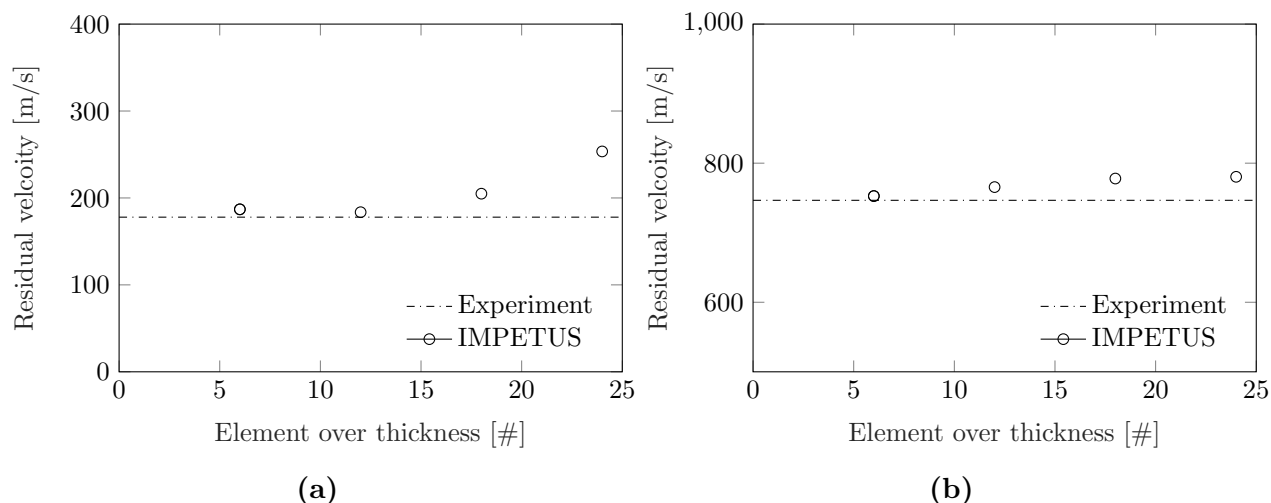


**Figure 6.11:** Sensitivity study; (a)  $v_i = 550$  m/s and (b)  $v_i = 900$  m/s.

## Impact Angle

A certain impact angle was observed for some of the projectiles in the time lapses presented in Section 4.2.1. As mentioned in Section 2.1.1 the impact angle is defined as the angle between the target normal and the symmetry axis. In this study three different angles were investigated,  $2^\circ$ ,  $5^\circ$  and  $10^\circ$ , in addition to  $0^\circ$  for initial velocities of 550 m/s and 900 m/s. In Figure 6.12 the different impact angles are shown. Here, the oblique impact angle was zero. In other words, the velocity vector is assumed parallel to the target normal. The angle situation looks like  $\gamma = \alpha = \theta \neq 0$  and  $\varphi=0$ . Table 6.8 and 6.9 present the residual velocity for  $v_i = 550$  m/s and  $v_i = 900$  m/s respectively. For an initial velocity of 550 m/s it was observed that the residual velocity starts to decrease dramatically for angles above  $2^\circ$ . A deviation in residual velocity of 57.2% was observed for an impact angle of  $10^\circ$  compared to a normal impact. The residual velocity for an impact with  $v_i = 900$  m/s starts to drop for angles above  $5^\circ$ . For  $10^\circ$  angle a deviation of 13% was seen. The angle effect seemed therefore to be largest for velocities near the ballistic limit velocity.

**Table 6.8:** Sensitivity study: Impact angle ( $v_i = 550$  m/s).

Impact Angle	$0^\circ$	$2^\circ$	$5^\circ$	$10^\circ$
$v_r$ [m/s]	183.6	182.0	151.3	78.5

**Table 6.9:** Sensitivity study: Impact angle ( $v_i = 900$  m/s).

Impact Angle	$0^\circ$	$2^\circ$	$5^\circ$	$10^\circ$
$v_r$ [m/s]	765.6	758.4	735.6	665.5

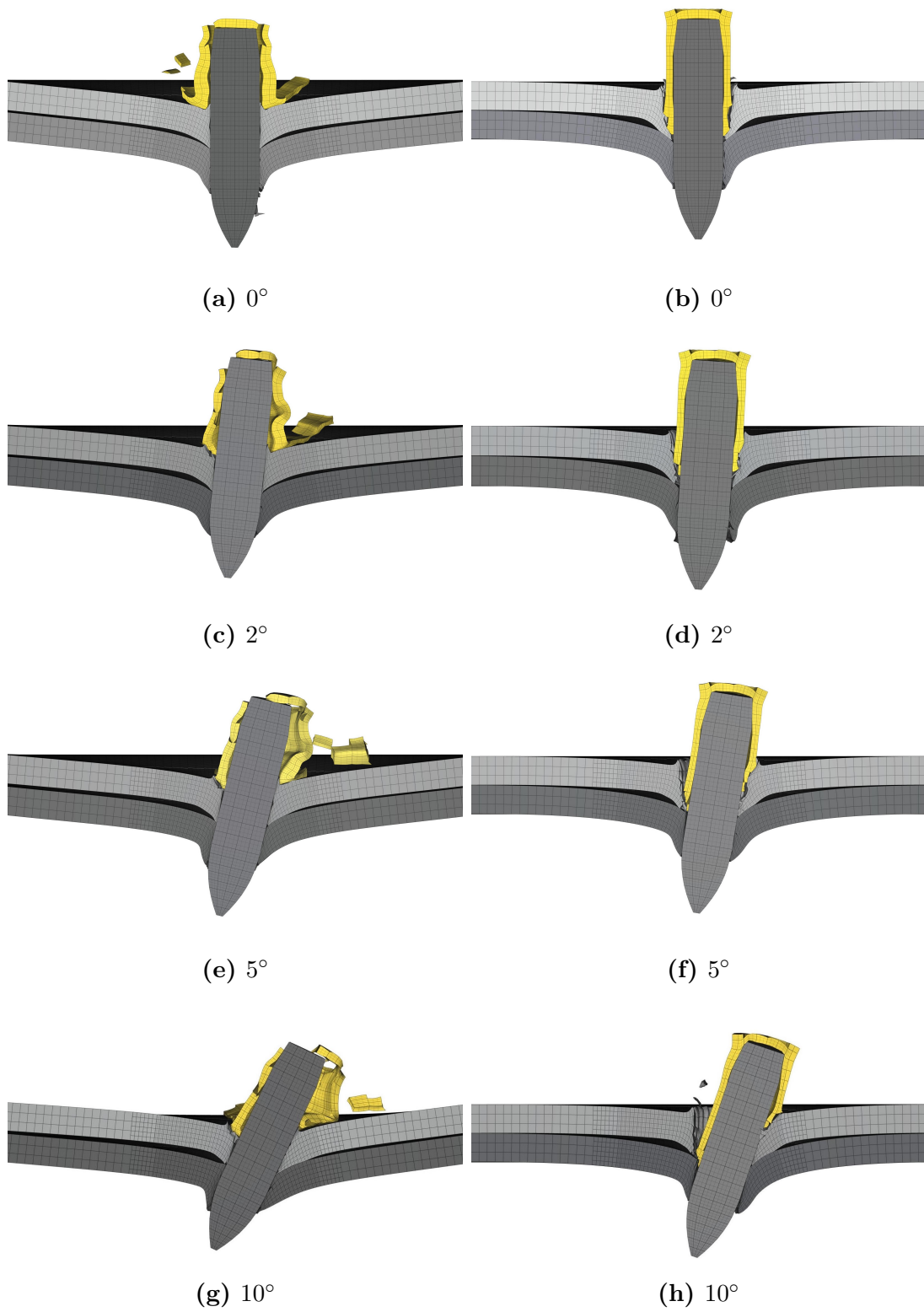


**Figure 6.12:** (a), (c), (e) and (g)  $v_i = 550$  m/s at 0.072 ms and (b), (d), (f) and (h)  $v_i = 900$  m/s at 0.03 ms.

## Boundary Conditions

Orthe and Thorsen [33] showed that the boundary conditions only has a minor effect on the residual velocity for impacts on a low-strength steel. A small study was therefore conducted to see if the boundary conditions affected the residual velocity more for a high-strength steel than for a low-strength steel. Figure 6.13 shows that the residual velocity was not sensitive to the applied boundary conditions. Only a deviation of 0.21% was observed for  $v_i = 900$  m/s. As expected the boundary conditions has a larger influence on the residual velocity for impacts with initial velocities near the ballistic limit velocity. The main reason for this is the more global response of the target plate. However, the deviation was still small. So both high-strength steel and low-strength steel is not very sensitive to boundary condition, especially for high velocity impacts. Table 6.10 lists the residual velocities.

**Table 6.10:** Sensitivity study: Boundary conditions.

Boundary conditions	$v_i$ [m/s]	$v_r$ [m/s]	Deviation
Partition clamped (base model)	550	183.6	-
No boundary conditions	550	170.0	-7.41%
Partition clamped (base model)	900	765.6	-
No boundary conditions	900	767.2	+0.21%

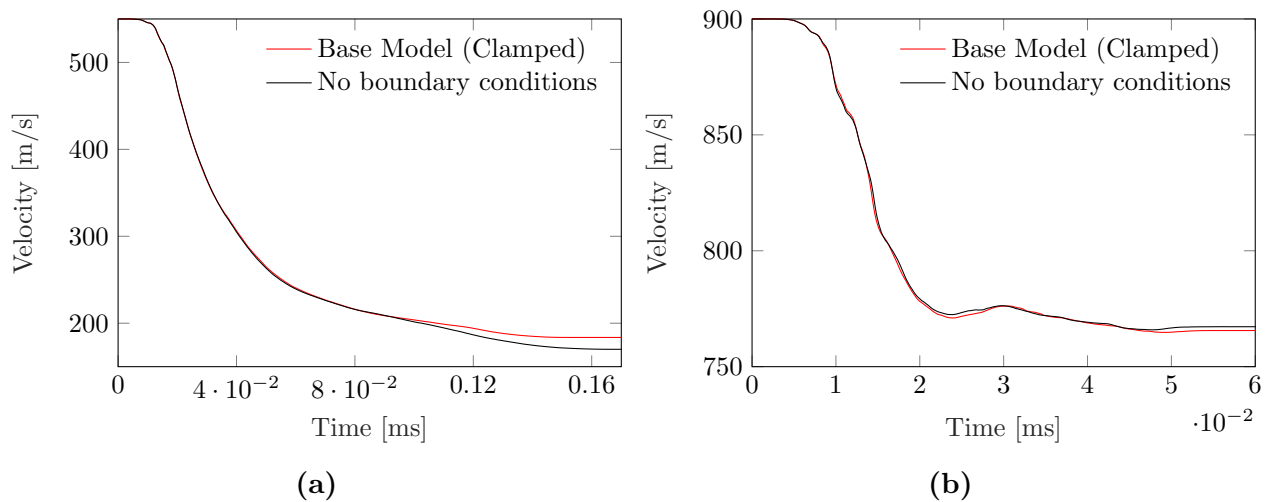


**Figure 6.13:** Effect of boundary conditions; (a)  $v_i = 550$  m/s and (b)  $v_i = 900$  m/s.

### 6.1.3 Effect of Temperature

A larger study was conducted to investigate the effect of the temperature on the ballistic properties of the material. From the ballistic experiments conducted in Chapter 4 the material strength seemed to increase for decreasing temperatures, while the target plate still mainly failed with ductile hole growth. The yield stress for Armox 500T at  $-40\text{ }^{\circ}\text{C}$  was found by using

$$A = \frac{\sigma_y}{1 - \left(\frac{T_r - T_0}{T_m - T_0}\right)^m} \quad (6.2)$$

with  $m = 1$ . The relation is obtained from the MJC constitutive relation [12].

Figure 6.14a illustrates the linear relation between the temperature and the yield stress. At  $-40\text{ }^{\circ}\text{C}$  (233 K) the yield stress was found to be 1290 MPa, this is a 4% increase compared to RT (293 K). The material hardening up to necking is illustrated in Figure 6.14b. Note that the other Voce material hardening parameters were assumed to be equal [12].

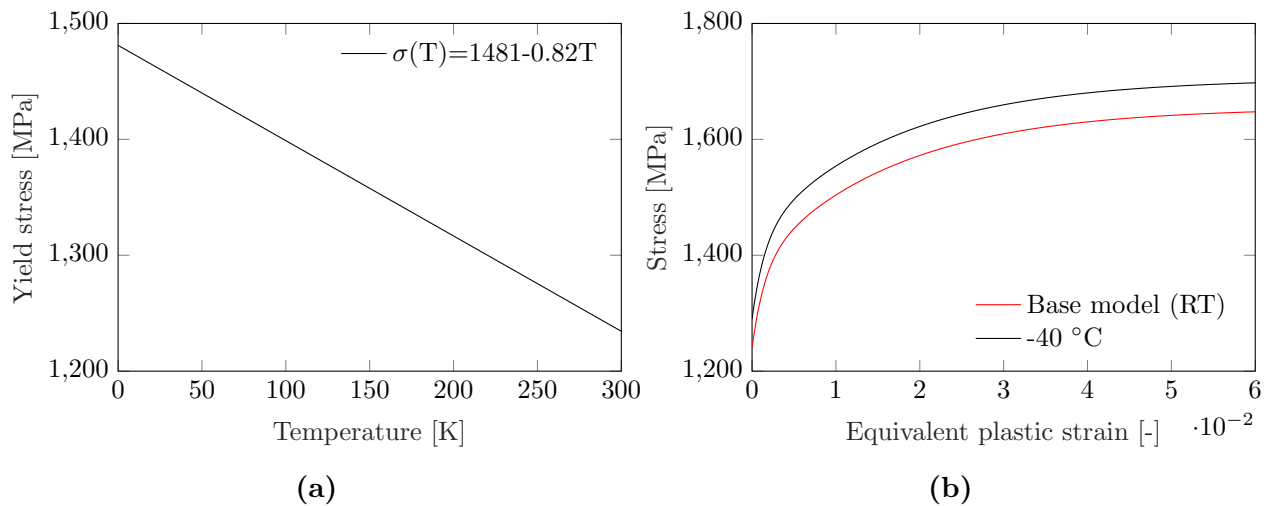


**Figure 6.14:** (a) Temperature - yield stress relation and (b) strain hardening to necking at different temperatures.

The numerical model at  $-40\text{ }^{\circ}\text{C}$  was almost identical to the base model. The only differences were that  $\sigma_0 = 1290\text{ MPa}$  and that  $T_{Ref} = T_0 = 233\text{ K}$ . A ductile fracture criterion was still defined, since there was no sign of brittle fracture modes in the component experiments at low temperature. Note that the  $W_c$  parameter is given by the area under the true stress curve at RT. Therefore, fracture will occur at lower plastic strains due to the higher yield stress at low temperatures. Figure 6.15 presents the ballistic limit curve at  $-40\text{ }^{\circ}\text{C}$ . An increase of 1.73%

was observed for the ballistic limit velocity compared to RT. The curve fitted Recht-Ipson parameters are listed in Table 6.11.

**Table 6.11:** Recht-Ipson parameters.

	$a$	$p$	$v_{bl}$ [m/s]	Deviation in $v_{bl}$
Base model (RT)	1	2.24	528.3	-
-40 °C	1	2.24	537.4	+1.73%

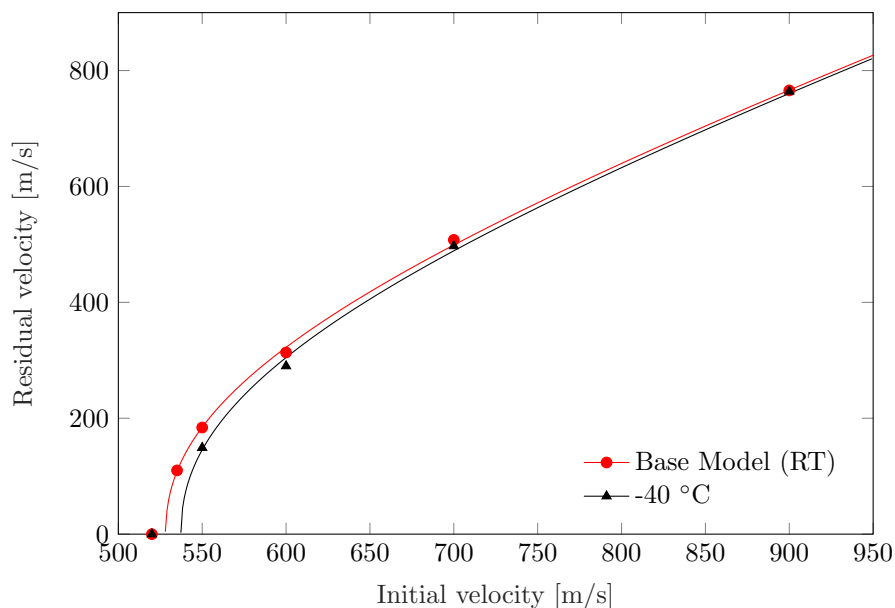


**Figure 6.15:** Ballistic limit curves at different temperatures.

Figure 6.16a shows that the  $\sigma_1/\sigma_0$  relation was not sensitive for a change in this temperature range. All the values were shown to be below five. Furthermore, only an increase of free nodes from 43651 to 45439 were detected for simulations at RT and -40°C respectively. Figures 6.16b and 6.17 substantiate these observations. No significant change in failure mode was seen for entry and exit holes.

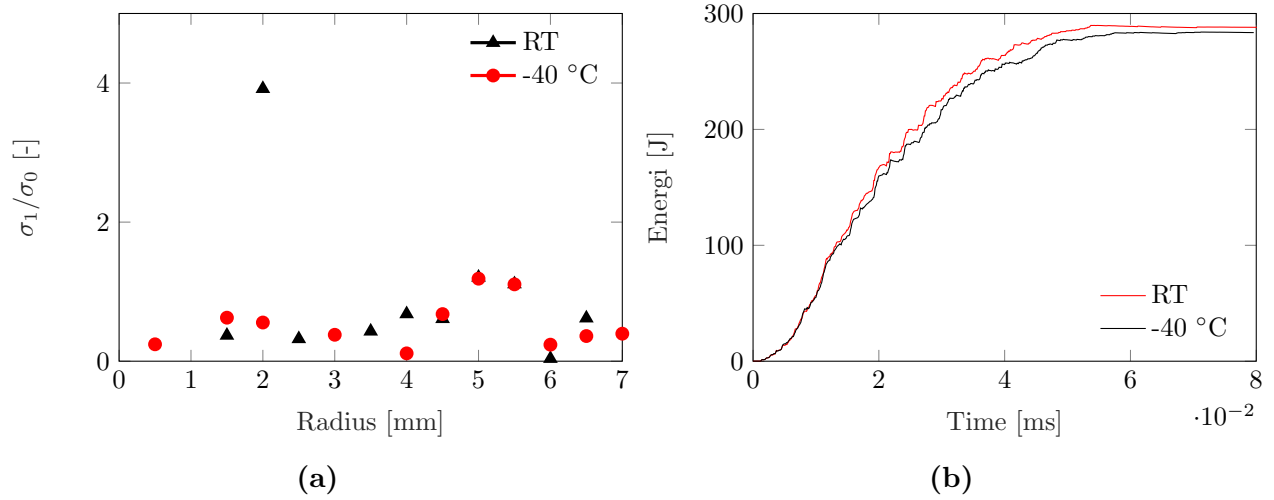


**Figure 6.16:** (a) Brittle fracture relation at 0.034 ms and (b) kinetic energy of free nodes.

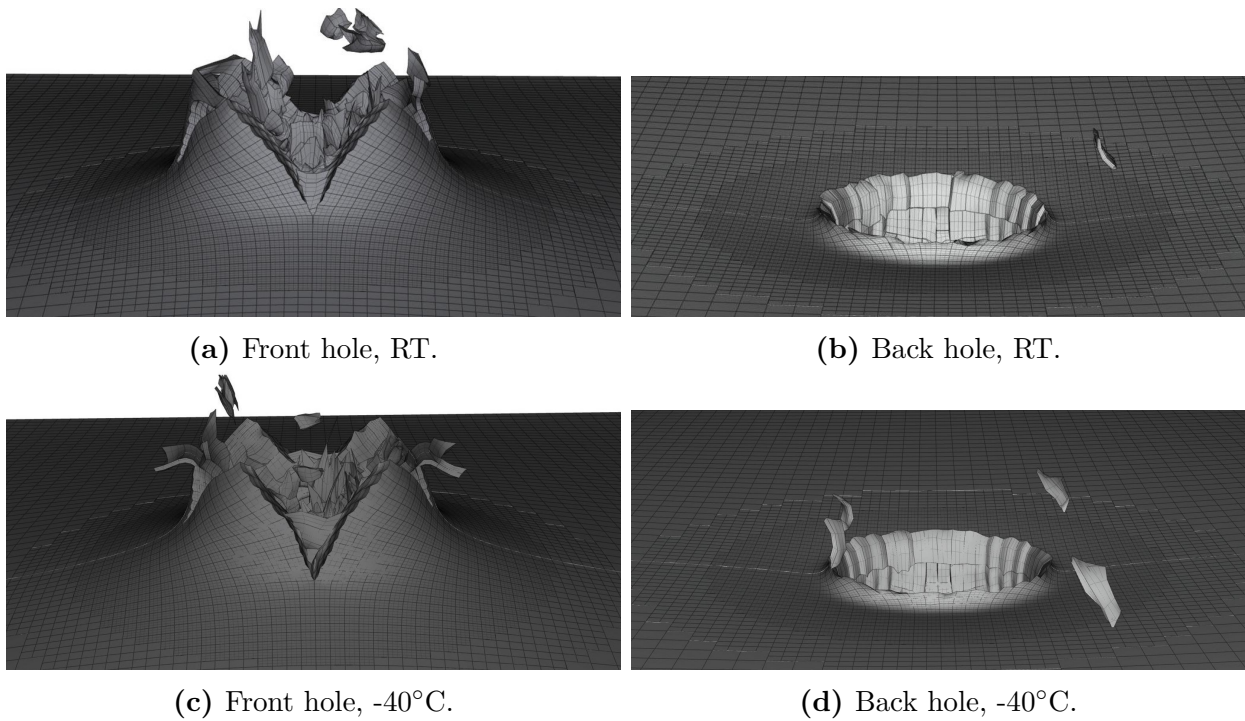


**Figure 6.17:** Close-ups of front and back holes at different temperatures for  $v_i = 900$  m/s.

## 6.2 NVE 36 Steel

### 6.2.1 Base Model

The NVE 36 base model is almost identical to the Armox 500T base model presented in Section 6.1.1. The differences are the material constants, found in Table 5.9, the monolithic configuration and the mesh size in the thickness direction due to different plate thicknesses for the two materials. Here, the element size in the thickness direction was 1 mm instead of 1.167 mm outside the impact area and 0.5 mm instead of 0.58 mm inside the impact area. For a more detailed description about the APM2 7.62 mm bullet, boundary conditions and contact, see Section 6.1.1. The target plate is illustrated in Figure 6.18.

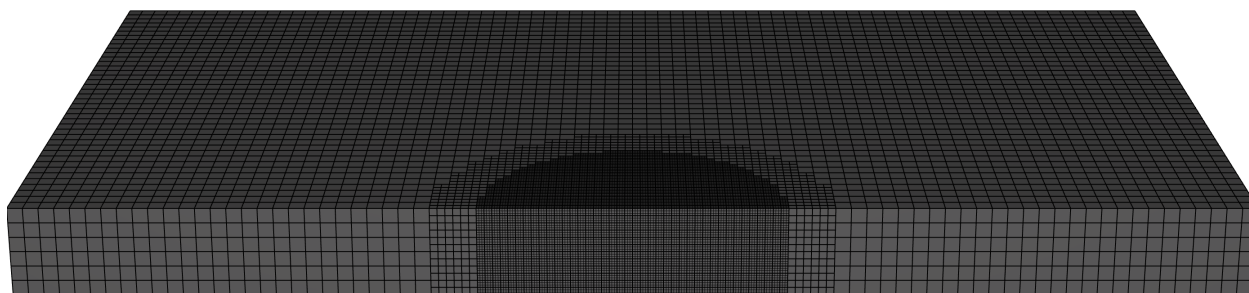


**Figure 6.18:** Meshed monolithic NVE 36 configuration (6 mm).

### Results

Figure 6.19 shows the ballistic limit curves obtained from the base model and the experimental tests. The Recht-Ipson parameters are presented in Table 6.12. It can be observed that the base model gives a conservative result compared to the ballistic limit velocity found from the experimental results. It underestimates the ballistic velocity with 8.26%.

**Table 6.12:** Recht-Ipson parameters - NVE 36 6 mm plates.

	$a$	$p$	$v_{bl}$ [m/s]	Deviation in $v_{bl}$
Experiment	1	2.22	401.9	-
Base model	1	2.26	368.7	-8.26%

Figure 6.20 presents the total energy balance for  $v_i = 400$  m/s and  $v_i = 900$  m/s. Only a deviation of less than one percentage was observed for both impact velocities. The 5%



criterion was satisfied in other words. Time-lapses for both initial velocities are illustrated in Figure 6.21 and 6.22.

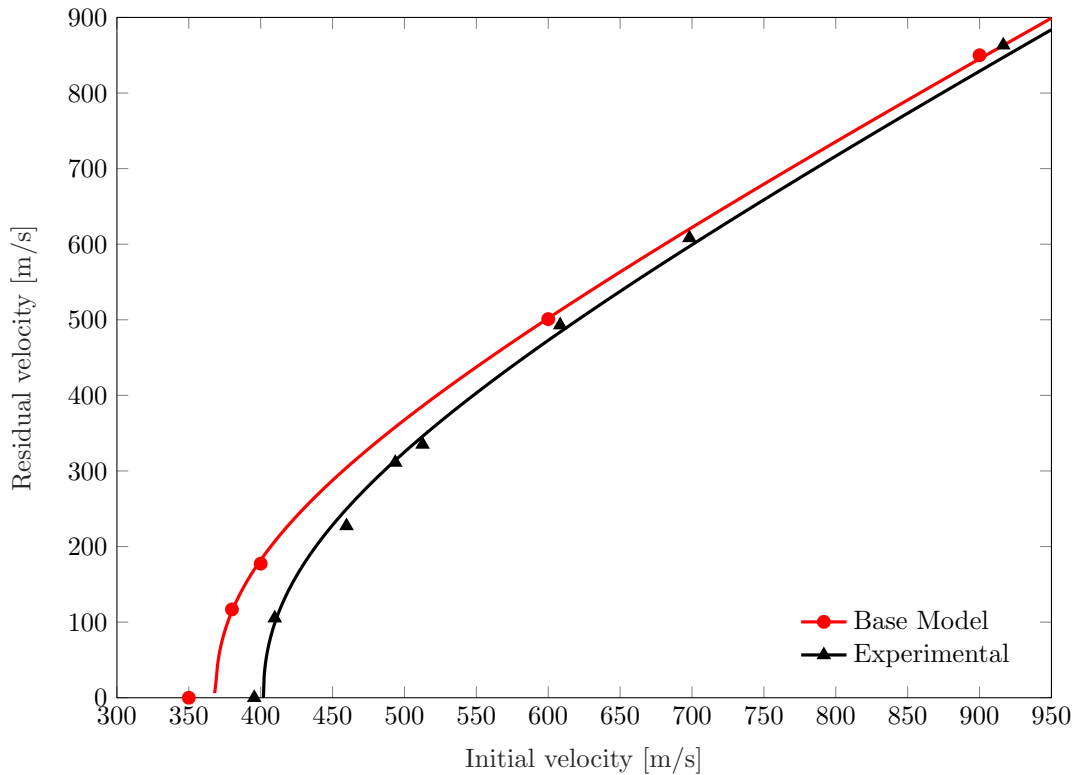


**Figure 6.19:** Ballistic limit curves from experimental data and numerical simulations in IMPETUS.

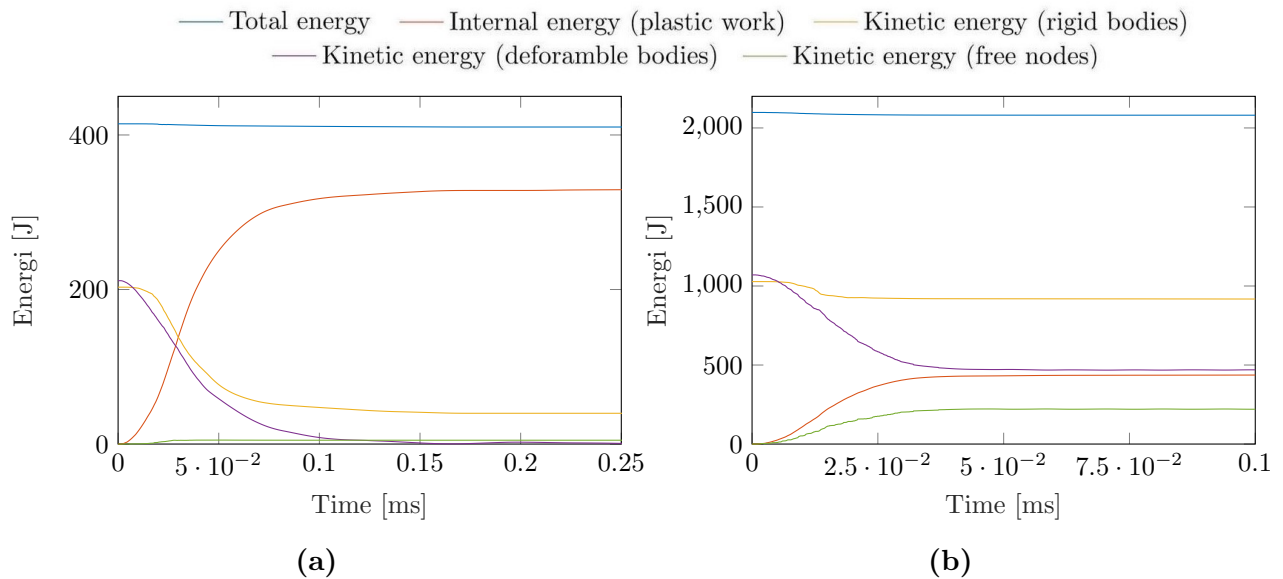


**Figure 6.20:** (a) Energy balance and (b) internal energy plot for  $v_i = 900$  m/s .

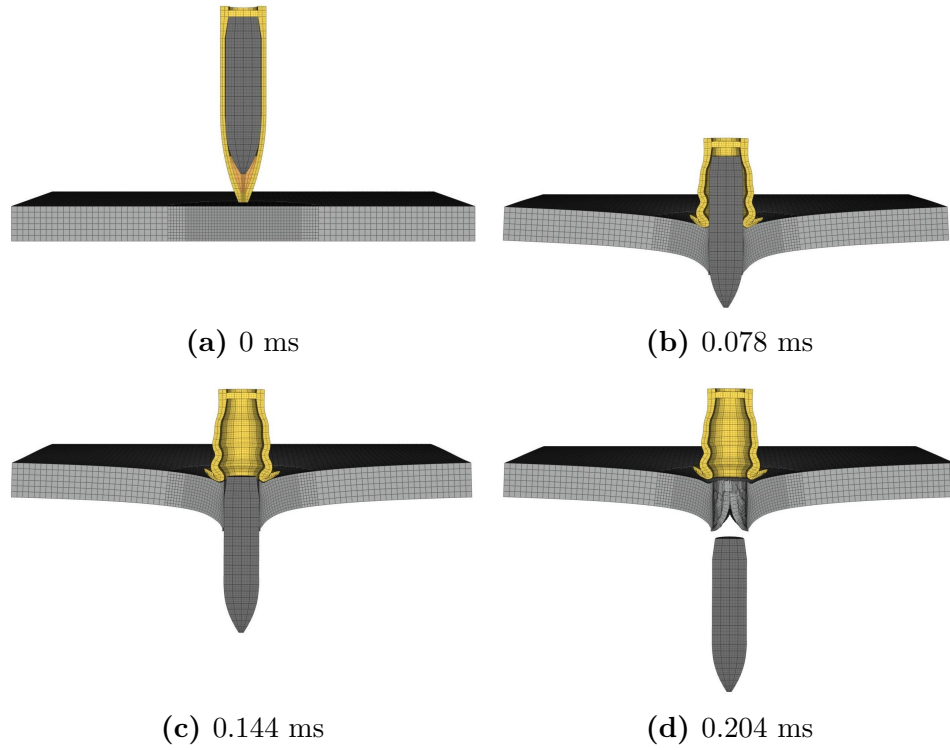


**Figure 6.21:** Time-lapses ( $v_i = 400$  m/s and  $v_r = 177.4$  m/s).

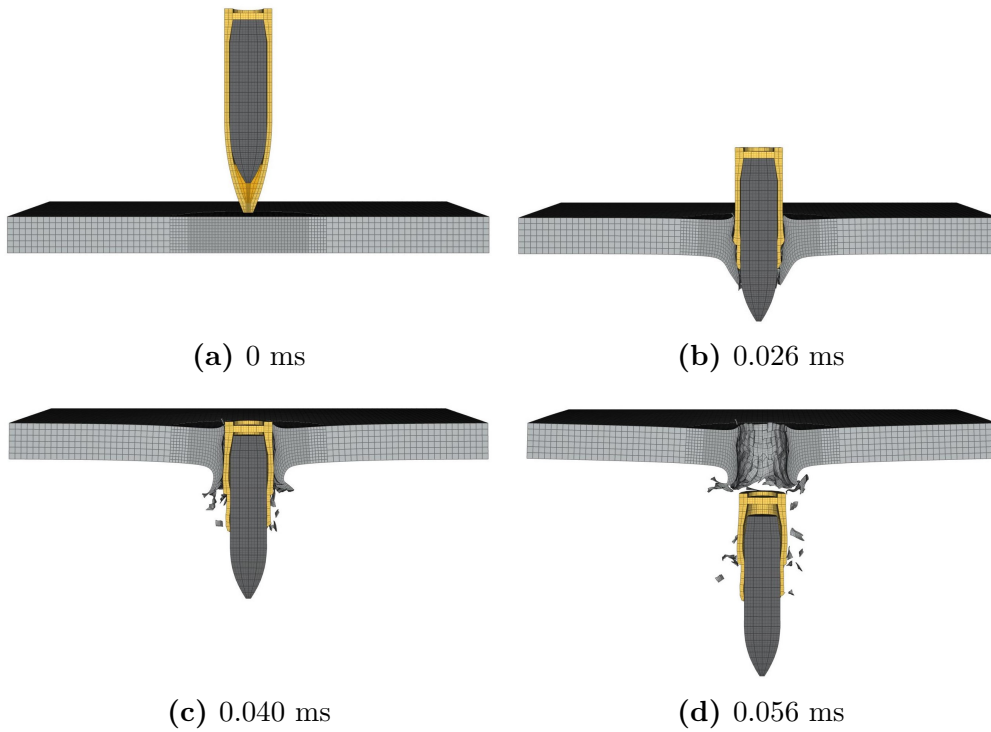


**Figure 6.22:** Time-lapses ( $v_i = 900$  m/s and  $v_r = 850$  m/s).

By inspecting Figure 6.23 the main failure mode seemed to be ductile hole growth. However, some fragmentations were also seen for NVE 36 as for Armox 500T. The amount of fragmentation observed was higher for simulations with high initial velocity than for simulations with low initial velocity. An increase in free nodes from 16186 to 29061 were observed for  $v_i = 400$  m/s and  $v_i = 900$  m/s respectively.

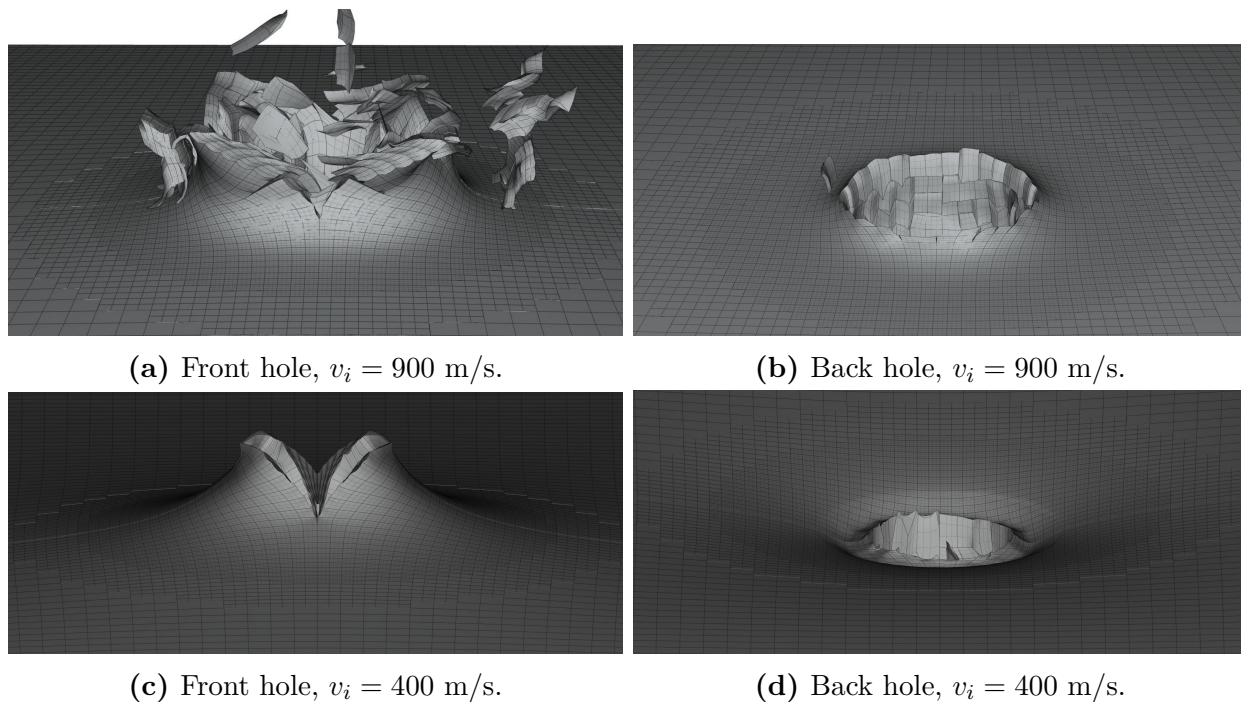
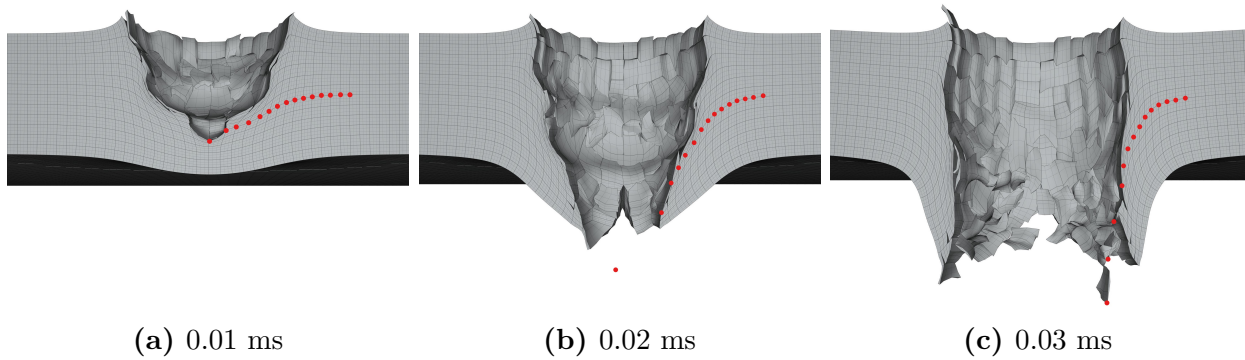


**Figure 6.23:** Close-ups of front and back holes.

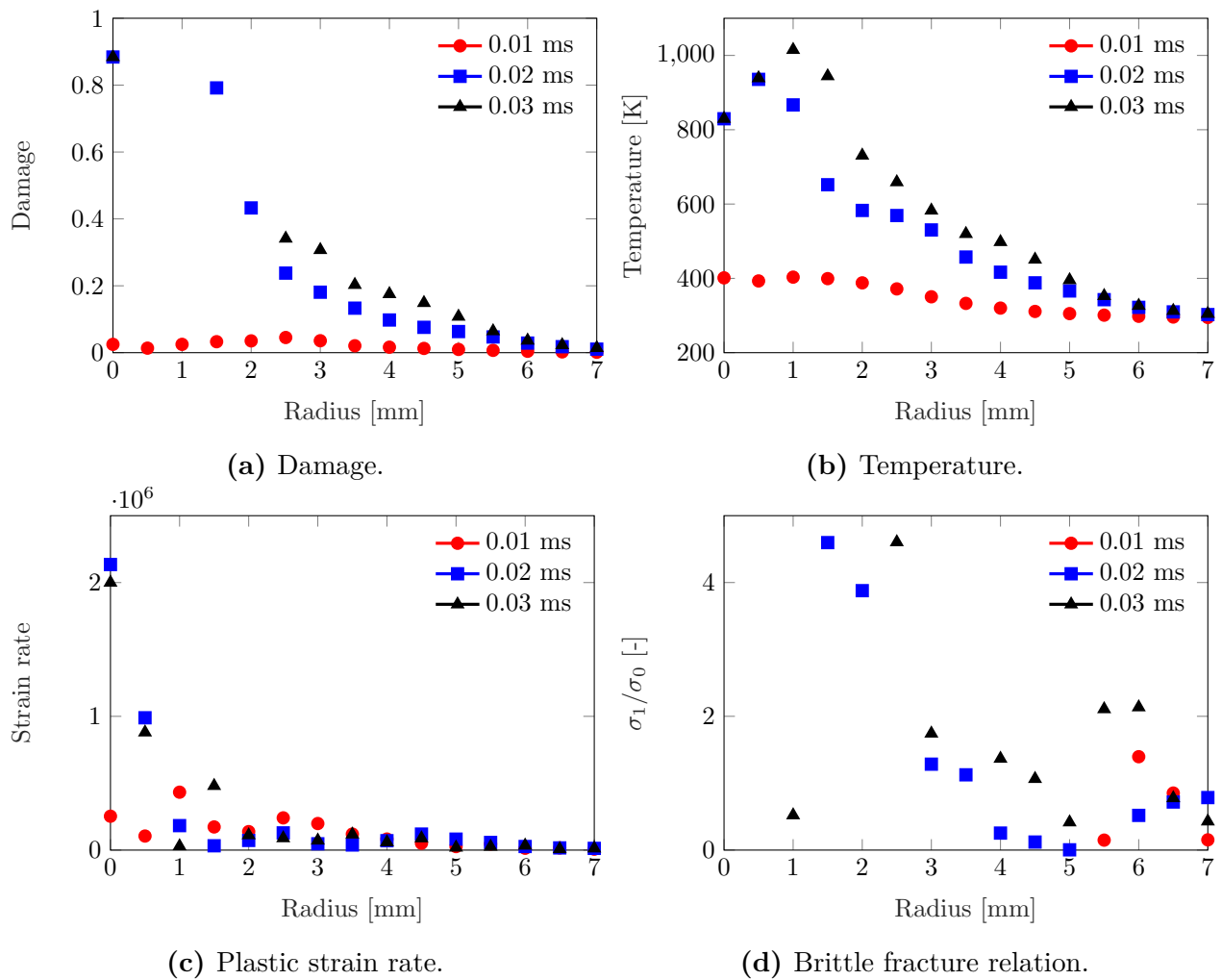
Also for NVE 36 a closer investigation was conducted to gain insight in the process near the bullet hole. Fifteen nodes from the impact point with a distance of 0.5 mm were picked out in the middle of the target plate. The nodes are marked with red dots in Figure 6.24. The same values such as damage, temperature, plastic strain rate and maximum principal stress were taken out as for Armox 500T. Furthermore, the values were extracted at 0.01 ms, 0.02 ms and 0.03 ms, for  $v_i = 900$  m/s. It should also be noted that the overall trends in the plots were emphasized since some nodes near the impact zone give slightly non-physical results. Below is a summary of observation from each plot in Figure 6.25.

Figure 6.25a indicates that elements within a distance of 2 mm from the impact point reached the critical fracture value of unity (Equation 2.15) after 0.03 ms. For the temperature an increase of about 750 K was observed near the contact area between the projectile and the target plate. The temperature decreased rapidly to 273 K with increasing radius and at a

radius of 7 mm no deviation in temperature was seen. Additionally, high plastic strain rates were observed near the impact area. For the brittle fracture relation only values below five were observed, which indicated that no brittle fracture occurred. Note that values below zero (compression) were neglected since only tensile stresses were of interest.



**Figure 6.24:** Sensor nodes marked with red dots.  $v_i = 900$  m/s and  $v_r = 850$  m/s.



**Figure 6.25:** Outputs from nodes in Figure 6.24 during impact.

## 6.2.2 Sensitivity Study

For NVE 36 the simulations conducted in the sensitivity study were run with initial velocities of 400 m/s and 900 m/s. The effects of change in mesh, strain rate hardening, temperature softening, fracture parameter and impact angle were investigated. Descriptions of equal sensitive studies conducted for Armox 500T as for NVE 36 are not repeated here. They can be found in Section 6.1.2.

### Mesh

Table 6.13 and 6.14 present the results from the study. For both initial velocities only relatively small differences in residual velocity were seen for different mesh. The results presented in Figure 6.26 indicates that the residual velocity from the simulations had nearly converged. Note that the residual velocity for an impact with  $v_i = 400$  m/s was found to be zero from the ballistic limit curve obtained in Chapter 4.

**Table 6.13:** Sensitivity study: Mesh ( $v_i = 400$  m/s).

Elm. over thickness	6	12 (base)	18	24
$v_r$ [m/s]	181.7	177.1	181.1	193.5

**Table 6.14:** Sensitivity study: Mesh ( $v_i = 900$  m/s).

Elm. over thickness	6	12 (base)	18	24
$v_r$ [m/s]	839.2	850.8	850.5	851.3

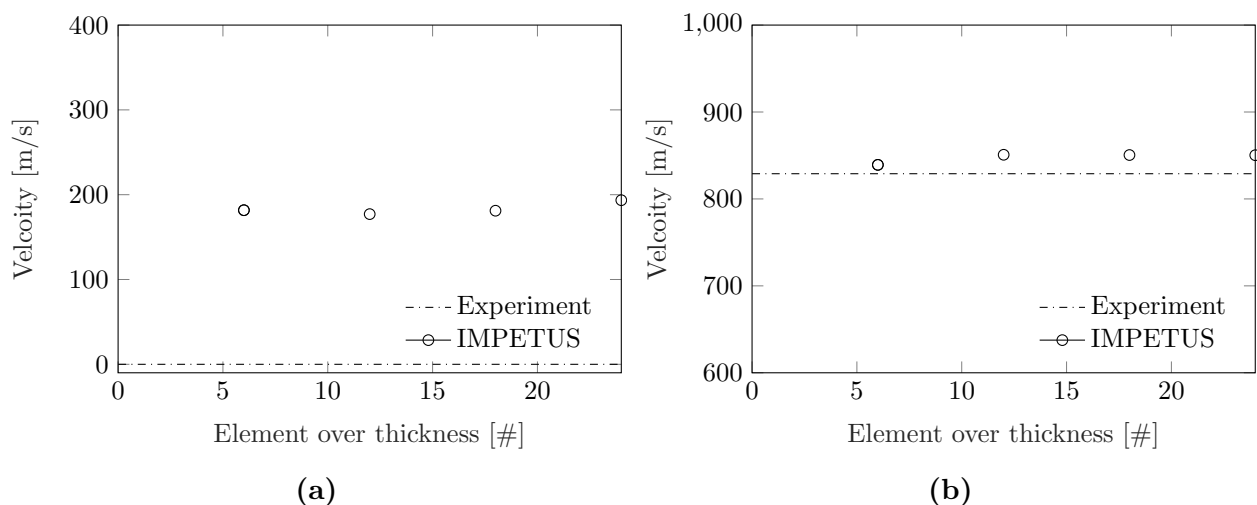


**Figure 6.26:** Sensitivity study; (a)  $v_i = 400$  m/s and (b)  $v_i = 900$  m/s.

## Strain Rate Hardening and Temperature Softening

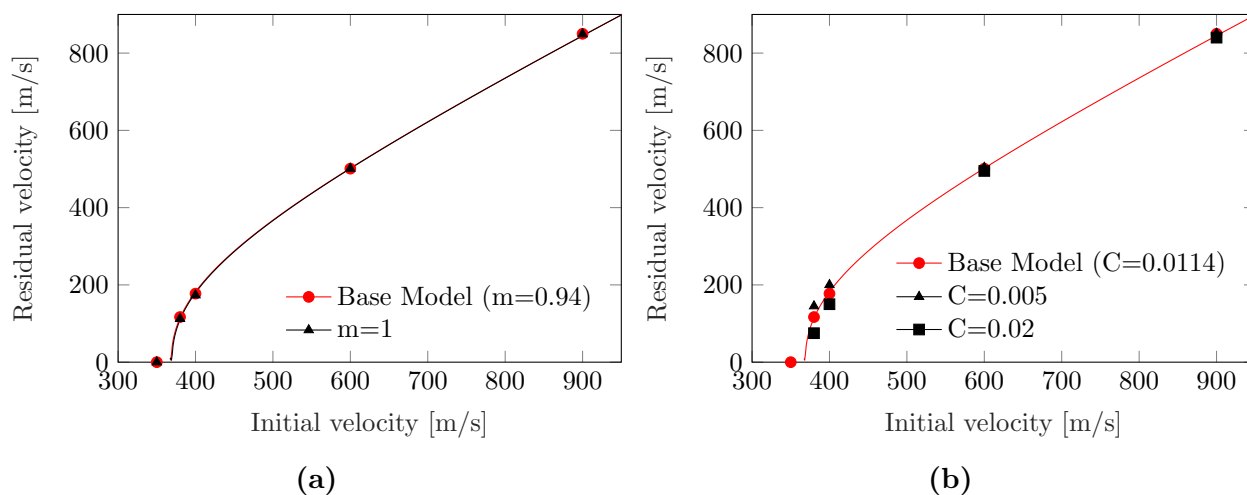
As mentioned these two parameters were found in the literature. A sensitivity study was therefore conducted to see if these two parameters affected the residual velocity and the ballistic limit velocity.

Table 6.15 shows that the residual velocity obtained from simulations with an impact velocity of 900 m/s is not sensitive to a change in the temperature softening parameter. Additionally, the ballistic limit curve was found for  $m = 1$ . Only a deviation of +0.3% was observed for the ballistic limit velocity compared to the results from the base model ( $m = 0.94$ ). The ballistic limit curves are presented in Figure 6.27a.

Two values were checked for the strain rate hardening parameter,  $C = 0.005$  and  $C = 0.02$ , in addition to the base model ( $C = 0.0114$ ). The results are presented in Figure 6.27b. As expected from looking on the MJC constitutive relation in Equation 2.13, the ballistic limit velocity increased with an increasing  $C$ -value due to an increase of the strain rate dependency. Børvik et al. [9] showed that for an increase of the yield stress, the strain rate hardening parameter was reduced. Therefore, the  $C$ -value found for Weldox 460E is assumed to give a conservative result due to a higher yield stress for Weldox 460E than for NVE 36.

**Table 6.15:** Sensitivity study: Temperature softening ( $v_i = 900$  m/s).

$m$	0.94	1	2	3	4
$v_r$ [m/s]	850.4	849.2	846.0	845.2	844.3



**Figure 6.27:** Sensitivity study: (a) Temperature softening parameter and (b) strain rate hardening parameter

### Cockcroft-Latham Parameter

Different failure strain was observed for the quasi-static tensile tests conducted in Section 3.2.3, especially between the two directions. Specimens that were extracted out in  $90^\circ$  with respect to the rolling direction were shown to have approximately 30% higher failure strain than the  $0^\circ$ -direction. Therefore, a study was conducted to see how sensitive the numerical model was for the Cockcroft-Latham parameter. Simulations with  $W_C = 1000$  MPa were run and only a deviation in the ballistic limit velocity of -0.43 % was observed (see Table 6.16).

**Table 6.16:** Sensitivity study: Cockcroft-Latham parameter.

$W_C$ [MPa]	$v_{bl}$ [m/s]	Deviation
1430	368.7	-
1000	367.1	-0.43 %

### Impact Angle

In this sensitivity study three different angles were investigated,  $2^\circ$ ,  $5^\circ$  and  $10^\circ$ , in addition to  $0^\circ$  for initial velocities of 400 m/s and 900 m/s. In Figure 6.28 the different impact angles are shown. The angle situation looks like  $\gamma = \alpha = \theta \neq 0$  and  $\varphi=0$ .

Table 6.17 and 6.18 present the residual velocity for  $v_i = 400$  m/s and  $v_i = 900$  m/s respectively. The same tendencies were seen for NVE 36 as for Armox 500T. The angle effect seemed to be largest for velocities near the ballistic limit velocity and for angles of  $10^\circ$  the residual velocity start to drop dramatically.

**Table 6.17:** Sensitivity study: Impact angle ( $v_i = 400$  m/s).

Impact Angle	$0^\circ$	$2^\circ$	$5^\circ$	$10^\circ$
$v_r$ [m/s]	177.1	182.3	176.3	146.1

**Table 6.18:** Sensitivity study: Impact angle ( $v_i = 900$  m/s).

Impact Angle	$0^\circ$	$2^\circ$	$5^\circ$	$10^\circ$
$v_r$ [m/s]	850.9	846.2	835.8	807.9



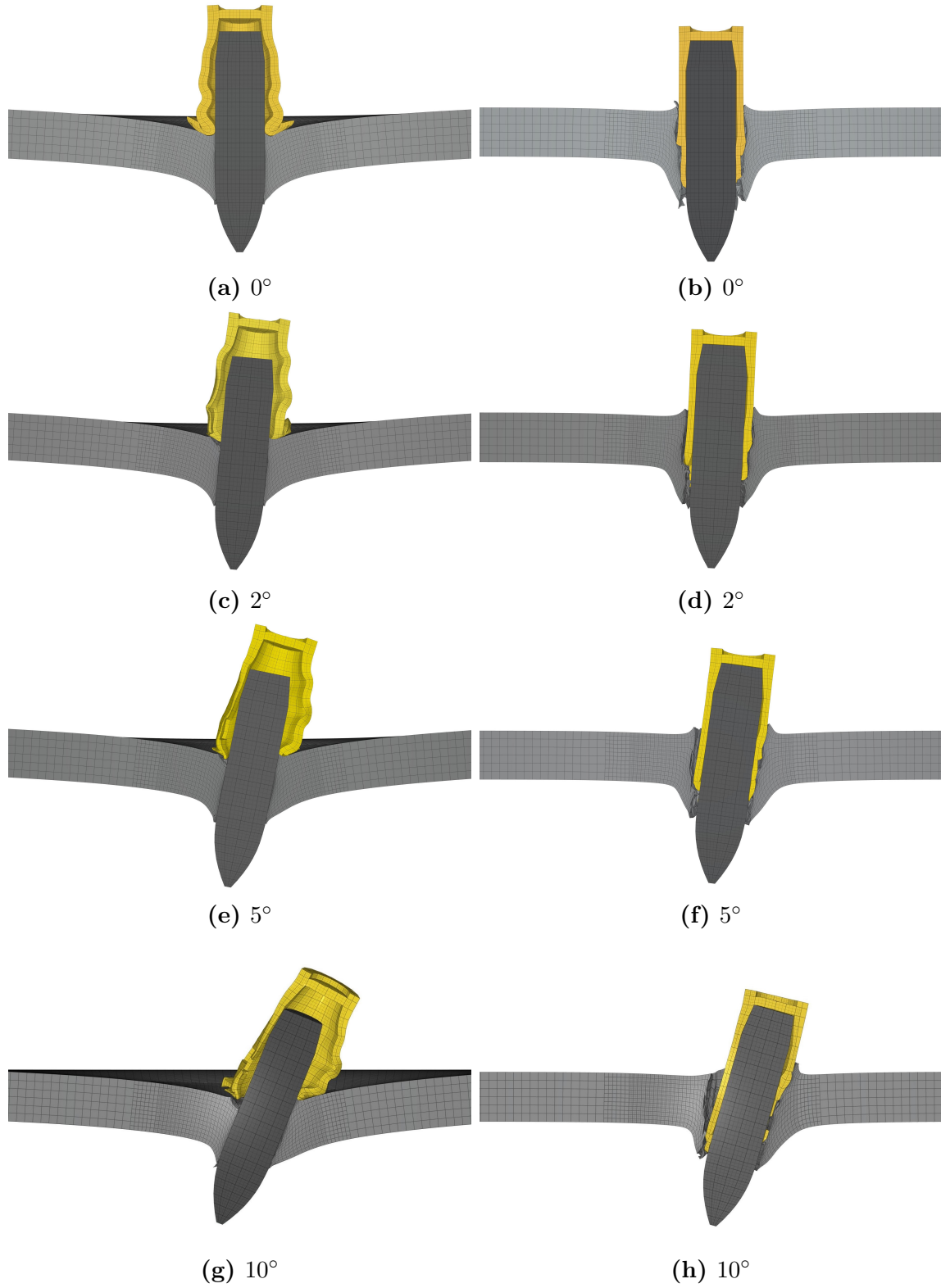


**Figure 6.28:** (a), (c), (e) and (g)  $v_i = 400$  m/s at 0.09 ms and (b), (d), (f) and (h)  $v_i = 900$  m/s at 0.028 ms

### 6.2.3 Effect of Temperature

The temperature softening parameter was set to unity, since the sensitivity study conducted on the  $m$ -value showed that the ballistic limit curve was not sensitive for a change from  $m = 0.94$  to  $m = 1$ . The linear relation between the temperature and the yield stress in Figure 6.29a was therefore obtained from Equation 6.2. At  $-40\text{ }^{\circ}\text{C}$  the yield stress was found to be 234 MPa, this is a 4% increase compared to RT. The material hardening at  $-40\text{ }^{\circ}\text{C}$  is presented in Figure 6.29b. Note, also for NVE 36 the other Voce material hardening parameters were assumed to be equal.

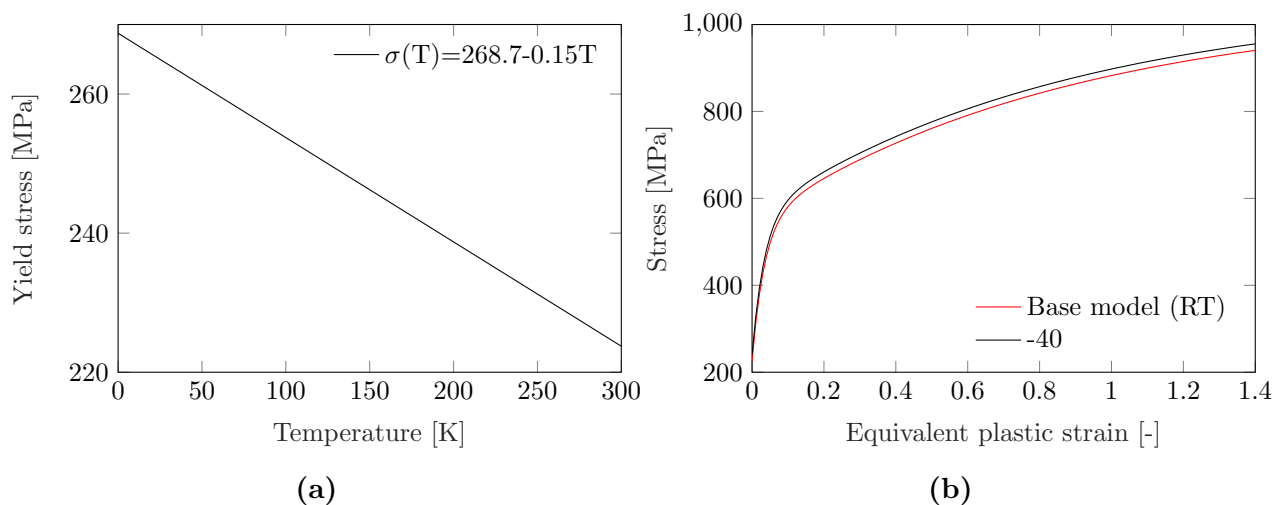


**Figure 6.29:** (a) Temperature - yield stress relation and (b) strain hardening at different temperatures.

The only differences between the numerical simulations were that  $\sigma_0 = 234\text{ MPa}$  and  $T_{Ref} = T_0 = 233\text{ K}$ . No sign of brittle fracture was seen in the ballistic experiments for the NVE 36 target plates, therefore a ductile fracture criterion was still defined. Figure 6.30 presents the ballistic limit curves. An increase of 0.57% was observed for the ballistic limit velocity compared to RT. Table 6.19 presents the curve fitted Recht-Ipson parameters.

**Table 6.19:** Recht-Ipson parameters for experiments and base model.

	$a$	$p$	$v_{bl}$ [m/s]	Deviation in $v_{bl}$
Base model	1	2.26	368.7	-
-40 $^{\circ}\text{C}$	1	2.26	370.8	+0.57%

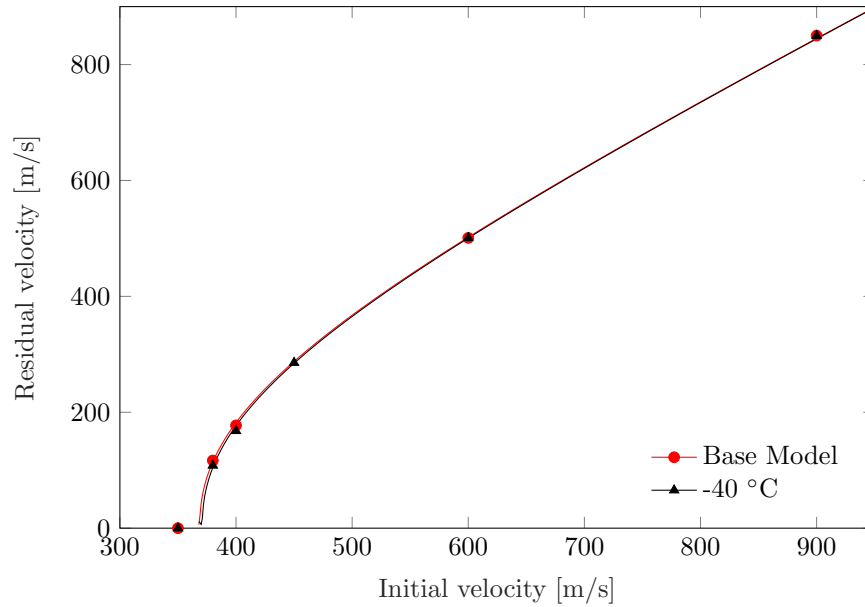


**Figure 6.30:** Ballistic limit curves for different temperatures.

A closer investigation was conducted to see if the decrease in the temperature affects the fracture modes and the brittle fracture relation. Both plots in Figure 6.31 indicates that the temperature do not influence the results that much. It should be noted that one value over five was observed, but the tendencies in the plot indicates ductile fracture. Only an increase in free nodes from 29061 to 31597 was observed. The close-ups of the impact holes are shown in Figure 6.32. They seem to be almost identically.

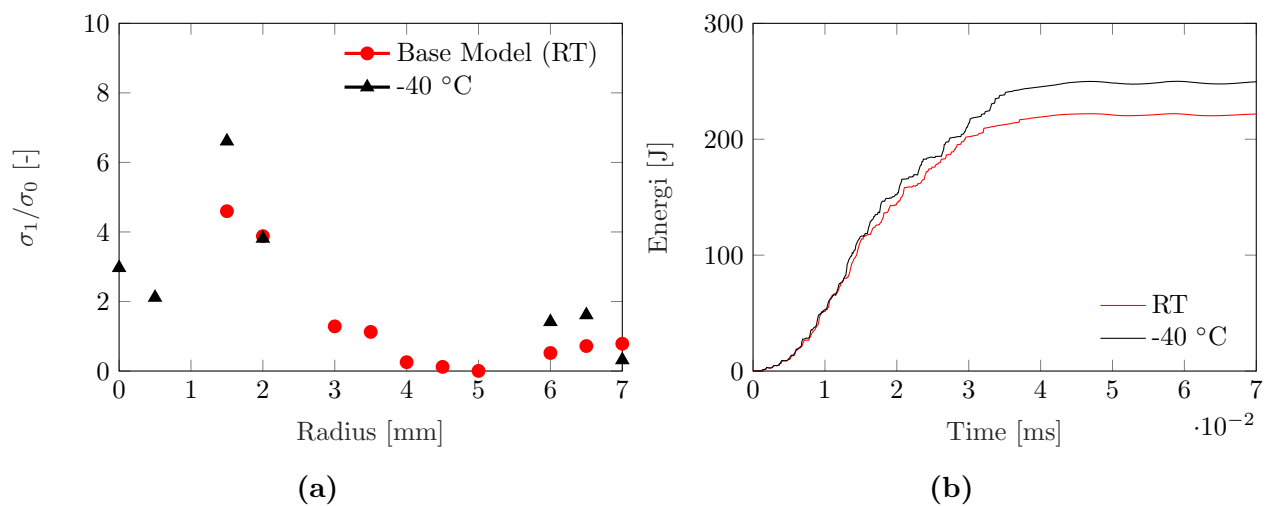


**Figure 6.31:** (a) Brittle fracture relation at 0.03 ms and (b) kinetic energy of free nodes.

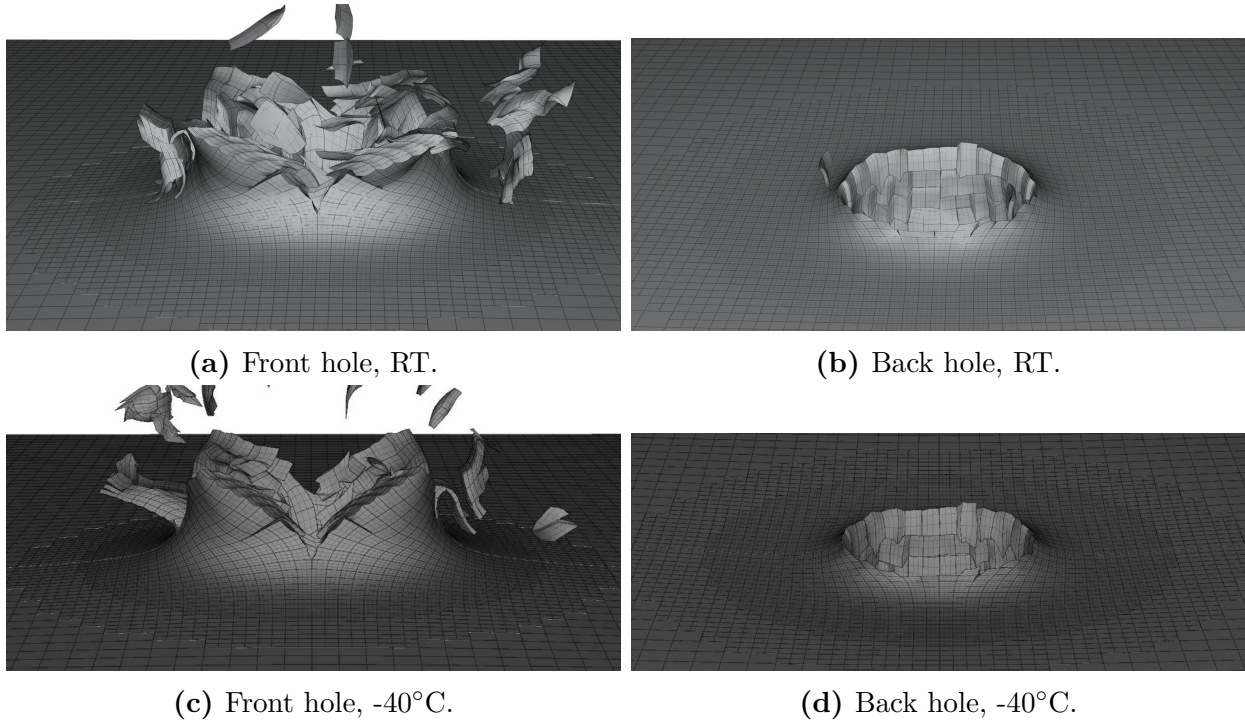


**Figure 6.32:** Close-ups of front and back holes at different temperatures for  $v_i = 900$  m/s.

## 6.3 Summary and Discussion

Table 6.20 presents a summary of ballistic limit velocities and failure modes for both Armox 500T and NVE 36. Following notations are used; Ductile Hole Growth (DHG), Fragmentation (F) and Radial Cracks (RC).

**Table 6.20:** Summary: Ballistic limit velocities and failure modes.

Material	Temperature	$v_{bl}$ [m/s]	Rel. diff.	Failure modes
Armox 500T	RT (20 °C)	528.3	-	DHG, RC, F <sup>1</sup>
Armox 500T	-40 °C	537.4	+1.73%	DHG, RC, F <sup>1</sup>
NVE 36	RT (20 °C)	368.7	-	DHG, RC, F <sup>1</sup>
NVE 36	-40 °C	370.8	+0.57%	DHG, RC, F <sup>1</sup>

<sup>1</sup> for high impact velocities.

- The numerical simulations seemed to capture the trends seen in the ballistic impact experiments. The decrease in the temperature gave an increase of 1.73% and 0.57% for the ballistic limit velocity for Armox 500T and NVE 36 respectively. From the experiments an increase of about 4% was observed.
- Ductile hole growth was the main failure mode for both materials at the various temperatures. Node splitting was able to capture the fragmentation observed in the experiments.
- The numerical simulations of the Armox 500T gave only a 0.69% non-conservative difference for the ballistic limit velocity compared to the experimental results. A conservative result was obtained for the NVE 36 steel. A deviation in ballistic limit velocity of 8.26% was observed.
- The DBTT seemed to be below -40 °C for both materials, due to approximately no change in failure modes for the different temperatures. Minor differences were seen in the brittle fracture relation for various temperatures. Also here the results indicated clearly that the failure modes were more sensitive to initial velocities than to temperatures within the studied range.
- The sensitivity studies conducted on mesh and boundary conditions showed that they only had minor influence on the residual velocity, especially for high velocities near 900 m/s.

- The residual velocity of the high strength steel Armox 500T was shown to be more sensitive for an impact angle than the low strength steel NVE 36.

# Concluding Remarks

A summary of important observations, results and conclusions from this thesis are given below. The objective of this study was to investigate how the ballistic properties of the armour steel Armox 500T and the structural steel NVE 36 were affected by a change in the temperature. Material tests were performed to describe the material behaviour at RT. Then ballistic impact experiments were conducted at RT and -40 °C. The plates were subjected to impacts by 7.62 mm APM2 bullets. Further, the MJC constitutive relation and the CL fracture criterion were calibrated for use in the numerical study. In the numerical study, the main goal was to reproduce the same trends that were seen in the ballistic impact experiments.

## Material Properties

The quasi-static tensile tests were performed using dog bone specimens of the Armox 500T steel and using smooth specimens of the NVE 36 steel. For both materials the tensile specimens were extracted from two different directions, 0° and 90°, with respect to the rolling direction of the plates. The results showed that the Armox 500T steel has about four times the yield stress of the NVE 36 steel. However, the opposite was true for the ductility. Some differences were seen in failure strain for the different directions, but otherwise the plastic flow was isotropic for both materials.

## Experimental Results

The ballistic experiments were conducted at RT and -40 °C. Only a deviation of +4.65% and +4.35% for the ballistic velocity were observed for the Armox 500T steel and for the NVE 36 steel respectively at -40 °C compared to RT. Minor effects were also seen for the failure modes for the two test temperatures. The failure modes seemed to be more sensitive for

initial velocities than for temperatures in this range. No sign of the ductile to brittle transition temperature was observed so the materials can be assumed ductile for most practical purposes in the tested temperature range.

### **Numerical Results**

For Armox 500T a deviation of +0.69% was observed for the ballistic limit velocity obtained by the numerical simulations compared to the value obtained by the ballistic impact experiments. For the NVE 36 steel a conservative result of -8.26% was obtained. The main fracture mode for both materials was ductile hole growth as in the experiments. The numerical simulations were able to capture the fragmentation. For numerical simulations at -40 °C the same tendencies were seen as in the experiments. The temperature has minor influence on the ballistic limit velocity. The amount of free nodes increase more with a higher initial velocity than for a decrease in the temperature. Additionally, the armour steel Armox 500T produce more free nodes than the low strength steel NVE 36.

The main conclusion for this thesis is that a change from RT to -40 °C has as a minor positive effect on the ballistic properties for the armour steel Armox 500T and for the structural steel NVE 36. This has been shown both experimentally and numerically.



### Further Work

- **Charpy V-notch tests.** Conduct several Charpy V-notch tests to determine the ductile to brittle transition temperature for both materials, experimentally and numerically.
- **More comprehensive material tests.** The strain rate hardening and temperature softening constants were found in the literature, since only quasi-static tests were conducted. These constants can be obtained from tensile tests with different strain rates and temperatures.
- **Investigate other materials.** Carry out the same tests on a material with a higher ductile to brittle transition temperature than Armox 500T and NVE 36.
- **Additional experiments.** Performed ballistic impact test with large projectiles, blunt and ogival nose shape.
- **More comprehensive numerical study.** A larger sensitivity study can be conducted. Oblique impact, friction coefficients, element erosion and brittle fracture criterion are of interest.



# Bibliography

- [1] Anderson TL. Fracture Mechanics: Fundamentals and Applications. Taylor & Francis Group, third edition, 2005.
- [2] Backman ME, Goldsmith W. The mechanics of penetration of projectiles into targets. International Journal of Engineering Science, 1978.
- [3] Baker WE, Westine PS, Dodge FT. Similarity methods in engineering dynamics: theory and practice of scale modeling. Spartan Books;[distributed by] Hayden Book Co., 1973.
- [4] Bridgman, PW. Trans Am. Soc. Met, vol. 32:553, 1944.
- [5] Børvik T, Hopperstad OS, Langseth M. TKT4128 Impact Mechanics - Lecture notes: An Introduction to Penetration and Perforation Mechanics. SIMLab, NTNU, 2015.
- [6] Børvik T, Hopperstad OS. Materials Mechanics - Part 1. SIMLab, NTNU, First version, 2015.
- [7] Børvik T, Hopperstad OS. Materials Mechanics - Part 2. SIMLab, NTNU, First version, 2016.
- [8] Børvik T, Hopperstad OS, Langseth M, Malo KA. Effect of target thickness in blunt projectile penetration of Weldox 460 E steel plates. International Journal of Impact Engineering, vol. 28, no. 4, pp. 413–464, 2003.
- [9] Børvik T, Dey S, Clausen AH. Perforation resistance of five different high-strength steel plates subjected to small-arms projectiles. International Journal of Impact Engineering, 36:948-964, 2009.
- [10] Børvik T, Hopperstad OS, Berstad T, Langseth M. Numerical simulations of plugging failure in ballistic penetration. International Journal of Solids and Structures, 38(34-35):6241-6264, 2001.

- [11] Børvik T, Olovsson L, Dey S, Langseth M. Normal and oblique impact of small arms bullets on AA6082-T4 aluminium protective plates. *International Journal of Impact Engineering*, 38:577-589, 2011.
- [12] Børvik T. Private communication, 2017.
- [13] Camacho GT and Ortiz M. Adaptive Lagrangian modelling of ballistic penetration of metallic targets. *Computer methods in applied mechanics and engineering*, vol. 142, no. 3, pp. 269–301, 1997.
- [14] Cockroft MG, Latham DJ. Ductility and the work ability of metals. *Journal of the Institute of Metals*, 96:33-39, 1968.
- [15] Dey S, Børvik T, Hopperstad OS, Langseth M. On the influence of fracture criterion in projectile impact of steel plates. *Computational Materials Science*, 38:176–91, 2006.
- [16] Dey S. High-strength steel plates subjected to projectile impact: An experimental and numerical study. PhD thesis, SIMLab, Norwegian University of Science and Technology, 2004.
- [17] Dey S, Børvik T, Hopperstad OS, Leinum JR, Langseth M. The effect of target strength on the perforation of steel plates using three different projectile nose shapes. *International Journal of Impact Engineering*, 30:1005-1038, 2004.
- [18] Dey S, Børvik T, Teng X, Wierzbicki T, Hopperstad OS. On the ballistic resistance of double-layered steel plates: An experimental and numerical investigation. *International Journal of Solids and Structures*, 44:6701–6723, 2007.
- [19] Dieter GE. *Mechanical Metallurgy: SI Metric Edition*. McGraw-Hill Book Company, third edition, 1988.
- [20] Erice B, Galvez F, Cendon DA, Sanchez-Galvez V and Børvik T. An experimental and numerical study of ballistic impacts on a turbine casing material at varying temperatures. *Journal of Applied Mechanics*, vol. 78, no. 5, p. 051019, 2011.
- [21] Fagerholt E. Field measurements in mechanical testing using close-range photogrammetry and digital image analysis. PhD thesis, Norwegian University of Science and Technology, 2012.
- [22] Goldsmith W. Non-ideal projectile impact on targets. *International Journal of Impact Engineering*, 22:95-395, 1999.

- 
- [23] Holmen JK. Private communication, 2017.
- [24] Holmen JK, Johnsen J, Jupp S, Hopperstad OS, Børvik T. Effects of heat treatment on the ballistic properties of AA6070 aluminium alloy. *International Journal of Impact Engineering*, 57:119-133, 2013.
- [25] Holmen JK, Johnsen J. Effects of Heat Treatment on the Ballistic Properties of AA6070 Aluminium Plates. Master's Thesis, 2012.
- [26] Holmen JK, Solberg JK, Hopperstad OS, Børvik T. Ballistic impact of layered and case-hardened steel plates. *International Journal of Impact Engineering*, 2017.
- [27] Holmen, JK. Dynamic Fracture Modeling. SIMLab, Norwegian University of Science and Technology, 2015.
- [28] IMPETUS Afea AS. IMPETUS Afea Solver [internet]. Available from: <http://www.impetus-afea.com>.
- [29] Johnson GR, Cook WH. A constitutive model and data for metals subjected to large strains, high strain rates and high temperatures. *Proceedings of the 7th International Symposium on Ballistics*, 1983.
- [30] Le Roy G, Embury JD, Edwards G, Ashby MF. A model of ductile fracture based on the nucleation and growth of voids. *Acta Metallurgica*, 29(8):1509-1522, 1981.
- [31] Mathisen KM. Private communication, 2016.
- [32] Olovsson L. Private communication, 2017.
- [33] Orthe E, Thorsen H. Ballistic Perforation of Surface Hardened Mild Steel Plates. Master's Thesis, Norwegian University of Science and Technology, 2014.
- [34] Recht RF, Ipson TW. Ballistic perforation dynamics. *Journal of Applied Mechanics*, vol. 30, no. 3, pp. 384-390, 1963.
- [35] SSAB. <https://www.ssab.com/products/brands/armox/armox-500t>. Obtained in February 2017.
- [36] Thomesen, S. Impact Behaviour of Steel at Low Temperatures. Master's Thesis, 2016.
- [37] Zukas JA. *High Velocity Impact Dynamics*. John Wiley and Sons, Inc., first edition, 1990.

- [38] Zukas JA, Scheffler DR. Practical aspects of numerical simulations of dynamic events: effects of meshing. *International Journal of Impact Engineering*, 24:925-945, 2000.
- [39] Zukas JA. *Impact dynamics*. John Wiley and Son, New York, 1982

# Armox 500T Steel

## A.1 Bullet Holes, RT

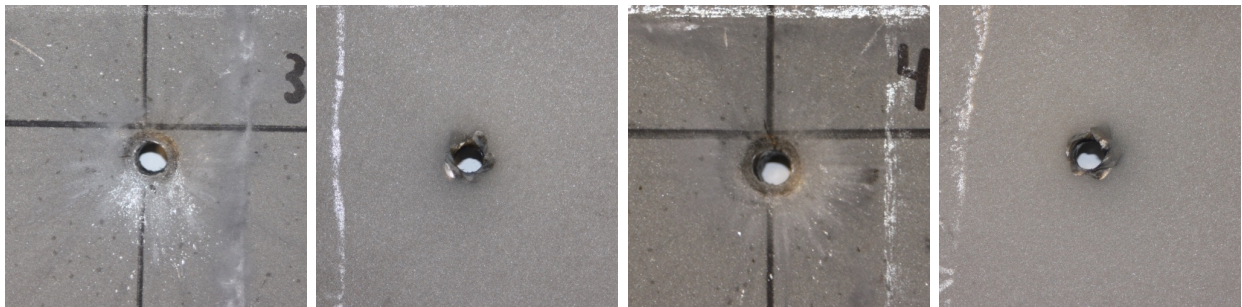


(a) Hole 1 - Front

(b) Hole 1 - Back

(c) Hole 2 - Front

(d) Hole 2 - Back



(e) Hole 3 - Front

(f) Hole 3 - Back

(g) Hole 4 - Front

(h) Hole 4 - Back



(i) Hole 5 - Front

(j) Hole 5 - Back

(k) Hole 6 - Front

(l) Hole 6 - Back



(m) Hole 7 - Front

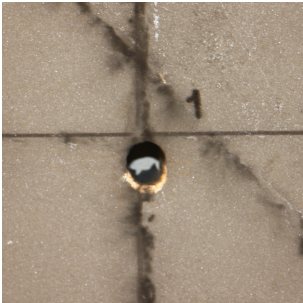
(n) Hole 7 - Back

(o) Hole 8 - Front

(p) Hole 8 - Back



## A.2 Bullet Holes, -40 °C



(a) Hole 1 - Front



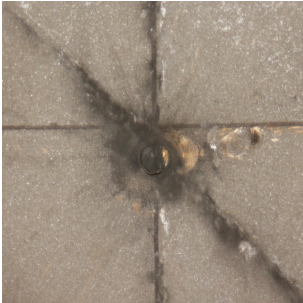
(b) Hole 1 - Back



(c) Hole 2 - Front



(d) Hole 2 - Back



(e) Hole 3 - Front



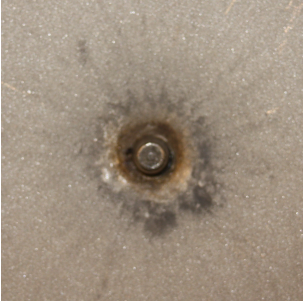
(f) Hole 3 - Back



(g) Hole 4 - Front



(h) Hole 4 - Back

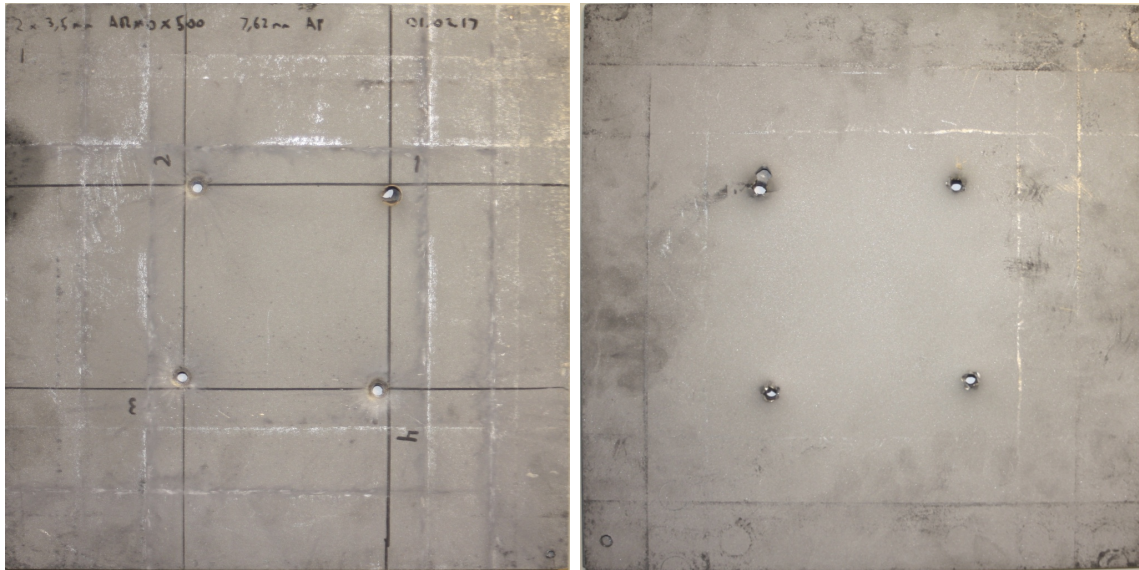


(i) Hole 5 - Front



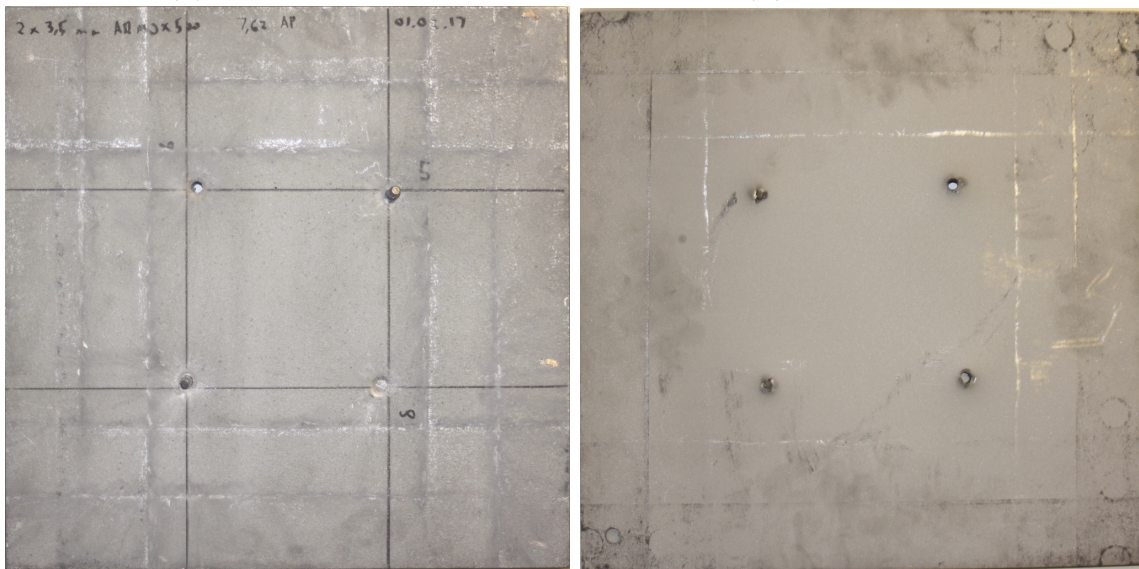
(j) Hole 5 - Back

### A.3 Front and Backside, RT



(a) Plate 1 - Front

(b) Plate 1 - Back



(c) Plate 2 - Front

(d) Plate 2 - Back

**Figure A.3:** Armox 500T - Plate thickness 2 x 3.5 mm



## A.4 Front and Backside, -40 °C



(a) Plate 1 - Front

(b) Plate 1 - Back

**Figure A.4:** Armox 500T - Plate thickness 2 x 3.5 mm



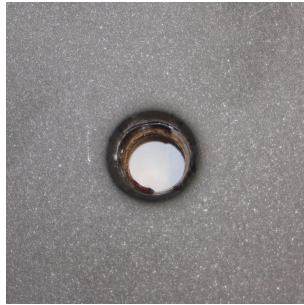
# NVE 36 Steel



## B.1 Bullet Holes, RT



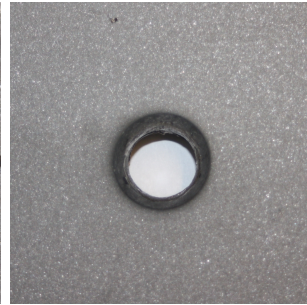
(a) Hole 1 - Front



(b) Hole 1 - Back



(c) Hole 2 - Front



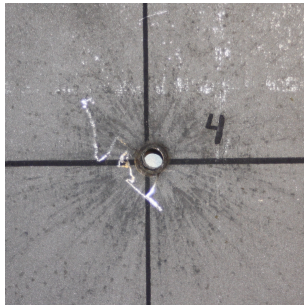
(d) Hole 2 - Back



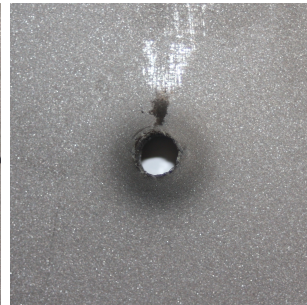
(e) Hole 3 - Front



(f) Hole 3 - Back



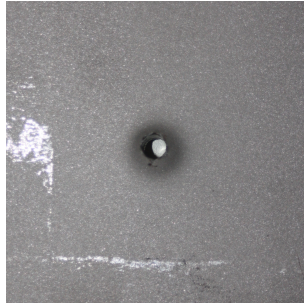
(g) Hole 4 - Front



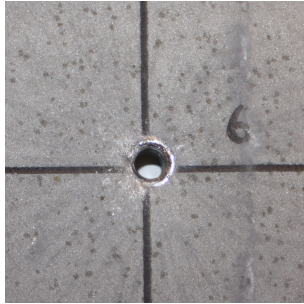
(h) Hole 4 - Back



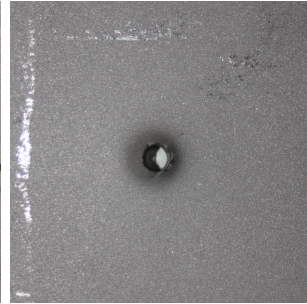
(i) Hole 5 - Front



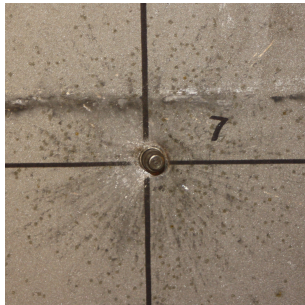
(j) Hole 5 - Back



(k) Hole 6 - Front



(l) Hole 6 - Back



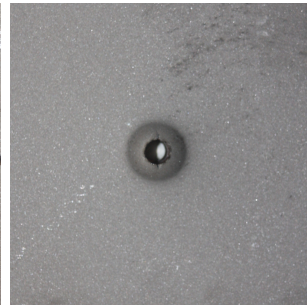
(m) Hole 7 - Front



(n) Hole 7 - Back



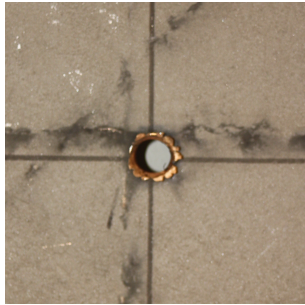
(o) Hole 8 - Front



(p) Hole 8 - Back



## B.2 Bullet Holes, -40 °C



(a) Hole 1 - Front



(b) Hole 1 - Back



(c) Hole 2 - Front



(d) Hole 2 - Back



(e) Hole 3 - Front



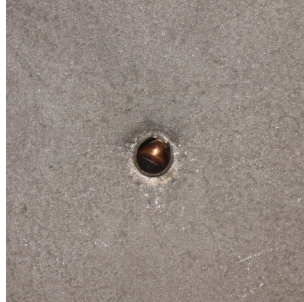
(f) Hole 3 - Back



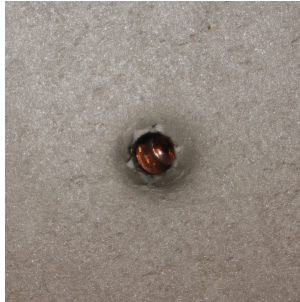
(g) Hole 4 - Front



(h) Hole 4 - Back

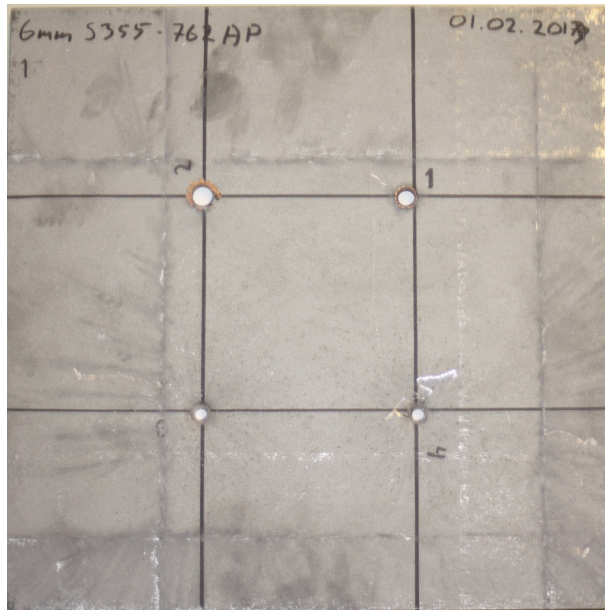


(i) Hole 5 - Front



(j) Hole 5 - Back

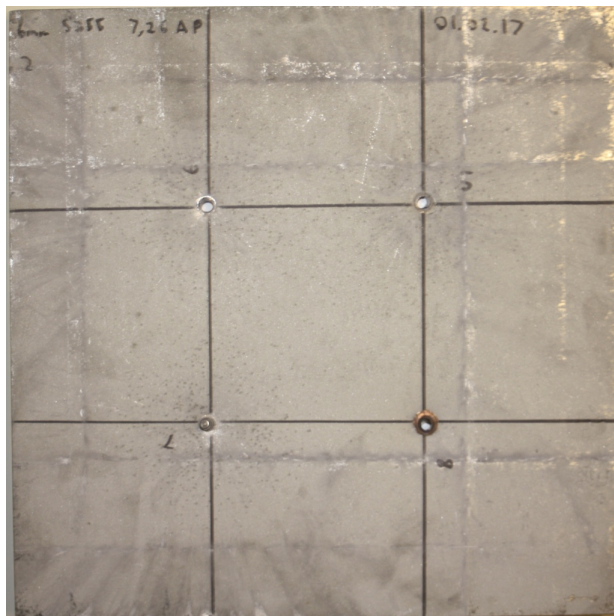
### B.3 Front and Backside, RT



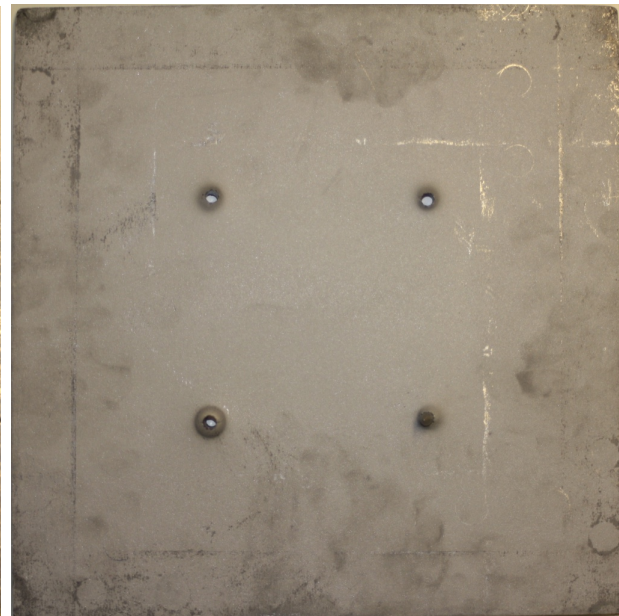
(a) Plate 1 - Front



(b) Plate 1 - Back



(c) Plate 2 - Front

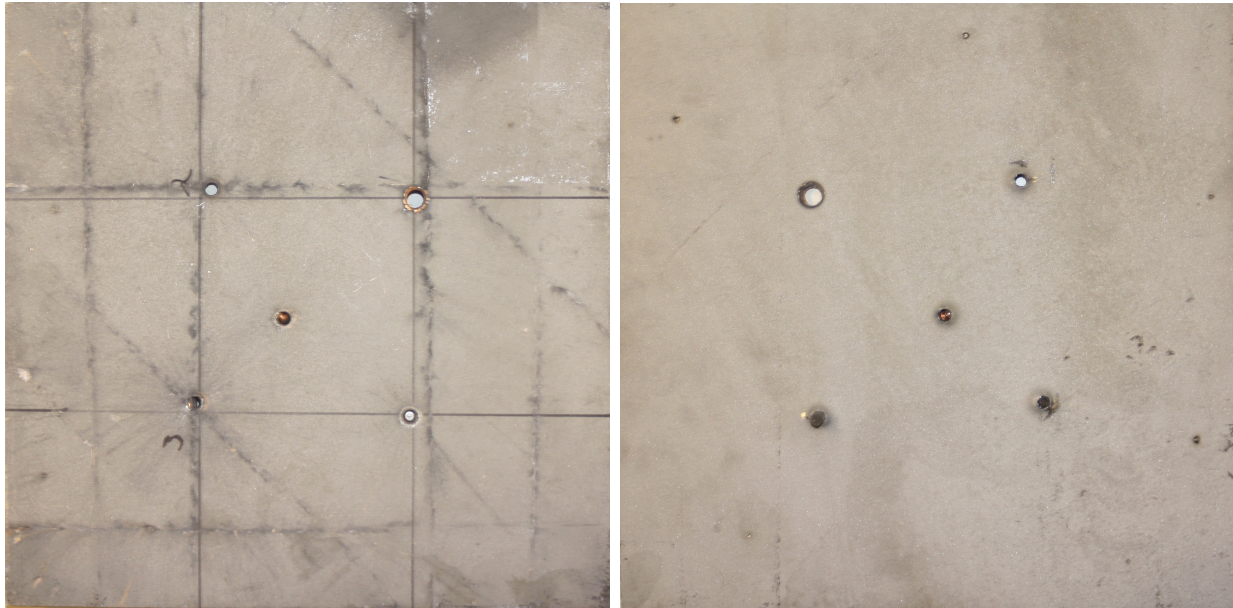


(d) Plate 2 - Back

**Figure B.3:** NVE 36 - Plate thickness 6 mm



## B.4 Front and Backside, -40 °C



(a) Plate 1 - Front

(b) Plate 1 - Back

**Figure B.4:** NVE 36 - Plate thickness 6 mm